Density Functional Theory for colloidal spheres in various external potentials

Inaugural-Dissertation

zur Erlangung des Doktorgrades
der Mathematisch-Naturwissenschaftlichen Fakultät
der Heinrich-Heine-Universität Düsseldorf

vorgelegt von

Tim Neuhaus

aus Hilden

Düsseldorf, März 2013

aus dem Institut für Theoretische Physik II: Weiche Materie
der Heinrich-Heine-Universität Düsseldorf

Gedruckt mit der Genehmigung der
Mathematisch-Naturwissenschaftlichen Fakultät der
Heinrich-Heine-Universität Düsseldorf

Referent: Prof. Dr. Hartmut Löwen
Korreferent: Prof. Dr. Stefan U. Egelhaaf

Tag der mündlichen Prüfung: 25. April 2013

List of published work

This thesis is based on the publications listed below. Most of the text has been rewritten but some parts are similar to the original publications.

[1] **Fluid phase separation inside a static periodic field: An effectively two-dimensional phenomenon**
R. L. C. Vink, T. Neuhaus, and H. Löwen, J. Chem. Phys. **134**, 204907 (2011).
Statement of the author: This paper was written in collaboration with Richard Vink who performed all simulations and analyzed the results obtained from these. Hartmut Löwen contributed by connecting these results with the theoretical predictions which were given by my calculations and analysis.

[2] **Soft repulsive mixtures under gravity: Brazil-nut effect, depletion bubbles, boundary layering, nonequilibrium shaking**
T. Kruppa, T. Neuhaus, R. Messina, and H. Löwen, J. Chem. Phys. **136**, 134106 (2012).
Statement of the author: In this paper, all simulations, the analysis of their results, as well as the work on the depletion bubble picture and the examination of the boundary layer were accomplished by Tobias Kruppa. All work concerning classical and dynamical density functional theory was performed by me. René Messina and Hartmut Löwen merged the examinations.

[3] **Rhombic preordering on a square substrate**
T. Neuhaus, M. Marechal, M Schmiedeberg, and H. Löwen, Phys. Rev. Lett. **110**, 118301 (2013).
Statement of the author: This paper is based on my results from density functional theory. Matthieu Marechal simulated the same system yielding a corroboration of the theoretical predictions. Finally, Michael Schmiedeberg and Hartmut Löwen contributed by linking both findings and organizing the outline and Michael Schmiedeberg created the schematic illustration of the system (figure 5.1).

[4] **Compatibility waves drive crystal growth on patterned substrates**
T. Neuhaus, M Schmiedeberg, and H. Löwen, submitted to New J. Phys. (2013)
Statement of the author: In this paper, all calculations and analysis were performed by me. Michael Schmiedeberg and Hartmut Löwen helped by supervising and guiding the work as well as writing parts and improving the rest. Figure 6.1(a) was drawn by Michael Schmiedeberg.

Contents

CHAPTER 1

Introduction

In 1991, Pierre-Gilles de Gennes received the Nobel Prize in physics for his work in applying the concepts of simple thermodynamics to more complex soft matter systems [5]. But what is soft matter? In contrast to hard materials such as aluminum or gold, soft matter systems are easier to deform — in other words, they have shear moduli which are several orders of magnitude lower than those of hard materials. The particles, which make up the soft matter system, are dispersed in a medium consisting of much smaller ’particles’ (i.e. molecules) such that the dispersion medium can be treated as a continuum and quantum mechanics can be neglected. Consequently, a lower size limit of about 1nm exists. On the other hand, the thermal energy of every particle in a soft matter system needs to be larger than or of the same order as its potential energy. In other words, the particles undergo thermal (Brownian) motion instead of just sedimenting in the dispersion. This gives a rough estimate of the upper size limit of colloidal particles of 10μm.

Soft matter systems can be classified into different types such as colloids and polymers. Colloids are mesoscopic particles of any shape, but most commonly spheres, disks, or rods. The phase in which the colloids and the dispersion medium exist are independent of one another and almost all combinations of phases can occur. Well known examples are paints (solid paint particles embedded in a liquid solution), milk (liquid fat droplets as well as protein micelles dissolved in liquid water), ice cream (liquid particles dispersed in frozen water), or even foam, where gaseous bubbles are dispersed in a liquid (e.g., beer head).

Polymers are long chains of subunits, called monomers, which are linked by covalent chemical bonds where the bond energy is much larger than the thermal energy. Typically, polymers consist of hundreds to millions of monomers. These can form simple linear chains or branches of chains (e.g., in dendrimers or star-polymers). In most cases, the polymers are coiled so that they can be modeled as spheres with a radius of gyration[1]. Polymers are used in everyday applications, such as plastics or rubber, but are also used as a model for DNA.

One of the main advantages of colloidal systems is that experiments can typically be

---

[1] The square of the radius of gyration for a linear polymer chain with N monomers at position $\mathbf{r}_i$ is given by $R_\mathrm{g}^2 = \frac{1}{N}\sum\limits_{i=1}^{N}(\mathbf{r}_i - R_\mathrm{G})^2$, including the position of the center of masses R_G. [6]

performed at ambient temperature with particles which can be examined for example by either microscopy or scattering experiments. One can also study the fundamental properties of many-body systems, an undertaking which is practically impossible in molecular or atomic systems. Therefore, they can serve as excellent model systems.

How can soft matter systems be modeled? The simplest model system imaginable consists of hard spherical particles – colloids – dispersed in a liquid. These hard spheres cannot overlap and do not interact when the particle-particle distance is larger than their diameter. Nevertheless, a liquid-solid phase transition which is purely entropically driven has been observed for hard sphere colloidal systems. This was experimentally proven in the famous work of P. N. Pusey and W. van Megen in 1986 [7]. They examined dispersed PMMA (Poly(methyl methacrylate)[2]) spheres, which where sterically stabilized by polymer chains in order to suppress the electrostatic van-der-Waals attraction such that the interaction potential approximates the hard sphere potential. The Bragg reflections of these spherical particles at different packing fractions were studied, leading to a fluid, a crystalline, and a glass phase.

Based on this bulk phase diagram, multiple examinations of hard sphere systems followed. In addition to the bulk behavior, where for example interfaces between different phases were studied, the influence of confining geometries (e.g., planar or structured walls) or of other external potentials (e.g., induced by magnetic or optical fields, or by gravity) was explored[3]. Furthermore, non-equilibrium situations including homogeneous as well as heterogeneous nucleation were analyzed.

In this thesis, hard spherical colloids provide the basis for all studies. The addition of polymers into a dispersion of hard spherical colloids modifies the interaction potential of the spheres which then can be described using the Asakura-Oosawa (AO) model [9–11]. Here, the polymers are treated as spheres when the interaction between a colloid and a polymer is considered. Interactions between different polymers are modeled to be ideal, or in other words, two polymers do not interact but simply penetrate one another. Colloid-colloid as well as colloid-polymer interactions are modeled as hard-body interactions. In this case, an effective interaction potential can be calculated for the pairwise interaction of two colloids, which is affected by the surrounding polymers. Consequently, there is no separate term left which describes the interaction with polymers [12]. Bulk coexistence of a colloid-rich and a colloid-poor phase can be observed [13]. In chapter 3, such a binary mixture is studied under the influence of an external light field which is periodic in space. The external potential induces a phase which varies strongly in the local density of the colloids (and the polymers respectively) [14], and, is hence called the *zebra* phase. The phase diagram as well as the critical behavior is computed and analyzed.

Well known from everyday life is the *brazil-nut effect*, which can occur in a shaken mixture of particles with different sizes and shapes, for example in a package of cereals which contains small grains and larger berries. When the package is shaken, small grains more

---

[2] Commonly known as Plexiglas®.

[3] For a review see, for example Ref. [8].

frequently slide under a large berry than vice versa. Thus, after some time, the berries are lifted and are finally located on top of the package. This effect can also be observed in a binary mixture of repulsive particles under gravity, as will be discussed in chapter 4. Here, the different regimes of occurrence of the brazil-nut regime are depicted in the static and dynamic case (the box is inverted periodically in time).

Compared with a dispersion of hard spheres in three dimensions, the behavior of hard disks on a surface was studied much less even though it seems to be simpler at first glance. Based on the bulk phase diagram [15], the effect of a patterned substrate on the equilibrium phases can be studied and the results are presented in chapter 5. In bulk, hard disks either form a homogeneous fluid or a crystal with hexagonal structure. Inducing a substrate potential results in a competition of this structure with the square symmetry of the substrate pattern which leads to *rhombic* preordering. The resulting phase diagram is explored and the transitions between the different orders are studied. Furthermore, growth dynamics of a dispersion of hard disks located on patterned substrates can be examined (see chapter 6). In this case, the substrate locally modifies the velocity of growth yielding a new mechanism of growth which is based on subsequent island formation and driven by a *compatibility wave*.

All these diverse systems have been explored using a common method: In 1964, P. Hohenberg and W. Kohn investigated the density functional theory (DFT) [16] in which an energy functional of the local density can be constructed that becomes minimal for the equilibrium configuration of the system. The importance of this development was honored with the Nobel Prize in chemistry for Walter Kohn [17] in 1998. This first idea for DFT was constructed for an interacting electron gas in an external potential and later, it was applied to classical systems (for a review see for example [18]). The prime challenge for soft matter systems is to find a functional which describes the particle interactions and recovers the phase behavior. In the following chapter, some approaches for this functional are presented, including some concepts from thermodynamics and statistical mechanics which are necessary for the derivations.

CHAPTER 2

Theoretical basics

To explain density functional theory, some concepts have to be pointed out first, in order to have a solid basis for the theory. This goes back to the work of Maxwell, Boltzmann, and Gibbs [19–21] in the 1870's, who dealt with equilibrium statistical mechanics to describe many particle systems by writing down effective Hamiltonians. In classical mechanics, the particle motion can be described by the exact Hamiltonian but for many body systems, which are considered in this work, this approach fails due to complexity. In this section, the main concepts of thermodynamics and statistical mechanics which are required for this work, will be pointed out. Afterwards, based on this, the focus will be laid on classical and dynamical density functional theory. The outline of the descriptions in common textbooks [22,23], recent review articles [15,24,25], and some lecture notes [26,27] will be followed.

2.1 Thermodynamics and Statistical Physics

A system of N particles has $6N$ coordinates in phase space, namely the positions $\mathbf{r}^N = (\mathbf{r}_1, \ldots, \mathbf{r}_N)$ and momenta $\mathbf{p}^N = (\mathbf{p}_1, \ldots, \mathbf{p}_N)$, with $\mathbf{r}_i$ and $\mathbf{p}_i$ describing the position and the momentum of particle i. The Hamiltonian H of this system then can be composed as a sum of the kinetic energy T, interparticle potential energy U, and the external potential U_{ext},

$$H(\mathbf{r}^N, \mathbf{p}^N) = T(\mathbf{p}^N) + U(\mathbf{r}^N) + U_{\text{ext}}(\mathbf{r}^N), \tag{2.1}$$

where the kinetic energy of particles with mass m_i is given by

$$T(\mathbf{p}^N) = \sum_{i=1}^{N} \frac{\mathbf{p}_i^2}{2m_i}. \tag{2.2}$$

Assuming that the particles only have pairwise interactions with an effective interaction potential $\phi(\mathbf{r})$, the potential energy U has the form

$$U(\mathbf{r}^N) = \sum_{i<j} \phi(\mathbf{r}_i - \mathbf{r}_j), \tag{2.3}$$

with particle i at position $\mathbf{r}_i$ and particle j at position $\mathbf{r}_j$. Solving the Hamiltonian for this system becomes inefficient at large particle numbers and impossible for classical many-body systems with $N \approx 10^{23}$ particles. Here, it is necessary to introduce averaged or *macroscopic* variables in order to describe the behavior of the system. Depending on the actual system it is important to choose different macroscopic variables. In thermodynamics the common state variables are the entropy S, the temperature T of the system, the pressure p, the volume V that is accessible to the particles, the number of particles N, and the chemical potential μ. In the *canonical ensemble* where energy can be exchanged with a heat bath, the set of fixed quantities which characterize the system is (T, V, N) and the potential which results is the Helmholtz free energy F with

$$F(T, V, N) = -ST - pV + \mu N. \tag{2.4}$$

In order to compare the results with the microscopic description, the canonical partition function for a three-dimensional system becomes

$$Z(T, V, N) = \frac{1}{h^{3N} N!} \int \mathrm{d}\mathbf{p}^N \int \mathrm{d}\mathbf{r}^N e^{-\beta H}, \tag{2.5}$$

where H is the Hamiltonian from equation (2.1) and $\beta = (k_B T)^{-1}$ is the inverse temperature with the Boltzmann constant k_B, and the Planck constant h. The canonical free energy can be expressed in terms of Z as

$$F(T, V, N) = -k_B T \ln Z(T, V, N). \tag{2.6}$$

If the system allows particle exchange in addition to heat exchange, the fixed set of quantities will be (T, V, μ). In this *grand canonical ensemble*, the energy is called the grand canonical free energy Ω and reads

$$\Omega(T, V, \mu) = F - \mu N = -k_B T \ln \Xi(T, V, \mu), \tag{2.7}$$

with the grand canonical partition function

$$\Xi(T, V, \mu) = \sum_{N=0}^{\infty} e^{\beta \mu N} Z(T, V, N) = \sum_{N=0}^{\infty} \frac{z^N}{h^{3N} N!} \int \mathrm{d}\mathbf{p}^N \int \mathrm{d}\mathbf{r}^N e^{-\beta H}. \tag{2.8}$$

Here, z is the *fugacity* with $z = e^{\beta \mu}$.

2.2 Density Functional Theory

Density functional theory (DFT) was first invented by Hohenberg and Kohn [16] for an inhomogeneous electron gas in 1964. They found a functional for the energy of the system that only depends on the electron density, but which is similar for all external potentials. In honor of this great idea, Walter Kohn received the Nobel Prize in chemistry in 1998 [17]. This approach was generalized to finite temperatures by Mermin [28] in 1965, and adapted to classical systems by Ebner et al. [29]. In his work, Mermin proved that there is a unique functional $\Omega[\rho(\mathbf{r})]$ which depends on the average one-body density,

$$\rho(\mathbf{r}) = \langle\hat{\rho}(\mathbf{r})\rangle = \left\langle \sum_{i=1}^{N} \delta(\mathbf{r}-\mathbf{r}_i) \right\rangle \equiv \rho^{(1)}(\mathbf{r}), \tag{2.9}$$

and becomes minimal for the equilibrium density. Here, $\langle\rangle$ denotes the grand canonical ensemble average defined for any $u(\mathbf{r})$ as

$$\langle u(\mathbf{r})\rangle = \sum_{N=0}^{\infty} \frac{1}{h^{3N}N!} \int \mathrm{d}\mathbf{p}^N \int \mathrm{d}\mathbf{r}^N u(\mathbf{r}) f_N, \tag{2.10}$$

with the grand canonical probability density

$$f_N = \frac{1}{\Xi} e^{-\beta(H-\mu N)}. \tag{2.11}$$

For an external potential $U_{\text{ext}}(\mathbf{r}^N) = \sum_{i=1}^{N} V_{\text{ext}}(\mathbf{r}_i)$, affecting each particle independent of all other particles, the average of the external potential including the mean density which is defined above, reads

$$\left\langle U_{\text{ext}}(\mathbf{r}^N)\right\rangle = \int \mathrm{d}\mathbf{r}\langle\hat{\rho}(\mathbf{r})\rangle V_{\text{ext}}(\mathbf{r}) = \int \mathrm{d}\mathbf{r}\rho^{(1)}(\mathbf{r})V_{\text{ext}}(\mathbf{r}). \tag{2.12}$$

Assuming that the external potential is infinite outside of the accessible volume V it can determine the volume so that the Helmholtz free energy F from equation (2.4) becomes

$$F = \mathcal{F}[\rho(\mathbf{r})] - \int \mathrm{d}\mathbf{r}\rho^{(1)}(\mathbf{r})V_{\text{ext}}(\mathbf{r}), \tag{2.13}$$

where $\mathcal{F}[\rho(\mathbf{r})]$ denotes the intrinsic Helmholtz free energy functional which is independent of any external potential $V_{\text{ext}}(\mathbf{r})$. Accordingly, the initial step of DFT is rewriting the grand canonical free energy of equation (2.7) as a functional of $\rho(\mathbf{r})$

$$\Omega[\rho(\mathbf{r})] = \mathcal{F}[\rho(\mathbf{r})] + \int \mathrm{d}\mathbf{r}\rho(\mathbf{r})(V_{\text{ext}}(\mathbf{r})-\mu). \tag{2.14}$$

The minimization of Ω yields the Euler-Lagrange equation

$$\frac{\delta\Omega[\rho(\mathbf{r})]}{\delta\rho(\mathbf{r})} = \frac{\delta\mathcal{F}[\rho(\mathbf{r})]}{\delta\rho(\mathbf{r})} + V_{\text{ext}}(\mathbf{r}) - \mu = 0, \tag{2.15}$$

where the task is now to find a functional $\mathcal{F}[\rho]$.

The simplest system to be assumed is the classical ideal gas, where particles are not interacting at all ($U(\mathbf{r}^N) \equiv 0$). This serves on the one hand as an exemplary calculation and on the other hand as a part of the full grand canonical free energy functional, as will be explained later. The grand canonical partition function of equation (2.8) in this case becomes

$$\Xi_{\text{id}} = \sum_{N=0}^{\infty} \frac{(zZ_1)^N}{\Lambda^3 N!} = \frac{1}{\Lambda^3} e^{zZ_1}, \tag{2.16}$$

with the thermal De-Broglie wavelength $\Lambda = \frac{h}{\sqrt{2\pi m k_B T}}$ and the one-particle partition function

$$Z_1 = \int \mathrm{d}\mathbf{r} e^{-\beta V_{\text{ext}}(\mathbf{r})}. \tag{2.17}$$

Resulting from this, the grand canonical free energy of equation (2.7) takes the form

$$\Omega_{\text{id}} = -z k_B T \int \mathrm{d}\mathbf{r} e^{-\beta V_{\text{ext}}(\mathbf{r})} + k_B T \ln \Lambda^3 \tag{2.18}$$

which leads to the equilibrium density distribution

$$\rho_{\text{id}}(\mathbf{r}) = \frac{1}{\Lambda^3} e^{-\beta(V_{\text{ext}}(\mathbf{r}) - \mu)}. \tag{2.19}$$

Hence, a functional for the ideal gas is given by

$$\mathcal{F}_{\text{id}} = k_B T \int \mathrm{d}\mathbf{r} \rho(\mathbf{r}) \left[\ln(\Lambda^3 \rho(\mathbf{r})) - 1\right]. \tag{2.20}$$

For any kind of interaction the Helmholtz free energy can be written as a sum of this exact ideal gas term and a term due to the inter-particle interactions, which is called the *excess free energy* $\mathcal{F}_{\text{exc}}$,

$$\mathcal{F}[\rho(\mathbf{r})] = \mathcal{F}_{\text{id}}[\rho(\mathbf{r})] + \mathcal{F}_{\text{exc}}[\rho(\mathbf{r})]. \tag{2.21}$$

With this excess free energy functional, the grand canonical free energy $\Omega[\rho(\mathbf{r})]$ of equation (2.14) converts to

$$\Omega[\rho(\mathbf{r})] = \mathcal{F}_{\text{exc}}[\rho(\mathbf{r})] + k_B T \int \mathrm{d}\mathbf{r} \rho(\mathbf{r}) \left[\ln(\Lambda^3 \rho(\mathbf{r})) - 1 + \beta V_{\text{ext}}(\mathbf{r}) - \beta\mu\right]. \tag{2.22}$$

As mentioned before, the Euler-Lagrange equation can be obtained by minimizing this grand canonical free energy, so that the result becomes

$$\frac{\delta\Omega[\rho(\mathbf{r})]}{\delta\rho(\mathbf{r})} = \frac{\delta\mathcal{F}_{\text{exc}}[\rho(\mathbf{r})]}{\delta\rho(\mathbf{r})} + k_B T \left[\ln(\Lambda^3 \rho(\mathbf{r})) + \beta V_{\text{ext}}(\mathbf{r}) - \beta\mu\right] = 0. \tag{2.23}$$

This equation leads to a hierarchy of functions, which are called the *direct correlation functions*, and describe correlations between particles. As an example the two-body correlation function $c^{(2)}(\mathbf{r}_1, \mathbf{r}_2)$ explains the effect of a fixed particle at position $\mathbf{r}_1$ on a second particle at position $\mathbf{r}_2$. This hierarchy takes the form

$$\begin{aligned} c^{(1)}(\mathbf{r}) &= -\frac{\delta(\beta\mathcal{F}_{\mathrm{exc}}[\rho(\mathbf{r})])}{\delta\rho(\mathbf{r})}, \\ c^{(2)}(\mathbf{r}_1,\mathbf{r}_2) &= \frac{\delta c^{(1)}(\mathbf{r}_1)}{\delta\rho(\mathbf{r}_2)} = -\frac{\delta^2(\beta\mathcal{F}_{\mathrm{exc}}[\rho])}{\delta\rho(\mathbf{r}_1)\delta\rho(\mathbf{r}_2)}, \\ c^{(n)}(\mathbf{r}_1,\ldots,\mathbf{r}_n) &= \frac{\delta c^{(n-1)}(\mathbf{r}_1,\ldots,\mathbf{r}_{n-1})}{\delta\rho(\mathbf{r}_n)} = \ldots = -\frac{\delta^n(\beta\mathcal{F}_{\mathrm{exc}}[\rho])}{\delta\rho(\mathbf{r}_1)\ldots\delta\rho(\mathbf{r}_n)}. \end{aligned} \tag{2.24}$$

Rewriting equation (2.23) leads to a formula for the equilibrium density distribution

$$\rho(\mathbf{r}) = \exp\left[-\frac{\delta(\beta\mathcal{F}_{\mathrm{exc}}[\rho(\mathbf{r})])}{\delta\rho(\mathbf{r})} - \beta V_{\mathrm{ext}}(\mathbf{r}) + \beta\mu\right], \tag{2.25}$$

or using the results from equation (2.24)

$$\rho(\mathbf{r}) = \exp\left[c^{(1)}(\mathbf{r}) - \beta V_{\mathrm{ext}}(\mathbf{r}) + \beta\mu\right], \tag{2.26}$$

which becomes the barometric law for non-interacting particles ($c^{(1)}(\mathbf{r}) \equiv 0$). In any case, this theory does not contain any approximations but it is exact for all systems. The only unknown term is the excess free energy functional which shall be further specified in the following section.

2.3 Approaches for the excess functional

The previously described theory requires an expression for an excess free energy functional. If there is such a functional the density distribution and the free energy can be calculated directly. Unfortunately, the only known exact excess free energy functional was discovered by Percus for hard rods in one dimension [30] in 1976. For all other systems, the excess free energy functional has to be approximated using theoretical principles. Over the years several approaches were published which tried to describe the behavior of inhomogeneous fluids near a wall or the freezing transition. Two of the main concepts are presented in this section which are both *mean-field* approximations. This means that they average over all possible configurations of the system and by this, e.g., ignore any fluctuations of interfaces and educe only mean-field critical exponents (see section 3.2.3).

2.3.1 Density expansion

By assuming two density distributions $\rho_0(\mathbf{r})$ and $\rho_1(\mathbf{r})$ and a linear interpolation between both distributions, the density profile only depends on a coupling parameter λ as

$$\rho_\lambda := \rho(\mathbf{r};\lambda) = \rho_0(\mathbf{r}) + \lambda(\rho_1(\mathbf{r}) - \rho_0(\mathbf{r})) = \rho_0(\mathbf{r}) + \lambda\Delta\rho(\mathbf{r}), \tag{2.27}$$

with $0 \leq \lambda \leq 1$. In other words, these density distributions can be expressed as $\rho_0(\mathbf{r}) = \rho(\mathbf{r}; 0)$ and $\rho_1(\mathbf{r}) = \rho(\mathbf{r}; 1)$. The excess free energy $\mathcal{F}_{\mathrm{exc}}$ then can be obtained from equation (2.24) by functional integration so that

$$\beta\mathcal{F}_{\mathrm{exc}}[\rho_\lambda] - \beta\mathcal{F}_{\mathrm{exc}}[\rho_0] = -\int_0^1 \mathrm{d}\lambda \int \mathrm{d}\mathbf{r}\Delta\rho(\mathbf{r})c^{(1)}([\rho_\lambda]; \mathbf{r}), \tag{2.28}$$

and a second integration leads to

$$c^{(1)}([\rho_\lambda]; \mathbf{r}_1) - c^{(1)}([\rho_0]; \mathbf{r}_1) = \int_0^\lambda \mathrm{d}\lambda' \int \mathrm{d}\mathbf{r}_2\Delta\rho(\mathbf{r}_2)c^{(2)}([\rho_{\lambda'}]; \mathbf{r}_1, \mathbf{r}_2). \tag{2.29}$$

Combining these two equations, an exact excess free energy functional takes the form

$$\begin{aligned}\beta\mathcal{F}_{\mathrm{exc}}[\rho_\lambda] =& \beta\mathcal{F}_{\mathrm{exc}}[\rho_0] - \int \mathrm{d}\mathbf{r}\Delta\rho(\mathbf{r})c^{(1)}([\rho_\lambda]; \mathbf{r}) \\ & - \int_0^1 \mathrm{d}\lambda \int \mathrm{d}\mathbf{r}_1\Delta\rho(\mathbf{r}_1) \int_0^\lambda \mathrm{d}\lambda' \int \mathrm{d}\mathbf{r}_2\Delta\rho(\mathbf{r}_2)c^{(2)}([\rho'_\lambda]; \mathbf{r}_1, \mathbf{r}_2).\end{aligned} \tag{2.30}$$

In the framework of density expansion, the initial density distribution $\rho_0(\mathbf{r})$ is assumed to be that of a bulk fluid ρ_b, so that $\rho(\mathbf{r}) = \rho_b + \Delta\rho(\mathbf{r})$, and the two-body direct correlation function is set to be that of a fluid $c^{(2)}([\rho_\lambda]; \mathbf{r}_1, \mathbf{r}_2) = c^{(2)}(\rho_b; r_{12})$, which only depends on the distances of two particles $r_{12} = |\mathbf{r}_2 - \mathbf{r}_1|$. Minimizing the resulting grand canonical free energy functional gains a term for the density distribution compared to the ideal gas

$$\rho(\mathbf{r}_1) = \rho_b \exp\left[-\beta V_{\mathrm{ext}}(\mathbf{r}_1) + \int \mathrm{d}\mathbf{r}_2 c^{(2)}(\rho_b; r_{12})(\rho(\mathbf{r}_2) - \rho_b)\right]. \tag{2.31}$$

In the case of low packing fractions and pairwise additive interaction potentials $\phi(r)$, the excess free energy functional can be obtained by a virial expansion, so that

$$\begin{aligned}\beta\mathcal{F}_{\mathrm{exc}}[\rho] =& -\frac{1}{2}\int \mathrm{d}\mathbf{r}_1\rho(\mathbf{r}_1)\int \mathrm{d}\mathbf{r}_2\rho(\mathbf{r}_2)f(r_{12}) \\ & - \frac{1}{6}\int \mathrm{d}\mathbf{r}_1\rho(\mathbf{r}_1)\int \mathrm{d}\mathbf{r}_2\rho(\mathbf{r}_2)\int \mathrm{d}\mathbf{r}_3\rho(\mathbf{r}_3)f(r_{12})f(r_{13})f(r_{23}) + \ldots,\end{aligned} \tag{2.32}$$

with the Mayer function $f(r) = e^{-\beta\phi(r)} - 1$. The combination of equation (2.32) and the two-body direct correlation function from equation (2.24) leads to

$$c^{(2)}(\rho_b; r_{12}) = f(r_{12}) + \rho_b f(r_{12}) \int \mathrm{d}\mathbf{r}_3 f(r_{13})f(r_{23}) + \ldots. \tag{2.33}$$

Accordingly, the functional has to fulfill that in the zero density limit $c^{(2)}(r)$ is equal to the Mayer function $f(r)$. Examples for this functional are the works of Ramakrishnan and Youssuff [31] and of Haymet and Oxtoby [32].

2.3.2 Fundamental Measure Theory for hard spheres

Fundamental Measure Theory (FMT) was developed by Rosenfeld 1989 [33] for an m-component mixture of additive hard spheres with diameter σ_i in a three-dimensional system. Here, the interaction potential is defined by

$$\phi_{ij}(r) = \begin{cases} \infty & , \text{ for} r < \sigma_{ij} \\ 0 & \text{, otherwise,} \end{cases} \tag{2.34}$$

where $\sigma_{ij} = \frac{1}{2}(\sigma_i + \sigma_j)$ for particles of species i (diameter σ_i) and j (diameter σ_j). Accordingly, particles cannot overlap but move freely in all other cases. The derivation of FMT is based on the exact solution of hard rods in one dimension [30] and the exact low density limit from equation (2.32). Starting with the latter, the Mayer function for hard spheres can be written as

$$f_{ij}(r) = \begin{cases} -1 & , \text{ for} r < \sigma_{ij} \\ 0 & \text{, otherwise,} \end{cases} \tag{2.35}$$

or by using the Heaviside step function $\theta(r)$ as

$$f_{ij}(r) = -\theta(\sigma_{ij} - r). \tag{2.36}$$

The approach is now to use the *cross-correlation* $\otimes$, which in contrast to the definition of the convolution (see equation (2.41)) is given by

$$(f \otimes g)(\mathbf{r} = \mathbf{r}_i - \mathbf{r}_j) = \int \mathrm{d}\mathbf{r}' f(\mathbf{r}' - \mathbf{r}_i) g(\mathbf{r}' - \mathbf{r}_j), \tag{2.37}$$

to decompose the Mayer function into correlations of weight functions which result from geometrical features as

$$\begin{aligned} -f_{ij}(r) =& \omega_3^i \otimes \omega_0^j + \omega_0^i \otimes \omega_3^j + \omega_2^i \otimes \omega_1^j + \omega_1^i \otimes \omega_2^j \\ &- \boldsymbol{\omega}_2^i \otimes \boldsymbol{\omega}_1^j - \boldsymbol{\omega}_1^i \otimes \boldsymbol{\omega}_2^j. \end{aligned} \tag{2.38}$$

The weight functions ω_ν^i are given by

$$\begin{aligned} \omega_3^i(r) &= \theta(R_i - r), \\ \omega_2^i(r) &= \delta(R_i - r), \end{aligned}$$

$$\begin{aligned}
\omega_1^i(r) &= \frac{1}{4\pi R_i}\omega_2^i(r) = \frac{1}{4\pi R_i}\delta(R_i - r),\\
\omega_0^i(r) &= \frac{1}{4\pi R_i^2}\omega_2^i(r) = \frac{1}{4\pi R_i^2}\delta(R_i - r),\\
\boldsymbol{\omega}_2^i(r) &= \frac{\mathbf{r}}{r}\delta(R_i - r),\\
\boldsymbol{\omega}_1^i(r) &= \frac{1}{4\pi R_i}\boldsymbol{\omega}_2^i(r) = \frac{1}{4\pi R_i}\frac{\mathbf{r}}{r}\delta(R_i - r),
\end{aligned} \tag{2.39}$$

with R_i denoting the radius of particles of species i ($R_i = \sigma_i/2$). $\delta(x)$ is the well known Dirac delta function, and $\theta(x)$ indicates the Heaviside step function defined as [34]

$$\theta(x) = \begin{cases} 1, & \text{, for} x > 0,\\ 0, & \text{, for} x \leq 0. \end{cases} \tag{2.40}$$

$\omega_\nu^i(r)$ indicates the four scalar weight functions $\omega_{(0,1,2,3)}^i(r)$ as well as the two vector weight functions $\boldsymbol{\omega}_{(1,2)}^i(r)$. Knowing these weight functions, six weighted densities $n_\nu(\mathbf{r})$ are defined using a convolution $*$ which is

$$(f * g)(\mathbf{r}) = \int \mathrm{d}\mathbf{r} f(\mathbf{r}')g(\mathbf{r} - \mathbf{r}'), \tag{2.41}$$

so that they read

$$n_\nu(\mathbf{r}) = \sum_{i=1}^{m} \int \mathrm{d}\mathbf{r}' \rho_i(\mathbf{r}')\omega_\nu^i(\mathbf{r} - \mathbf{r}') = \sum_{i=1}^{m} (\rho_i * \omega_\nu^i)(\mathbf{r}), \tag{2.42}$$

where $\rho_i(\mathbf{r})$ denotes the density distribution of species i. Assuming a homogeneous fluid of only one component with uniform density distribution $\rho(\mathbf{r}) \equiv \rho_b$ and radius R the convolution can be performed analytically so that the resulting weighted densities are $n_3 = \frac{4}{3}\pi R^3 \rho_b$, $n_2 = 4\pi R^2 \rho_b$, $n_1 = R\rho_b$, and $n_0 = \rho_b$. Each of these weighted (bulk) densities is equal to the bulk density ρ_b times one of the geometrical properties of a sphere: the volume $V = \frac{4}{3}\pi R^3$, the surface area $A = 4\pi R^2$, the radius R and the Euler characteristic. Due to the symmetry of the uniform density distribution, the vectorial weighted densities $\mathbf{n}_2, \mathbf{n}_1$, resulting from anti-symmetric weight functions, vanish. It should be mentioned that, in the general case the latter usually have finite values. These geometrical measures are called the *fundamental measures* leading to the name of the theory.

The excess free energy functional can be assumed to be a combination of the weighted densities, so that the result is of the form

$$\beta\mathcal{F}_{\text{exc}}[\{\rho_i\}] = \int \mathrm{d}\mathbf{r}\Phi(\{n_\nu(\mathbf{r})\}), \tag{2.43}$$

where $\Phi(\{n_\nu(\mathbf{r})\})$ is given by

$$\Phi(\{n_\nu(\mathbf{r})\}) = f_1(n_3)n_0+f_2(n_3)n_1n_2+f_3(n_3)\mathbf{n}_1\cdot\mathbf{n}_2+f_4(n_3)n_2^3+f_5(n_3)n_2\mathbf{n}_2\cdot\mathbf{n}_2. \quad (2.44)$$

Here, Φ is not the interaction potential $\phi(r)$ of equation (2.34) but the *excess free energy density*. Each product of the weighted densities has the dimension $[\text{length}]^{-3}$ corresponding to a density so that the functions $f_j(n_3)$ with $j = 1, \ldots, 5$ need to be dimensionless and thus, depend only on the dimensionless scalar $n_3(\mathbf{r})$. The functional dependence results from the fact that they have to recover the previously mentioned low density limit of equation (2.32) truncated after the first term. In order to deduce the $f_j(n_3)$, Rosenfeld started with

$$\lim_{R_i\to\infty}\left(\frac{\mu^i_{\text{exc}}}{V_i}\right) = p, \quad (2.45)$$

where $V_i = \frac{4}{3}\pi R_i^3$ is the volume of a sphere with radius R_i and p is the pressure in the system. The excess chemical potential μ^i_{exc} can be extracted from equation (2.15) in combination with the ansatz of equation (2.43) to be

$$\mu^i_{\text{exc}} = \frac{\partial\Phi}{\partial\rho_i} = \sum_\nu \frac{\partial\Phi}{\partial n_\nu}\frac{\partial n_\nu}{\partial\rho_i}, \quad (2.46)$$

with ν denoting the scalar and vectorial functions. In the limit of infinite radii R_i, the only non-vanishing term in equation (2.45) is the first of the sum, so that $p = \frac{\partial\Phi}{\partial n_3}$. Substituting the pressure $p = -\frac{\partial F}{\partial V}$ with $F = \mathcal{F}[\rho]$ from equations (2.21), (2.43), and (2.44) results in a differential equation

$$\frac{\partial\Phi}{\partial n_3} = -\Phi + \sum_\nu \frac{\partial\Phi}{\partial n_\nu}n_\nu + n_0. \quad (2.47)$$

Solving this yields the prefactors of the excess free energy density (2.44)

$$\begin{aligned} f_1(n_3) &= -\ln(1-n_3), \\ f_2(n_3) &= \frac{1}{1-n_3}, \\ f_3(n_3) &= -\frac{1}{1-n_3}, \\ f_4(n_3) &= \frac{1}{24\pi(1-n_3)^3}, \\ f_5(n_3) &= -\frac{3}{24\pi(1-n_3)^3}. \end{aligned} \quad (2.48)$$

In conclusion, the excess free energy can be written as a sum of three parts $\Phi = \Phi_1+\Phi_2+\Phi_3$ with

$$\Phi_1 = -n_0\ln(1-n_3), \quad (2.49)$$

$$\Phi_2 = \frac{n_1n_2 - \mathbf{n}_1\cdot\mathbf{n}_2}{1-n_3}, \quad (2.50)$$

and

$$\Phi_3 = \frac{n_2^3 - 3n_2\mathbf{n}_2 \cdot \mathbf{n}_2}{24\pi(1-n_3)^2}. \tag{2.51}$$

One year after Rosenfeld, Kierlik and Rosinberg derived a different version of DFT [35] which was shown later [36] to be an alternative deconvolution of the Mayer function with the same results. As both theories fail to treat the freezing transition of single component hard sphere systems, further improvements were necessary. The approach was to reduce the results to lower dimensions in space, due to the fact that a crystal can be interpreted as particles confined to cavities created by the surrounding particles. This so called *dimensional crossover* [37, 38] leads to an empirical modification of the third term in Rosenfeld's excess free energy Φ_3. A further development was then performed by Tarazona and Rosenfeld [39, 40] yielding an additional tensorial weight function

$$\hat{\boldsymbol{\omega}}_2^i(r) = \left(\frac{\mathbf{r}\mathbf{r}}{r^2} - \frac{\hat{\mathbf{1}}}{3}\right)\omega_2^i(r), \tag{2.52}$$

including the dyadic product $\mathbf{r}\mathbf{r}$ and the unit matrix $\hat{\mathbf{1}}$. Hence, the third term Φ_3 can be amended to

$$\Phi_3 = \left[n_2^3 - 3n_2\mathbf{n}_2 \cdot \mathbf{n}_2 + \frac{9}{2}\left(\mathbf{n}_2\hat{\mathbf{n}}_2\mathbf{n}_2 - \mathrm{Tr}(\hat{\mathbf{n}}_2^3)\right)\right] \cdot \frac{1}{24\pi(1-n_3)^3}, \tag{2.53}$$

where $\mathrm{Tr}(\hat{\mathbf{m}}) = \sum\limits_j m_{jj}$ denotes the classical trace of a matrix $\hat{\mathbf{m}}$ with components m_{ij}.

Indeed, this version of FMT gives a good description of freezing but further improvements have been performed [41–43] leading to the White Bear Mark II functional which recovers surface tensions [44] or adsorption at walls [43] correctly.

2.3.3 Fundamental Measure Theory for hard disks

At first glance, it is a confusing feature of the original approach of Rosenfeld, that it well describes three-dimensional systems but fails for two dimensions [45, 46]. For the latter the exact deconvolution of the Mayer function (see equation (2.38)) requires an infinite number of weight functions [47,48]. In this section a recent approach [49] will be sketched out to obtain a density functional which describes the hard disk solid phase in an appropriate way. The path to follow was explained by Tarazona and Rosenfeld [39, 50] already more than twenty years ago. The Gauss-Bonnet theorem is used to perform the deconvolution of the Mayer function in analogy to equation (2.38) but with an additional tensorial term, similar to the one in the improved three-dimensional functional. This results in

$$-f_{ij}(r) = \omega_2^i \otimes \omega_0^j + \omega_0^i \otimes \omega_2^j + C_0\omega_1^i \otimes \omega_1^j + C_1\boldsymbol{\omega}_1^i \otimes \boldsymbol{\omega}_1^j + C_2\hat{\boldsymbol{\omega}}_1^i \otimes \hat{\boldsymbol{\omega}}_1^j, \tag{2.54}$$

with $C_0 = \pi/2$, $C_1 = -1$, and $C_2 = -\pi/4$, and the weight functions given in analogy to equation (2.39) by

$$\begin{aligned}
\omega_2^i(r) &= \theta(R_i - r), \\
\omega_1^i(r) &= \delta(R_i - r), \\
\omega_0^i(r) &= \frac{1}{\pi\sigma_i}\omega_1^i(r) = \frac{1}{\pi\sigma_i}\delta(R_i - r), \\
\boldsymbol{\omega}_1^i(r) &= \frac{\mathbf{r}}{r}\omega_1^i(r) = \frac{\mathbf{r}}{r}\delta(R_i - r), \text{and} \\
\hat{\boldsymbol{\omega}}_1^i(r) &= \frac{\mathbf{rr}}{r^2}\omega_1^i(r) = \frac{\mathbf{rr}}{r^2}\delta(R_i - r).
\end{aligned} \tag{2.55}$$

Similar to the three-dimensional case, the first three weight functions are scalars, whereas $\boldsymbol{\omega}_1^i(r)$ is a vector and $\hat{\boldsymbol{\omega}}_1^i(r)$ is a matrix containing the dyadic product $\mathbf{rr}$.

As in the three-dimensional system, the excess free energy $\mathcal{F}_{\text{exc}}$ can be expressed by the integral of the excess free energy density Φ (see equation (2.43)). Φ is assumed to be a linear combination of weight functions $n_\nu = \sum_i (\rho_i * \omega_\nu^i)$,

$$\Phi = f(n_2)n_0 + g_0(n_2)\tilde{C}_0(n_1)^2 + g_1(n_2)\tilde{C}_1\mathbf{n}_1 \cdot \mathbf{n}_1 + g_2(n_2)\tilde{C}_2\hat{\mathbf{n}}_1\hat{\mathbf{n}}_1, \tag{2.56}$$

where f and g_j, $(j = 0, 1, 2)$ depend only on the packing fraction n_2. The tensor product $\hat{\mathbf{n}}_1\hat{\mathbf{n}}_1$ is defined as the trace of the matrix product. Hence, the ansatz is the same as Rosenfeld's in equation (2.45), so that with $g_j \equiv g$, Φ becomes

$$\Phi = -n_0 \ln(1 - n_2) + \frac{1}{4\pi(1 - n_2)} \left[\tilde{C}_0(n_1)^2 + \tilde{C}_1\mathbf{n}_1 \cdot \mathbf{n}_1 + \tilde{C}_2\hat{\mathbf{n}}_1\hat{\mathbf{n}}_1\right]. \tag{2.57}$$

The remaining work is now to find the coefficients $\tilde{C}_l$ $(l = 1, 2, 3)$ such that Φ on the one hand recovers the correct second virial coefficient and on the other hand describes the low density limit correctly. Resulting from this two equations $2C_0 + C_1 = 2$ and $C_0 + C_1 + C_2 = 0$ can be written down and solved with a parameter b as

$$\tilde{C}_0 = \frac{b+2}{3}, \qquad \tilde{C}_1 = \frac{b-4}{3}, \text{ and } \tilde{C}_2 = \frac{2-2b}{3}, \tag{2.58}$$

where the b is chosen such that the results fit best to the Mayer function. The optimized value of $b = \frac{11}{4}$ leads to the concluding excess free energy density given by

$$\Phi = -n_0 \ln(1 - n_2) + \frac{1}{4\pi(1 - n_2)} \left(\frac{19}{12}(n_1)^2 - \frac{5}{12}\mathbf{n}_1 \cdot \mathbf{n}_1 - \frac{7}{6}\hat{\mathbf{n}}_1\hat{\mathbf{n}}_1\right). \tag{2.59}$$

2.3.4 Fundamental Measure Theory for a colloid-polymer mixture

Colloid-polymer mixtures are two-component systems with non-additive particles. A simple model invented by Asakura, Oosawa [9, 10] and improved by Vrij [11] can be written down. It describes the main properties adequately. The interaction between two colloids, and a colloid and a polymer is the same as for hard spheres (see equation (2.34)). Polymers are treated ideally, or in other words they do not interact with other polymers. In this section, the derivation of a density functional for this AO-model by Schmidt et al. [13,51] will be sketched out. The Hamiltonian for this kind of system contains the kinetic energy similar to equation (2.2), the external potential, and a sum of interaction terms given by

$$U(\mathbf{r}_j^{\mathrm{c}}, \mathbf{r}_k^{\mathrm{p}}) = \sum_{j<k}^{N_c} \phi_{\mathrm{cc}}(|\mathbf{r}_j^{\mathrm{c}} - \mathbf{r}_k^{\mathrm{c}}|) + \sum_{j}^{N_{\mathrm{c}}} \sum_{k}^{N_{\mathrm{p}}} \phi_{\mathrm{cp}}(|\mathbf{r}_j^{\mathrm{c}} - \mathbf{r}_k^{\mathrm{p}}|) + \sum_{j<k}^{N_{\mathrm{p}}} \phi_{\mathrm{pp}}(|\mathbf{r}_j^{\mathrm{p}} - \mathbf{r}_k^{\mathrm{p}}|). \tag{2.60}$$

Here the $\mathbf{r}^{\mathrm{c}}$ are the positions of the N_{c} colloids of radius R_{c} and the $\mathbf{r}^{\mathrm{p}}$ express the positions of the N_{p} polymers with gyration radius R_{p} in the system. Moreover, the ϕ_{mn} are the interaction potentials of the three combinations of particles $m, n \in \{\mathrm{c}, \mathrm{p}\}$, where the model is defined such that $\phi_{\mathrm{pp}} \equiv 0$, i.e. the last term vanishes. The only adjustable parameter is the size ratio $q = R_{\mathrm{p}}/R_{\mathrm{c}}$. In the zero-dimensional limit, a cavity can either hold no particles, a single colloid or an arbitrary number of polymers. This leads to the grand canonical partition sum given by

$$\Xi = 1 + z_{\mathrm{c}} + (e^{z_{\mathrm{p}}} - 1) = z_{\mathrm{c}} + e^{z_{\mathrm{p}}}, \tag{2.61}$$

with the accessible volume times the fugacities

$$\begin{aligned} z_{\mathrm{p}} &= \frac{\eta_{\mathrm{p}}}{1 - \eta_{\mathrm{c}}}, \\ z_{\mathrm{c}} &= \frac{\eta_{\mathrm{c}}}{1 - \eta_{\mathrm{c}}}\, e^{z_{\mathrm{p}}}. \end{aligned} \tag{2.62}$$

In these expressions the packing fractions of colloids $\eta_{\mathrm{c}} = \frac{4}{3}\pi R_c^3 \frac{N_{\mathrm{c}}}{V}$ and polymers $\eta_{\mathrm{p}} = \frac{4}{3}\pi R_{\mathrm{p}}^3 \frac{N_{\mathrm{p}}}{V}$ are included, where V is the accessible volume of the system. Accordingly, the excess free energy of the zero dimensional limit $F_{0\mathrm{D}}$ can be calculated as

$$\beta F_{0\mathrm{D}}(\eta_{\mathrm{c}}, \eta_{\mathrm{p}}) = (1 - \eta_{\mathrm{c}} - \eta_{\mathrm{p}}) \ln(1 - \eta_{\mathrm{c}}) + \eta_{\mathrm{c}}. \tag{2.63}$$

Based on this result and a low density expansion in analogy to equation (2.32) the excess free energy becomes

$$\beta \mathcal{F}_{\mathrm{exc}}[\rho_{\mathrm{c}}, \rho_{\mathrm{p}}] = \int \mathrm{d}\mathbf{r}\ \Phi(n_\nu^{\mathrm{c}}, n_\nu^{\mathrm{p}}), \tag{2.64}$$

including the weighted densities for each species $i = \mathrm{c}, \mathrm{p}$ from a convolution

$$n_\nu^i(\mathbf{r}) = \int \mathrm{d}\mathbf{r}' \rho_i(\mathbf{r}')\omega_\nu^i(\mathbf{r} - \mathbf{r}'), \tag{2.65}$$

where the weight functions are similar to those of a hard sphere system, defined in equation (2.39). Apparently, the radius R has to be replaced by the radius of the corresponding species. With the knowledge of the expansion of the original FMT by Rosenfeld, also the tensorial term of second rank is included, so that the excess free energy density $\Phi = \Phi_1 + \Phi_2 + \Phi_3$ becomes,

$$\Phi_1 = \sum_{i=\mathrm{c,p}} n_0^i \varphi^i(n_3^{\mathrm{c}}, n_3^{\mathrm{p}}), \tag{2.66}$$

$$\Phi_2 = \sum_{i,j=\mathrm{c,p}} (n_1^i n_2^j - \mathbf{n}_1^1 \cdot \mathbf{n}_2^j)\varphi^{ij}(n_3^{\mathrm{c}}, n_3^{\mathrm{p}}), \tag{2.67}$$

$$\Phi_3 = \sum_{i,j,k=\mathrm{c,p}} \left(\frac{1}{3} n_2^i n_2^j n_2^k - n_2^i \mathbf{n}_2^j \cdot \mathbf{n}_2^k + \frac{3}{2}\left[\mathbf{n}_2^i \hat{\mathbf{n}}_2^j \mathbf{n}_2^k - \mathrm{Tr}(\hat{\mathbf{n}}_2^i \hat{\mathbf{n}}_2^j \hat{\mathbf{n}}_2^k)\right]\right) \varphi^{ijk}(n_3^{\mathrm{c}}, n_3^{\mathrm{p}}). \tag{2.68}$$

In this description, $\varphi^{i\ldots k}(\eta_{\mathrm{c}}, \eta_{\mathrm{p}}) = \frac{\partial^m}{\partial\eta_i \ldots\ldots \partial\eta_k} \beta F_{0\mathrm{D}}(\eta_{\mathrm{c}}, \eta_{\mathrm{p}})$ are the derivatives of the zero dimensional free energy obtained from equation (2.63), where the packing fraction in zero dimensions is the analog to n_3 in three dimensions. Hence the $\varphi^{i\ldots k}$ are given by

$$\begin{aligned}
\varphi^{\mathrm{c}} &= -\ln(1 - n_3^{\mathrm{c}}) + \frac{n_3^{\mathrm{p}}}{1 - n_3^{\mathrm{c}}}, \\
\varphi^{\mathrm{p}} &= -\ln(1 - n_3^{\mathrm{c}}), \\
\varphi^{\mathrm{cc}} &= \frac{1 - n_3^{\mathrm{c}} + n_3^{\mathrm{p}}}{(1 - n_3^{\mathrm{c}})^2}, \\
\varphi^{\mathrm{cp}} &= \frac{1}{1 - n_3^{\mathrm{c}}}, \\
\varphi^{\mathrm{ccc}} &= \frac{1 - n_3^{\mathrm{c}} + 2n_3^{\mathrm{p}}}{(1 - n_3^{\mathrm{c}})^3}, \\
\varphi^{\mathrm{ccp}} &= \frac{1}{(1 - n_3^{\mathrm{c}})^2}, \\
\varphi^{\mathrm{cccc}} &= \frac{2 - 2n_3^{\mathrm{c}} + 6n_3^{\mathrm{p}}}{(1 - n_3^{\mathrm{c}})^4}, \\
\varphi^{\mathrm{cccp}} &= \frac{2}{(1 - n_3^{\mathrm{c}})^3}, \\
\varphi^{\mathrm{pp}} &= \varphi^{\mathrm{cpp}} = \varphi^{\mathrm{ppp}} = \varphi^{\mathrm{ccpp}} = 0.
\end{aligned} \tag{2.69}$$

It should be mentioned that all derivatives with two or more $ij = \mathrm{p}$ are zero because interactions between polymers would otherwise arise. The fourth order derivatives are required for the minimization performed in chapter 3 where derivatives of Φ from equation (2.68) with respect to the weighted densities have to be calculated.

2.4 Dynamical Density Functional Theory

Knowing the equilibrium properties of many-body systems, the dynamical behavior of these systems is interesting to study. Several approaches have been made to describe the density dependence on time $\rho(\mathbf{r}, t)$ since the 1970's [18, 52, 53]. Based on the theory of spinodal decomposition [54], a particle current $\mathbf{j}(\mathbf{r}, t)$ due to a spatial gradient of the chemical potential μ is assumed as

$$\mathbf{j}(\mathbf{r}, t) = -\Gamma \rho(\mathbf{r}, t) \nabla \mu(\mathbf{r}, t), \tag{2.70}$$

with a time-dependent density distribution $\rho(\mathbf{r}, t)$, a chemical potential $\mu(\mathbf{r}, t)$, and a mobility constant Γ. Linking the results to equilibrium DFT, the gradient can be expressed by a functional derivative (compare with equation (2.23)) as

$$\mu(\mathbf{r}, t) = \frac{\delta \mathcal{F}_{\text{exc}}[\rho(\mathbf{r}, t)]}{\delta \rho(\mathbf{r}, t)} + V_{\text{ext}}(\mathbf{r}, t). \tag{2.71}$$

In combination with the continuity equation

$$\frac{\partial \rho(\mathbf{r}, t)}{\partial t} = -\nabla \cdot \mathbf{j}(\mathbf{r}, t), \tag{2.72}$$

a basis for a dynamical density functional theory (DDFT) is given. However, no convincing proof was published until 1999 when Marconi and Tarazona [55] derived a deterministic DDFT starting from Langevin stochastic equations of motion for Brownian particles in the large friction limit. This derivation was revisited by Archer and Evans [56] in 2004. In this section the focus will lie on the latter approach to give an introduction to DDFT. The starting point is the Smoluchowski equation for N Brownian particles which is a generalized diffusion equation

$$\frac{\partial P(\mathbf{r}^N, t)}{\partial t} = \Gamma \sum_{i=1}^{N} \nabla_i \left(k_B T \nabla_i + \nabla_i (U(\mathbf{r}^N, t) + V_{\text{ext}}(\mathbf{r}^N, t)\right) P(\mathbf{r}^N, t), \tag{2.73}$$

where $P(\mathbf{r}^N, t)$ is the probability density distribution depending on the particle positions $\mathbf{r}^N = (\mathbf{r}_1, \ldots, \mathbf{r}_N)$ and time t. ∇ denotes the nabla-operator $\nabla = \hat{\mathbf{e}}_x \frac{\partial}{\partial x} + \hat{\mathbf{e}}_y \frac{\partial}{\partial y} + \hat{\mathbf{e}}_z \frac{\partial}{\partial z}$ with the three unit vectors $\hat{\mathbf{e}}_j$, $j = x, y, z$. Integrating the probability density distribution leads to the one-body density $\rho^{(1)}(\mathbf{r}_1, t)$ with

$$\rho^{(1)}(\mathbf{r}_1, t) = N \int \mathrm{d}\mathbf{r}_2 \ldots \int \mathrm{d}\mathbf{r}_N P(\mathbf{r}^N, t), \tag{2.74}$$

or more general the n-particle density

$$\rho^{(n)} = \frac{N!}{(N-n)!} \int \mathrm{d}\mathbf{r}_{n+1} \ldots \int \mathrm{d}\mathbf{r}_N P(\mathbf{r}^N, t). \tag{2.75}$$

The interaction potential $U(\mathbf{r}^N, t)$ can be written as a sum of two-body ($\phi_2(\mathbf{r}_i, \mathbf{r}_j, t)$), three-body ($\phi_3(\mathbf{r}_i, \mathbf{r}_j, \mathbf{r}_k, t)$) and higher body interactions to be

$$U(\mathbf{r}^N, t) = \frac{1}{2} \sum_{j \neq i} \sum_{i=1}^{N} \phi_2(\mathbf{r}_i, \mathbf{r}_j, t) + \frac{1}{6} \sum_{k \neq j \neq i} \sum_{j \neq i} \sum_{i=1}^{N} \phi_3(\mathbf{r}_i, \mathbf{r}_j, \mathbf{r}_k, t) + \ldots \ . \tag{2.76}$$

Thus, it can be inserted into the Smoluchowski equation (2.73) so that the result becomes

$$\begin{aligned} \frac{1}{\Gamma} \frac{\partial \rho^{(1)}(\mathbf{r}_1, t)}{\partial t} =& k_B T \nabla_1^2 \rho^{(1)}(\mathbf{r}_1, t) + \nabla_1 \left(\rho^{(1)}(\mathbf{r}_1, t) \nabla_1 V_{\text{ext}}(\mathbf{r}_1, t) \right) \\ &+ \nabla_1 \int \mathrm{d}\mathbf{r}_2 \rho^{(2)}(\mathbf{r}_1, \mathbf{r}_2, t) \nabla_1 \phi_2(\mathbf{r}_1, \mathbf{r}_2, t) \\ &+ \nabla_1 \int \mathrm{d}\mathbf{r}_2 \int \mathrm{d}\mathbf{r}_3 \rho^{(3)}(\mathbf{r}_1, \mathbf{r}_2, \mathbf{r}_3, t) \nabla_1 \phi_3(\mathbf{r}_1, \mathbf{r}_2, \mathbf{r}_3, t) \\ &+ \ldots \end{aligned} \tag{2.77}$$

In the case of only two-body interaction, it is known [18], that in a fluid the two-particle density is coupled to the one-body correlation function via

$$k_B T \rho(\mathbf{r}) \nabla c^{(1)}(\mathbf{r}) = \int \mathrm{d}\mathbf{r}' \rho^{(2)}(\mathbf{r}, \mathbf{r}') \nabla \phi_2(\mathbf{r}, \mathbf{r}'), \tag{2.78}$$

what can be generalized to many-body interactions. Additionally, relation (2.24) is repeated to give a link between the one-body correlation function and the excess free energy functional

$$c^{(1)}(\mathbf{r}) = -\beta \frac{\delta \mathcal{F}_{\text{exc}}[\rho(\mathbf{r})]}{\delta \rho(\mathbf{r})}. \tag{2.79}$$

Both equations hold only for the equilibrium fluid, but it is assumed here that they shall be valid for the non-equilibrium case too. Merging equation (2.77), truncated after the third summand due to the restriction of no higher than two-body interaction, (2.78), and (2.79), and labeling the one-particle density $\rho^{(1)}(\mathbf{r}, t) = \rho(\mathbf{r}, t)$, the DDFT equation can be obtained

$$\frac{\partial \rho(\mathbf{r}, t)}{\partial t} = \Gamma \nabla \left[\rho(\mathbf{r}, t) \nabla \frac{\delta \Omega[\rho(\mathbf{r}, t)]}{\delta \rho(\mathbf{r}, t)} \right]. \tag{2.80}$$

CHAPTER 3

Colloid-polymer mixtures in external fields

The results of this chapter have been published in [1]. Thus, this chapter contains calculations from density functional theory and simulations performed by Richard L. C. Vink. Hartmut Löwen combined the findings of both approaches. This chapter deals with a binary mixture of colloids and polymers, where the colloids are sterically stabilized and the polymers are not adsorbing to the colloids. Accordingly, colloids are interacting via a hard-body potential (compare with equation (2.34) in section 2.3.2) which is affected by the polymers to become an attractive depletion interaction. By integrating out the effect of the polymers, an effective potential can be obtained [9, 12]. This system has been studied using experiments, computer simulations, and theory [57–62] to learn about liquid-vapor demixing. The usage of a binary mixture as a model system also led to the understanding of interfacial phenomena [63–66], wetting [67–70], capillary waves [71,72], gelation [73], equilibrium clustering [74], and attractive glasses [75, 76].

As already mentioned in section 2.3.4, a simple model to describe this binary mixture is the Asakura-Oosawa model (AO). It contains the essential physics [59, 61] and provides a tool for theoretical predictions [13, 51] and computer simulations [77, 78] resulting in a liquid-vapor critical point in bulk [58] and a freezing transition [79]. Further investigations are the effects of a single wall [80, 81] or two parallel planar walls [82–87], and wetting [88–90] or phase separation in porous media [85, 91–95]. The addition of an external field as gravity [96, 97] or a periodic field [14] gives rise to some new phenomena.

In this chapter, the work of Götze et al. [14] sets the starting point, where the external field is a standing wave of wavelength λ induced by a laser-beam in one direction, the z-direction in the following. Knowing the effect of the field on the freezing of this system, the so-called *laser-induced freezing* [98, 99], the focus shall now be laid on the liquid-vapor transition. Götze et al. used density functional theory (see section 2.3.4) and found a spatially varying phase consisting of slabs of high and low dense colloidal regions, named the *zebra*-phase.

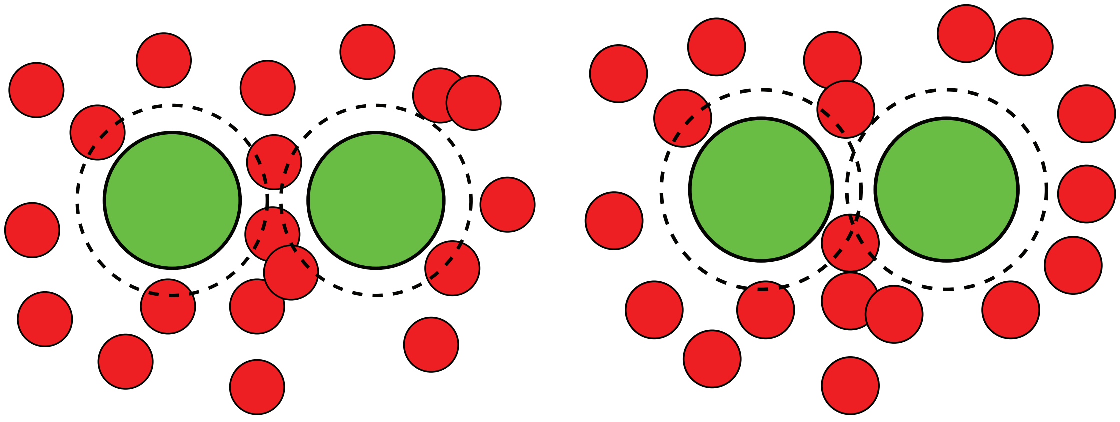

(a) no overlap (b) overlap

Figure 3.1: *Sketch of the AO model for two different configurations. Colloids are plotted in green with a dashed line denoting the restricted area for polymers which are plotted as ideal red spheres. In (a) no interaction of the colloids occurs, whereas in (b) the colloids feel an attractive potential due to entropy.*

3.1 System

In order to describe the system, the AO-model shall be repeated briefly. The system consists of colloids (c) and polymers (p) treated as ideal spheres with diameters σ and σ_{p}. The diameter of the colloids is used as a unit length, whereas the polymer diameter can be calculated via the colloid-to-polymer size ratio $q = \sigma_{\mathrm{p}}/\sigma$. However, the interaction of polymers with other polymers shall be ideal, so that the interaction potentials $\phi_{ij}(r)$ can be written as pair potentials with

$$\phi_{\mathrm{cc}}(r) = \begin{cases} \infty & \text{, for} r < \sigma \\ 0 & \text{, otherwise,} \end{cases} \tag{3.1}$$

$$\phi_{\mathrm{cp}}(r) = \begin{cases} \infty & \text{, for} r < (\sigma + \sigma_{\mathrm{p}})/2 \\ 0 & \text{, otherwise,} \end{cases} \tag{3.2}$$

$$\phi_{\mathrm{pp}}(r) = 0, \tag{3.3}$$

and the particles center-to-center distances r.

Due to these pair potentials, there is a restricted area around each colloid, where polymers cannot occur. If the center-to-center distance of two colloids is larger than their diameter plus the diameter of a polymer ($r > \sigma + \sigma_{\mathrm{p}}$), these regions will not overlap (see figure 3.1(a)) and hence, the two colloids will not interact. In this case, polymers are pushing the colloids randomly from all directions. When in contrast to this the distance is smaller than $\sigma + \sigma_{\mathrm{p}}$, but larger than the diameter σ (see figure 3.1(b)), the forbidden area for polymers will be decreased. This gain of entropy adds an attractive part to the

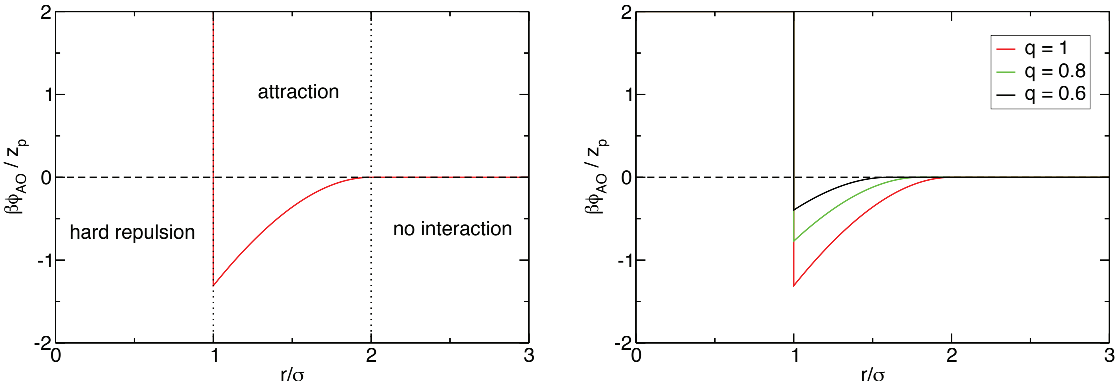

(a) regions of different interactions

(b) different values of q

Figure 3.2: *Effective interaction potential of the AO model with $\sigma = 1$, showing the three regions of hard repulsion, attraction, and no interaction for a size ratio $q = 1$ in (a) and a comparison of different values of q, $q = 1$, 0.8, and 0.6, in (b).*

interaction of the colloids. In conclusion, the effect of the polymers on the colloids can be written as an effective interaction potential [9]

$$\beta\phi_{\mathrm{AO}}(r) = \begin{cases} -\frac{\pi(1+q)^3\sigma^3 z_{\mathrm{p}}}{6}\left(1+\frac{r^3}{2(1+q)^3\sigma^3}-\frac{3r}{2(1+q)\sigma}\right) & \text{, for}\sigma < r < \sigma+\sigma_{\mathrm{p}} \\ 0 & \text{, for}r > \sigma+\sigma_p, \end{cases} \tag{3.4}$$

with the fugacity of the polymers $z_{\mathrm{p}} = \frac{1}{\Lambda_{\mathrm{p}}^3}e^{\beta\mu_{\mathrm{p}}}$. Obviously, particle distances smaller than the colloid diameter σ are restricted due to the hard-body interaction. The resulting potential is shown in figure 3.2(a), where the three regions of different interactions are illustrated for colloids and polymers of the same size ($q = 1$). In figure 3.2(b), three different values for the size ratio q are compared. The smaller the polymers are, or in other words the smaller q is, the more the attractive interaction range decreases and the more the minimum value of ϕ_{AO} increases. In this case, the polymers have less effect on the colloids, so that in the limes of vanishing diameter of the polymers, the system is a pure hard sphere mixture of colloids.

As common in DFT, all calculations are performed in the grand canonical ensemble, with fixed temperature T, system volume V, and chemical potentials μ_{c} and μ_{p}. Particle exchange occurs with a heat bath, so that the particle numbers N_{c} and N_{p} defining the particle densities $\rho_{\mathrm{c}} = N_{\mathrm{c}}/V$ and $\rho_{\mathrm{p}} = N_{\mathrm{p}}/V$ vary. In order to have a system invariant quantity, the packing fraction for the colloids is defined as $\eta_{\mathrm{c}} = \rho_{\mathrm{c}}\pi\sigma^3/6$. Sticking to a convention [58], the polymer reservoir packing fraction $\eta_{\mathrm{p}}^{\mathrm{r}} = \rho_{\mathrm{p}}\pi\sigma_{\mathrm{p}}^3/6$ is used instead of the chemical potential of the colloids, as it can be identified as the packing fraction of a pure polymer system at chemical potential μ_{p}. For the AO model, this is simply an ideal gas, because of no interaction of the polymers, what means that the reservoir packing fraction is $\eta_{\mathrm{p}}^{\mathrm{r}} \propto e^{\mu_{\mathrm{p}}/k_B T}$.

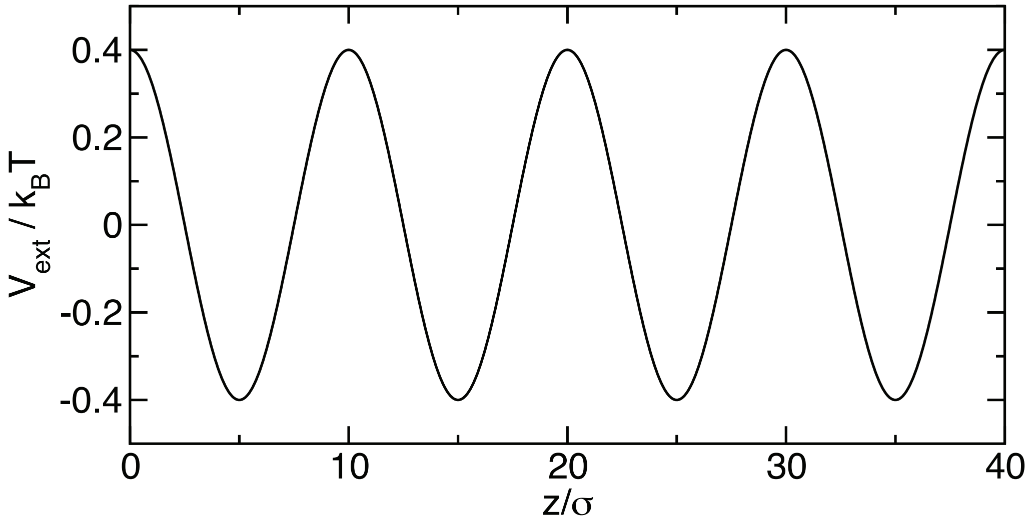

Figure 3.3: *External periodic potential* $V_{\text{ext}}(z)$ *given by equation* (3.5)*, with amplitude* $V_0 = 0.4k_BT$ *and wavelength* $\lambda = 10\sigma$*.*

Picking up the work of Götze et al. [14], the system is examined under the presence of an external potential along the z-direction given by

$$V_{\text{ext}}(z) = V_0 \cos\left(\frac{2\pi z}{\lambda}\right), \tag{3.5}$$

with the field specified by its amplitude V_0 and wavelength λ. In figure 3.3 an exemplary potential is plotted for $V_0 = 0.4k_BT$ and $\lambda = 10\sigma$.

In this work the given external potential is only acting on the colloids, whereas the polymers are only interacting with the colloids.

3.2 Density Functional Theory

In order to perform DFT calculations, the previously presented theory of section 2.3.4 can be used as a starting point. Hence, the grand canonical free energy

$$\Omega(T, \mu_{\text{c}}, \eta_{\text{p}}^{\text{r}}, [\rho_{\text{c}}(z), \rho_{\text{p}}(z)]) \tag{3.6}$$

has to be minimized. Here the $\rho_i(z)$ describe the density distributions depending only on the spatial z-component, where the other coordinates have been integrated out. Therefore, the excess free energy density of equation (2.68) $\Phi = \Phi_1 + \Phi_2 + \Phi_3$ can be rewritten with

$$\Phi_1 = \frac{1}{\pi\sigma^2} n_2^c \varphi^c + \frac{1}{\pi\sigma_{\text{p}}^2} n_2^p \varphi^p, \tag{3.7}$$

$$\Phi_2 = \underbrace{\frac{1}{2\pi\sigma}((n_2^c)^2 - (\mathbf{n}_2^c)^2)}_{=:A}\,\varphi^{cc} + \underbrace{\left(\frac{1}{2\pi\sigma} + \frac{1}{2\pi\sigma_\mathrm{p}}\right)(n_2^c n_2^p - \mathbf{n}_2^c \mathbf{n}_2^p)}_{=:B}\,\varphi^{cp}, \tag{3.8}$$

and

$$\begin{aligned}\Phi_3 = \frac{1}{8\pi}\Bigg\{ & \underbrace{\left(\frac{(n_2^\mathrm{c})^3}{3} - n_2^\mathrm{c}(\mathbf{n}_2^\mathrm{c})^2 + \frac{3}{2}\left[(\mathbf{n}_2^\mathrm{c})^2\,\hat{\mathbf{n}}_2^\mathrm{c} - (\hat{\mathbf{n}}_2^\mathrm{c})^3\right]\right)}_{=:C}\varphi^\mathrm{ccc} \\ & + \underbrace{\left((n_2^\mathrm{c})^2 n_2^\mathrm{p} - 2n_2^\mathrm{c}\mathbf{n}_2^\mathrm{c}\mathbf{n}_2^\mathrm{p} - n_2^\mathrm{p}(\mathbf{n}_2^\mathrm{c})^2 + \frac{3}{2}\left[2\mathbf{n}_2^\mathrm{c}\mathbf{n}_2^\mathrm{p}\hat{\mathbf{n}}_2^\mathrm{c} + (\mathbf{n}_2^\mathrm{c})^2\,\hat{\mathbf{n}}_2^\mathrm{p} - 3\,(\hat{\mathbf{n}}_2^\mathrm{c})^2\,\hat{\mathbf{n}}_2^\mathrm{p}\right]\right)}_{=:D}\varphi^\mathrm{ccp}\Bigg\},\end{aligned} \tag{3.9}$$

where the vector weighted densities $\mathbf{n}_{1,2}^\mathrm{c,p}$ and the tensorial weighted densities $\hat{\mathbf{n}}_2^\mathrm{c,p}$ have only one component. The derivatives of the zero-dimensional free energy φ^ν are similar to those defined in equation (2.69).

In order to minimize the grand canonical free energy, the excess free energy functional has to be derived by the density. This derivation can be simplified to a convolution by using

$$\begin{aligned}\beta\frac{\delta\mathcal{F}_\mathrm{exc}}{\delta\rho_i(\mathbf{r})} &= \int \mathrm{d}\mathbf{x}\frac{\delta\Phi}{\delta\rho_i(\mathbf{r})} \\ &= \sum_\nu \int \mathrm{d}\mathbf{x}\frac{\delta\Phi}{\delta n_\nu^i(\mathbf{x})}\frac{\delta n_\nu^i(\mathbf{x})}{\delta\rho_i(\mathbf{r})} \\ &= \sum_\nu \int \mathrm{d}\mathbf{x} T_\nu^i(\mathbf{x})\omega_\nu^i(\mathbf{x}-\mathbf{r}) \\ &= \sum_\nu \int \mathrm{d}\mathbf{x} T_\nu^i(\mathbf{x})\xi_\nu\omega_\nu^i(\mathbf{r}-\mathbf{x}) \\ &= \sum_\nu \xi_\nu\left(T_\nu^i \otimes \omega_\nu^i\right)(\mathbf{r}),\end{aligned} \tag{3.10}$$

containing the convolution in analogy to equation (2.37) given by

$$(T_\nu^i \otimes \omega_\nu^i)(\mathbf{r}) = \int \mathrm{d}\mathbf{x} T_\nu^i(\mathbf{x})\omega_\nu^i(\mathbf{r}-\mathbf{x}), \tag{3.11}$$

and a factor ξ_ν, which is 1 for symmetric and -1 for antisymmetric weight functions. In this context the only antisymmetric function is the vector weight function $\boldsymbol{\omega}_2^i$. Thus, the functional derivatives T^i_ν are calculated. This results for the colloids in

$$\begin{aligned}
T^{\mathrm{c}}_2 =& \frac{1}{\pi\sigma^2}\varphi^{\mathrm{c}} + \frac{1}{2\pi\sigma}2n^{\mathrm{c}}_2\varphi^{\mathrm{cc}} + \left(\frac{1}{2\pi\sigma} + \frac{1}{2\pi\sigma_{\mathrm{p}}}\right) n^{\mathrm{p}}_2\varphi^{\mathrm{cp}} + \\
&+ \frac{1}{8\pi}\left[\left((n^{\mathrm{c}}_2)^2 - (\mathbf{n}^{\mathrm{c}}_2)^2\right)\varphi^{\mathrm{ccc}} + \left(2n^{\mathrm{c}}_2 n^{\mathrm{p}}_2 - 2\mathbf{n}^{\mathrm{c}}_2\mathbf{n}^{\mathrm{p}}_2\right)\varphi^{\mathrm{ccp}}\right], \\
T^{\mathrm{c}}_3 =& \frac{1}{\pi\sigma^2} n^{\mathrm{c}}_2\varphi^{\mathrm{cc}} + \frac{1}{\pi\sigma_{\mathrm{p}}^2} n^{\mathrm{p}}_2\varphi^{\mathrm{cp}} + A\varphi^{\mathrm{ccc}} + B\varphi^{\mathrm{ccp}} + \frac{1}{8\pi}(C\varphi^{\mathrm{cccc}} + D\varphi^{\mathrm{cccp}}), \\
\mathbf{T}^{\mathrm{c}}_2 =& -\frac{1}{2\pi\sigma}2\mathbf{n}^{\mathrm{c}}_2\varphi^{\mathrm{cc}} - \left(\frac{1}{2\pi\sigma} + \frac{1}{2\pi\sigma_{\mathrm{p}}}\right)\mathbf{n}^{\mathrm{p}}_2\varphi^{\mathrm{cp}} + \\
&+ \frac{1}{8\pi}\left[\left(-2n^{\mathrm{c}}_2\mathbf{n}^{\mathrm{c}}_2 + 3\mathbf{n}^{\mathrm{c}}_2\hat{\mathbf{n}}^{\mathrm{c}}_2\right)\varphi^{\mathrm{ccc}} + \left(-2n^{\mathrm{p}}_2\mathbf{n}^{\mathrm{c}}_2 - 2n^{\mathrm{c}}_2\mathbf{n}^{\mathrm{p}}_2 + 3\mathbf{n}^{\mathrm{c}}_2\hat{\mathbf{n}}^{\mathrm{p}}_2 + 3\mathbf{n}^{\mathrm{p}}_2\hat{\mathbf{n}}^{\mathrm{c}}_2\right)\varphi^{\mathrm{ccp}}\right], \\
\hat{\mathbf{T}}^{\mathrm{c}}_2 =& \frac{3}{16\pi}\left[\left((\mathbf{n}^{\mathrm{c}}_2)^2 - 3(\hat{\mathbf{n}}^{\mathrm{c}}_2)^2\right)\varphi^{\mathrm{ccc}} + \left(2\mathbf{n}^{\mathrm{c}}_2\mathbf{n}^{\mathrm{p}}_2 - 6\hat{\mathbf{n}}^{\mathrm{c}}_2\hat{\mathbf{n}}^{\mathrm{p}}_2\right)\varphi^{\mathrm{ccp}}\right],
\end{aligned} \tag{3.12}$$

and for the polymers in

$$\begin{aligned}
T^{\mathrm{p}}_2 =& \frac{1}{\pi\sigma_{\mathrm{p}}^2}\varphi^{\mathrm{p}} + \left(\frac{1}{2\pi\sigma} + \frac{1}{2\pi\sigma_{\mathrm{p}}}\right) n^{\mathrm{c}}_2\varphi^{\mathrm{cp}} + \frac{1}{8\pi}\left((n^{\mathrm{c}}_2)^2 - (\mathbf{n}^{\mathrm{c}}_2)^2\right)\varphi^{\mathrm{ccp}}, \\
T^{\mathrm{p}}_3 =& \frac{1}{\pi\sigma_{\mathrm{p}}^2} n^{\mathrm{c}}_2\varphi^{\mathrm{cp}} + A\varphi^{\mathrm{ccp}} + \frac{1}{8\pi}C\varphi^{\mathrm{cccp}}, \\
\mathbf{T}^{\mathrm{p}}_2 =& -\left(\frac{1}{2\pi\sigma} + \frac{1}{2\pi\sigma_{\mathrm{p}}}\right)\mathbf{n}^{\mathrm{c}}_2\varphi^{\mathrm{cp}} + \frac{1}{8\pi}\left[-2n^{\mathrm{c}}_2\mathbf{n}^{\mathrm{c}}_2 + 3\mathbf{n}^{\mathrm{c}}_2\hat{\mathbf{n}}^{\mathrm{c}}_2\right]\varphi^{\mathrm{ccp}}, \\
\hat{\mathbf{T}}^{\mathrm{p}}_2 =& \frac{3}{16\pi}\left[(\mathbf{n}^{\mathrm{c}}_2)^2 - 3(\hat{\mathbf{n}}^{\mathrm{c}}_2)^2\right]\varphi^{\mathrm{ccp}},
\end{aligned} \tag{3.13}$$

where the A, B, C, and D are defined in equations (3.8) and (3.9).

In order to simplify the calculations in a one-dimensional system, the convolution of the densities and the three-dimensional weight functions (see equation (2.39)) is recalled

$$\bar{\rho}_{\mathrm{c}}(z) = \int \mathrm{d}\mathbf{r}'\omega_\nu(|\mathbf{r} - \mathbf{r}'|)\rho_{\mathrm{c}}(z'). \tag{3.14}$$

Transforming this to cylindrical coordinates, the modulus is given by $|\mathbf{r} - \mathbf{r}'| = \sqrt{\rho^2 + (z - z')^2}$, so that the previous integral becomes

$$\bar{\rho}_{\mathrm{c}}(z) = \int_{-\infty}^{\infty} \mathrm{d}z' \underbrace{2\pi \int_0^{\infty} \mathrm{d}\rho\rho\omega_\nu(\sqrt{\rho^2 + (z - z')^2})}_{=:\tilde{\omega}_\nu(z - z')} \rho_{\mathrm{c}}(z'), \tag{3.15}$$

where the inner integrals are renamed as new one-dimensional weight functions $\tilde{\omega}_\nu(r)$.

For $|z| > \sigma_i/2$, weight functions vanish but otherwise they become

$$\begin{aligned}
\tilde{\omega}_3^i(z) &= \pi(R_i^2 - z^2)\,\theta(R_i - |z|) \\
\tilde{\omega}_2^i(z) &= 2\pi R_i\,\theta(R_i - |z|) \\
\tilde{\boldsymbol{\omega}}_2^i(z) &= 2\pi z\,\theta(R_i - |z|) \\
\tilde{\hat{\boldsymbol{\omega}}}_2^i(z) &= 2\pi R_i \left(\frac{z^2}{R_i^2} - \frac{1}{3}\right)\,\theta(R_i - |z|),
\end{aligned} \tag{3.16}$$

where the radii $R_i = \sigma_i/2$ are used to emphasize the analogy to section 2.3.2, where also the Heavyside step function $\theta(x)$ is introduced. The fastest way to compute a convolution in one dimension is performed in Fourier space. Known from mathematics, a convolution becomes a multiplication in Fourier space

$$\mathrm{FT}(f \otimes g) = \mathrm{FT}(f) \cdot \mathrm{FT}(g), \tag{3.17}$$

where FT denotes the common d-dimensional Fourier transform

$$\mathrm{FT}(f)(\mathbf{k}) = \frac{1}{\sqrt{(2\pi)^d}} \int\limits_{\mathcal{R}^d} \mathrm{d}^d r\, f(\mathbf{r}) e^{-i\mathbf{k}\cdot\mathbf{r}}. \tag{3.18}$$

Unfortunately, the weight functions shown in equation (3.16) have discontinuities as they contain the Heaviside step function. Consequently, it is better to perform their Fourier transform analytically and multiply the result with the numerical Fourier transform of the densities. The resulting Fourier transforms are given by

$$\begin{aligned}
\mathrm{FT}(\omega_3^i)(k) &= \frac{4\pi}{k^3\sqrt{2\pi}} \left(\sin(kR_i) - kR_i\cos(kR_i)\right) \\
\mathrm{FT}(\omega_2^i)(k) &= \frac{4\pi R_i}{k\sqrt{2\pi}} \sin(kR_i) \\
\mathrm{FT}(\boldsymbol{\omega}_2^i)(k) &= \frac{4\pi i}{k^2\sqrt{2\pi}} \left(kR_i\cos(kR_i) - \sin(kR_i)\right) \\
\mathrm{FT}(\hat{\boldsymbol{\omega}}_2^i)(k) &= \frac{8\pi}{k^3 R_i\sqrt{2\pi}} \left(\left(\frac{k^2R_i^2}{3} - 1\right)\sin(kR_i) + kR_i\cos(kR_i)\right).
\end{aligned} \tag{3.19}$$

Summing all up, the density distribution $\rho_i(z)$ for each of the two species containing the fugacity z_i can be obtained by

$$\rho_i(z) = z_i \exp\left[-\sum_\nu (T_\nu^i \otimes \omega_\nu^i)(z) - \beta V_{\text{ext},i}(z)\right]. \tag{3.20}$$

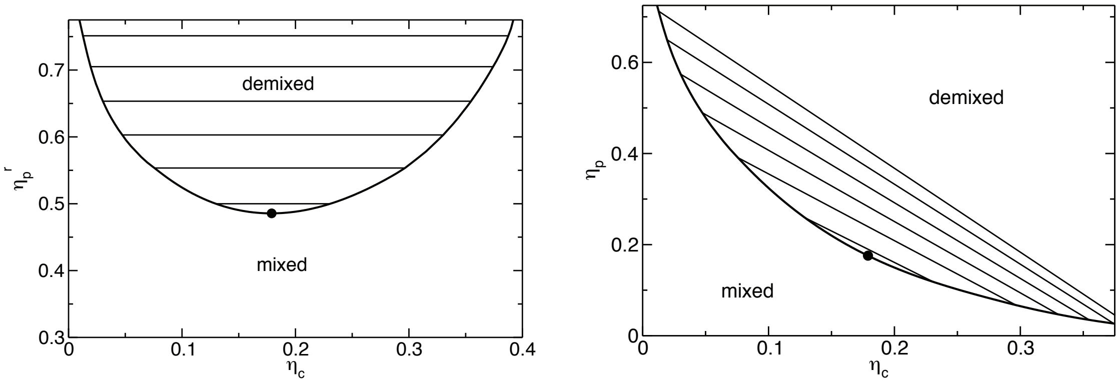

(a) $(\eta_{\mathrm{c}}, \eta_{\mathrm{p}}^{\mathrm{r}})$ representation (b) $(\eta_{\mathrm{c}}, \eta_{\mathrm{p}})$ representation

Figure 3.4: *Bulk phase diagram of the AO model with* $q = 0.6$ *in (a)* $(\eta_{\mathrm{c}}, \eta_{\mathrm{p}}^{\mathrm{r}})$ *representation and (b)* $(\eta_{\mathrm{c}}, \eta_{\mathrm{p}})$ *representation with a thick line illustrating the binodal and straight lines indicating the coexistence configurations. The black dot represents the critical point in each of the two representations.*

3.2.1 Phase diagram

In order to see the effect of the external potential, first a system in absence of any potential, $V_{\mathrm{ext}}(\mathbf{r}) \equiv 0$, is assumed. Accordingly, the density distribution is homogeneous so that $\rho_i(\mathbf{r}) \equiv \rho_i$ at all spatial coordinates $\mathbf{r}$. In analogy to section 2.3.3, the weight functions $w_\nu^i = \int \mathrm{d}\mathbf{r}\omega_\nu^i(\mathbf{r})$ yield the fundamental measures of the particles, namely the volume $w_3^i = \frac{4}{3}\pi R_i^3$ and the surface area $w_2^i = 4\pi R_i^2$, so that the weighted densities n_ν become

$$n_3^i = \frac{4}{3}\pi R_i^3 \rho_i = \eta_i, \quad n_2^i = 4\pi R_i^2 \rho_i = \frac{3\eta_i}{R_i}, \quad \mathbf{n}_2^i = \hat{\mathbf{n}}_2^i = 0, \tag{3.21}$$

where η_i is the packing fraction of species i. The grand canonical free energy per volume V of this system is

$$\frac{\beta}{V}\Omega = \frac{\beta}{V}\mathcal{F}_{\mathrm{exc}} + \rho[\ln\rho + 3\ln(\Lambda_{\mathrm{c}}) - 1 - \beta\mu_{\mathrm{c}}] + \rho_{\mathrm{p}}[\ln\rho_{\mathrm{p}} + 3\ln(\Lambda_{\mathrm{p}}) - 1 - \beta\mu_{\mathrm{p}}], \tag{3.22}$$

and the functional derivatives become

$$\begin{aligned}\frac{\beta}{V}\frac{\delta\Omega}{\delta\rho_c} &= \frac{\beta}{V}\frac{\delta\mathcal{F}_{\mathrm{exc}}}{\delta\rho_{\mathrm{c}}} + \ln\rho_{\mathrm{c}} + 3\ln(\Lambda_{\mathrm{c}}) - \beta\mu_{\mathrm{c}}, \\ \frac{\beta}{V}\frac{\delta\Omega}{\delta\rho_p} &= \frac{\beta}{V}\frac{\delta\mathcal{F}_{\mathrm{exc}}}{\delta\rho_{\mathrm{p}}} + \ln\rho_{\mathrm{p}} + 3\ln(\Lambda_{\mathrm{p}}) - \beta\mu_{\mathrm{p}},\end{aligned} \tag{3.23}$$

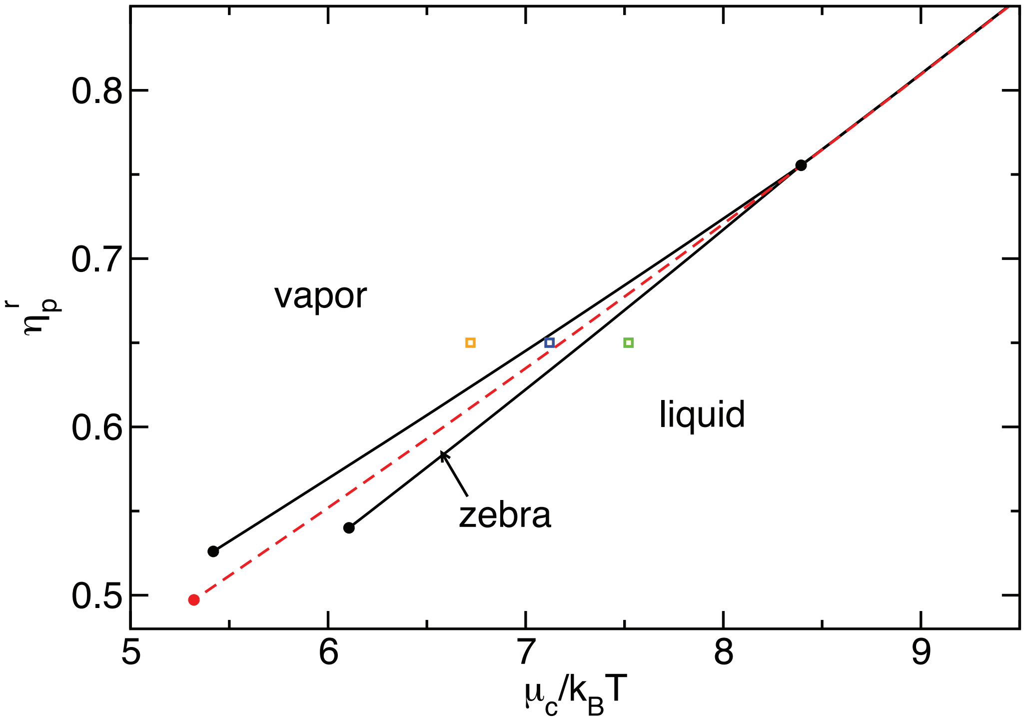

Figure 3.5: *Phase diagram of the AO model with $q = 0.6$ in (μ_c, η_p^r) representation, in an external potential with amplitude $V_0 = 0.5k_BT$ and wavelength $\lambda = 8.192\sigma$. The red dashed line indicates the bulk binodal. Critical points as well as the triple point are illustrated by filled circles. The open squares denote the state points, where the density profiles are calculated and shown in figure 3.7.*

containing the derivatives of the excess free energy density

$$\frac{\beta}{V}\frac{\delta \mathcal{F}_{\mathrm{exc}}}{\delta \rho_i} = T_2^i w_2^i + T_3^i w_3^i. \tag{3.24}$$

Phases at coexistence have to fulfill two conditions. On the one hand, the chemical potentials μ_{c} and μ_{p} of the two phases have to be similar and on the other hand, the pressure p has to match between the two phases. In other words, the coexistence line can be obtained by a common tangent construction. As previously shown [51], additional to the mixed phase, where both species have homogeneous densities, the AO model contains a fluid-fluid demixing phase, where dense colloidal regions and dilute colloidal regions occur in coexistence.

In figure 3.4, the resulting demixing phase diagram for $q = 0.6$ is plotted in two different representations. On the left (3.4(a)), the already mentioned ($\eta_{\mathrm{c}}, \eta_{\mathrm{p}}^{\mathrm{r}}$) representation is chosen. The right plot (3.4(a)) contains the coexisting packing fractions of the colloids η_{c} and the polymers η_{p}. Indeed, the so-called *binodal* line in the phase diagram, shown as a thick curve, indicates the densities of the two phases in coexistence. Following the thin

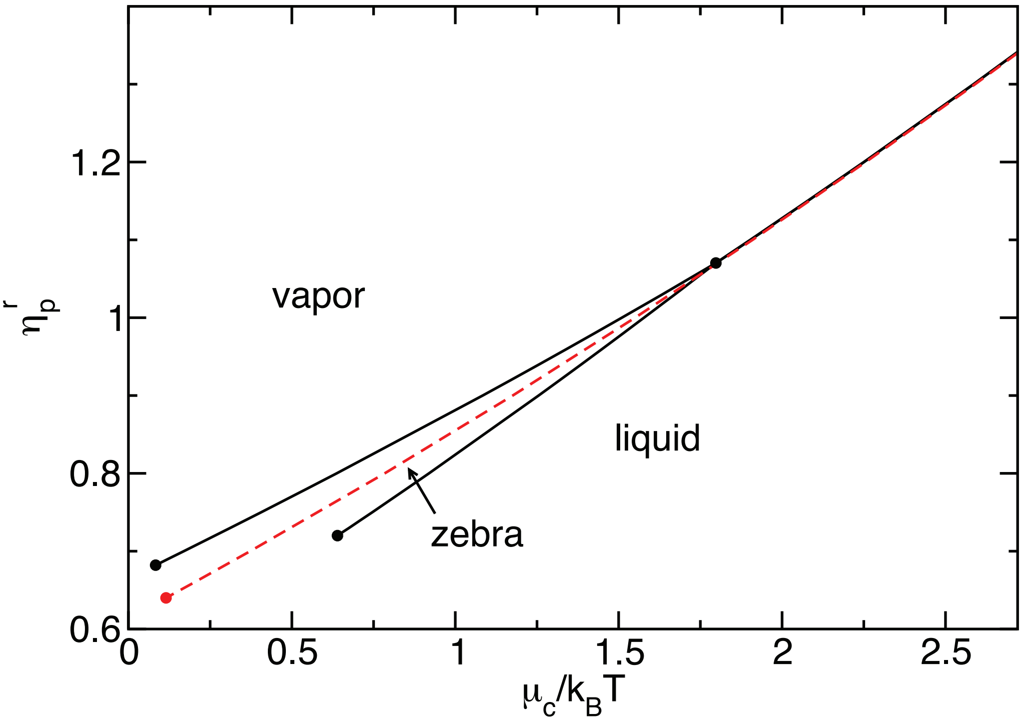

Figure 3.6: *Phase diagram of the AO model in* (μ_c, η_p^r) *representation similar to figure 3.5 but with* $q = 1.0$ *and the external potential characterized by the amplitude* $V_0 = 0.4k_BT$ *and the wavelength* $\lambda = 10\sigma$.

lines, the coexisting packing fractions are visualized by their intersection points with the binodal. Accordingly, figure 3.4(a) shows the packing fractions of the two coexisting colloidal phases and figure 3.4(b) contains the pairs of packing fractions of the two species at coexistence. The black dots denote the critical points of the binodal.

However, the addition of an external potential modifies the phase-diagram dramatically. First, the results from [14] are revisited and therefore, a size ratio $q = 0.6$ and an external potential with amplitude $V_0 = 0.5k_BT$ and wavelength $\lambda = 8.192\sigma$ is chosen.

In figure 3.5 the resulting phase diagram is presented. Here, the bulk binodal is shown as a dashed red line separating the lower packed vapor and the higher packed liquid phase regions. In the presence of the external potential, this binodal splits up and an additional phase, namely the zebra phase, occurs in between. Additionally, the single critical point becomes a critical point for each of the binodal lines. Thus, the phase diagram forms the *inverted letter Y* or *pitchfork* topology. The critical point of the bulk phase is located at lower values of η_p^r, which results from the confinement due to the external potential. This confinement indeed lowers the temperature or in other words increases the polymer reservoir packing fraction. In contrast to previous results (see [14]), the two branches of the fork are of different length, so that the liquid-zebra critical point at $\eta_{p,cr}^{r,zl} \approx 0.526$ exceeds that of the vapor-zebra one at $\eta_{p,cr}^{r,vz} \approx 0.540$. Additionally, this can be seen from

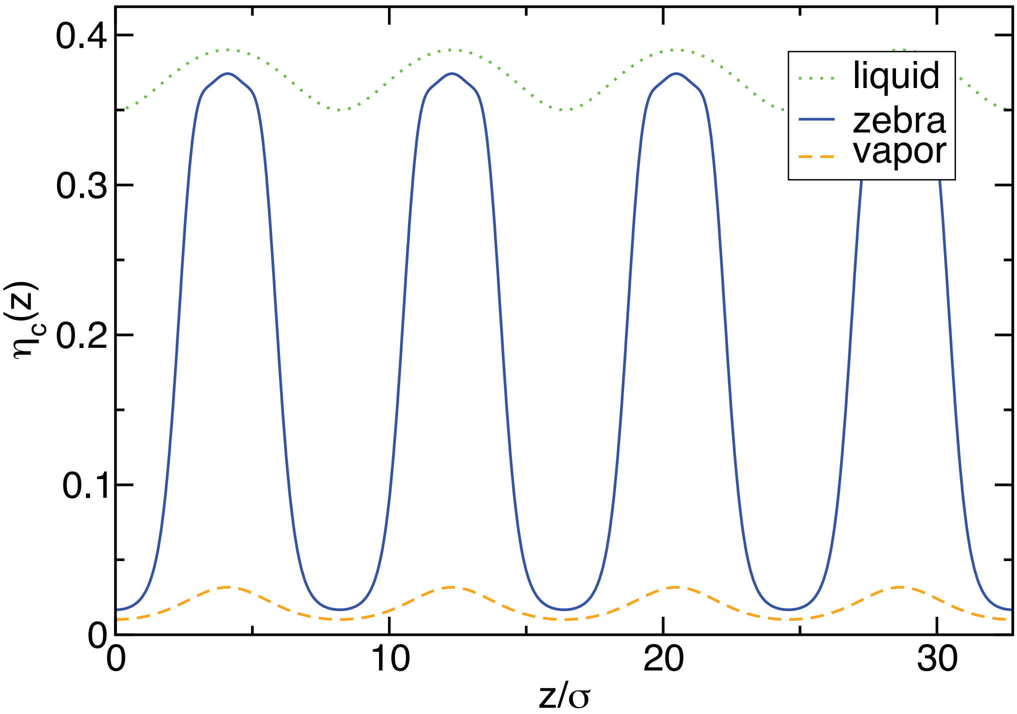

Figure 3.7: *Selected density profiles representing the three different phases calculated at fixed* $\eta_{\rm p}^{\rm r} = 0.8$ *illustrating the vapor (*$\mu_{\rm c}/k_BT = 6.72$*), zebra (*$\mu_{\rm c}/k_BT = 7.12$*), and liquid phase (*$\mu_{\rm c}/k_BT = 7.52$*), as indicated in figure 3.5. The system parameters correspond to the phase diagram shown in figure 3.5, namely* $q = 0.6$*, amplitude* $V_0 = 0.5k_BT$ *and wavelength* $\lambda = 8.192\sigma$*.*

the simulation results that will be presented later. Consequently, the two transition lines approach each other with increasing the polymer reservoir packing fraction $\eta_{\rm p}^{\rm r}$, until they merge at the triple point at $\eta_{\rm p,tr}^{\rm r} \approx 0.755$.

In order to have a system which can be compared with simulations, where problems occur by calculating much more polymers than colloids, as it is required for the previous size ratio of $q = 0.6$, a second set of parameters is chosen with $q = 1$, $\lambda = 10\sigma$, and $V_0 = 0.4k_BT$. The resulting phase diagram can be seen in figure 3.6. Here, the results are similar to those presented in figure 3.5 but the region of the zebra phase is broadened and the whole system has shifted to significantly lower values of the chemical potential $\mu_{\rm c}$.

Knowing the phase diagram, the structure of the different phases shall be examined. As already pointed out, the key difference to the bulk AO model lies in the presence of an additional phase, called the zebra phase. This occurs for polymer reservoir packing fractions $\eta_{\rm p}^{\rm r}$ between the triple and the critical points and appropriate colloid chemical potentials $\mu_{\rm c}$. In order to characterize the different phases, density profiles $\rho(z)$ or, more strictly speaking, profiles of the local packing fraction $\eta(z)$ are computed, as the latter can be better compared with simulation results. Accordingly, three equilibrium profiles, indicated by colored squares in figure 3.5, are presented in figure 3.7.

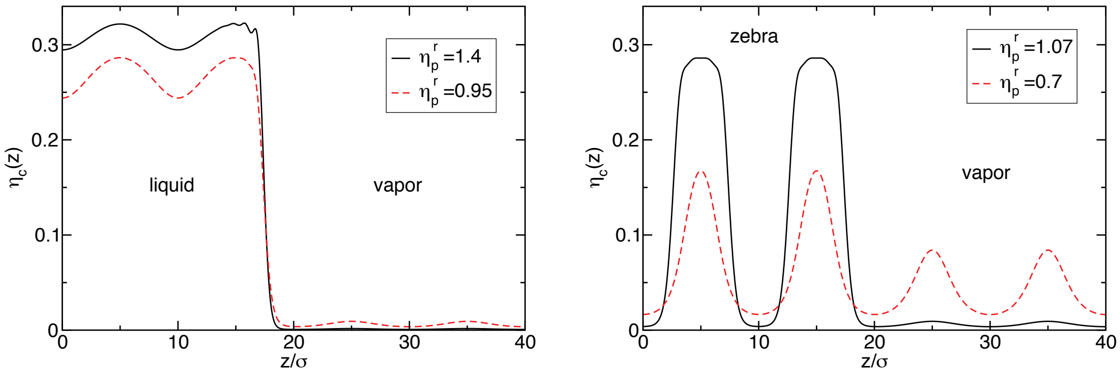

(a) regions of different interactions

(b) different values of q

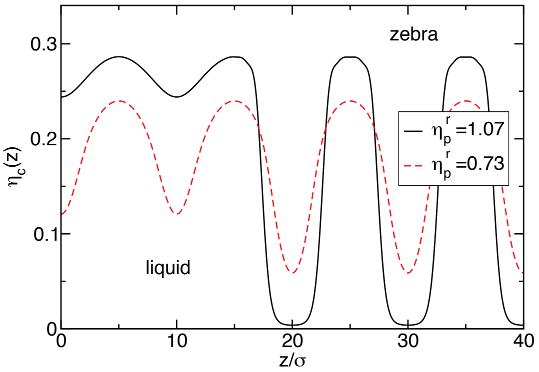

(c) different values of q

Figure 3.8: *Equilibrium density profiles $\eta_\mathrm{c}(z)$ containing the three different interfaces for the AO model with $q = 1$ in the presence of an external field with amplitude $V_0 = 0.4k_BT$ and wavelength $\lambda = 10\sigma$, where (a) illustrates the vapor-liquid, (b) the vapor-zebra, and (c) the zebra-liquid interface.*

At fixed $\eta_\mathrm{p}^\mathrm{r} = 0.8$ the colloid chemical potential is increased so that, a vapor phase ($\mu_\mathrm{c}/k_BT = 6.72$), a zebra phase ($\mu_\mathrm{c}/k_BT = 7.12$), and a fluid phase ($\mu_\mathrm{c}/k_BT = 7.52$) are obtained. Due to the non-constant external potential, all phases have a modulation with the same wavelength λ. However, the average densities are different, where the vapor has a low value, and the liquid has a high value with a slightly different amplitude. On the other hand, the zebra phase displays a much higher amplitude of the modulation, oscillating between the vapor and the fluid average density.

3.2.2 Interfaces and interfacial free energies

After having computed single phases, now interfaces between two coexisting phases and the corresponding surface tensions are studied. Above the triple point $\eta_\mathrm{p}^\mathrm{r} > \eta_\mathrm{p,tr}^\mathrm{r}$, there can be coexistence of a vapor and a liquid phase resulting in a vapor-liquid surface tension γ_vl. In order to calculate this surface tension, first the density profiles of the pure

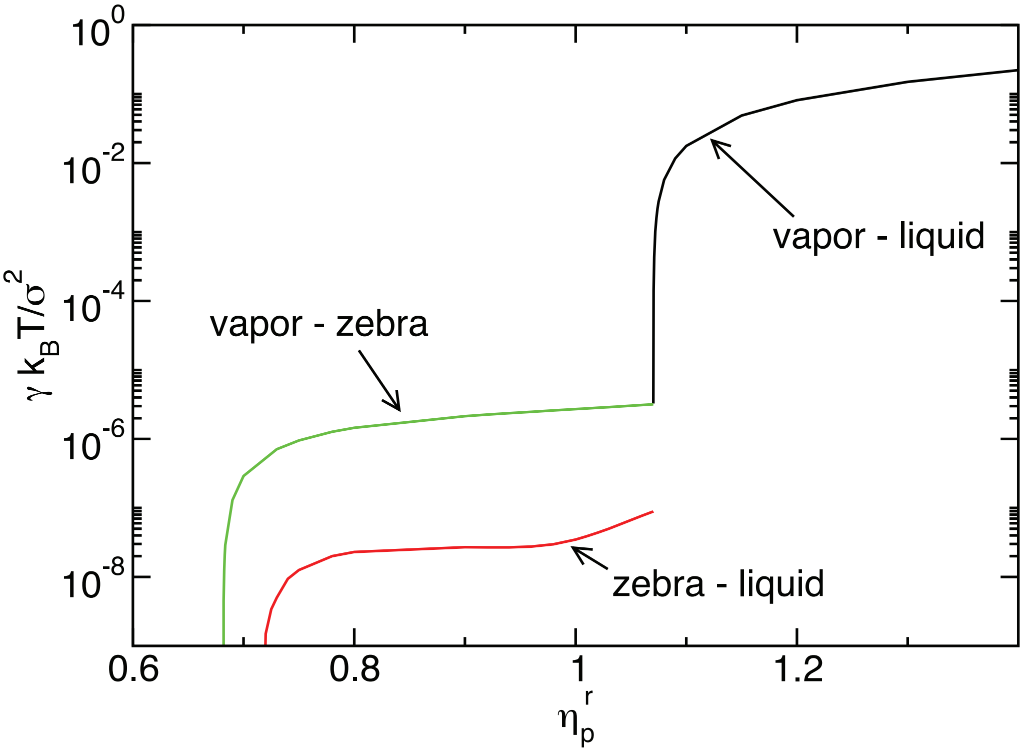

Figure 3.9: *Surface tensions of the vapor-liquid (γ_{vl}), vapor-zebra (γ_{vz}), and zebra-liquid (γ_{zl}) interface depending on the polymer reservoir packing fractions η_p^r plotted on a logarithmic scale. All values were obtained for an AO model with $q = 1$ in an external potential with $V_0 = 0.4 k_B T$ and $\lambda = 10\sigma$.*

coexisting phases, vapor and liquid, have to be computed, leading to the grand canonical free energies $\Omega_{\mathrm{v,pure}}$ and $\Omega_{\mathrm{l,pure}}$. Obviously, at coexistence these are equal, so that $\Omega_{\mathrm{v,pure}} = \Omega_{\mathrm{l,pure}} =: \Omega_{\mathrm{pure}}$. The density profiles which are obtained resemble the corresponding ones in figure 3.7. Then, a system that is including a vapor-liquid interface is considered, minimized by using DFT, and again the grand canonical free energy Ω_{vl} is calculated.

Density profiles are plotted in figure 3.8(a) for two different polymer reservoir packing fractions. Here, some oscillations occur at the interface for sufficiently large η_p^r. With the knowledge of the grand canonical free energies, the surface tension can be obtained by calculating the excess free energy per unit area

$$\gamma_{\mathrm{vl}} = \frac{\Omega_{\mathrm{pure}} - \Omega_{\mathrm{vl,pure}}}{2A}, \tag{3.25}$$

with A denoting the area of the interface. As the examined system is preferred to be periodic for DFT calculations, two interfaces are present, so that a factor of $1/2$ has to be included in the previous formula. In analogy the vapor-zebra and the zebra-liquid interfaces are examined, when the polymer reservoir packing fraction is below the triple point and above the critical points. Hence, some exemplary density profiles are plotted in figures 3.8(b) and 3.8(c) respectively. Strikingly, the interfaces are very sharp, or in other words, the modification of the density profiles close to the interface compared with those of the pure phases is very little. Remembering the definition of the interfacial tension (see equation (3.25)) it can be deduced, that the resulting surface tensions γ_{vz} and γ_{zl} must be very small.

In order to summarize the results obtained from DFT, the three different surface tensions are calculated for various $\eta_{\mathrm{p}}^{\mathrm{r}}$ and the results are presented in figure 3.9 on a logarithmic scale.

For $\eta_{\mathrm{p}}^{\mathrm{r}}$ above the triple point $\eta_{\mathrm{p,tr}}^{\mathrm{r}}$ the vapor-liquid surface tension has finite values but it vanishes at the triple point. By further decreasing the polymer reservoir packing fraction, both, the vapor-zebra γ_{vz} and the zebra-liquid surface tension γ_{zl} remain finite until $\eta_{\mathrm{p}}^{\mathrm{r}}$ reaches one of the critical points. Thus, the first vanishes at $\eta_{\mathrm{p}}^{\mathrm{r}} = \eta_{\mathrm{p,cr}}^{\mathrm{r,vz}}$ and the latter at $\eta_{\mathrm{p}}^{\mathrm{r}} = \eta_{\mathrm{p,cr}}^{\mathrm{r,zl}}$. Both phases coexisting with the zebra phase create a very low surface tension, so that all the time $\gamma_{\mathrm{vl}} \geq \gamma_{\mathrm{vz}} + \gamma_{\mathrm{zl}}$ is fulfilled. More precisely, this means that there is no complete wetting of the zebra phase for polymer reservoir packing fractions higher than the triple point.

3.2.3 Critical behavior

As a further step of understanding the AO model in presence of a spatially oscillating external potential, the critical behavior of the density profiles close to the two critical points is examined. As mentioned previously, DFT is a mean-field theory which shall recover the mean-field critical exponents. Nevertheless, it has been refuted [77] that the universality class of the AO model is the mean-field one. A vapor-zebra order parameter can be considered, given by

$$\Delta_{\mathrm{vz}} = \frac{1}{\lambda} \int_{0}^{\lambda} \mathrm{d}z (\eta_{\mathrm{c,z}}(z) - \eta_{\mathrm{c,v}}(z)), \tag{3.26}$$

which contains the equilibrium colloid density profiles of the zebra phase $\eta_{\mathrm{c,z}}(z)$ or the vapor phase $\eta_{\mathrm{c,v}}(z)$, respectively. In other words, this definition denotes the difference of the *average* colloid densities of the vapor and the zebra phase, as the integration is performed over one period of the external potential. The zebra-liquid order parameter is defined analogously by

$$\Delta_{\mathrm{zl}} = \frac{1}{\lambda} \int_{0}^{\lambda} \mathrm{d}z (\eta_{\mathrm{c,l}}(z) - \eta_{\mathrm{c,z}}(z)), \tag{3.27}$$

containing the equilibrium colloid density profile of the liquid phase $\eta_{\mathrm{c,l}}(z)$.

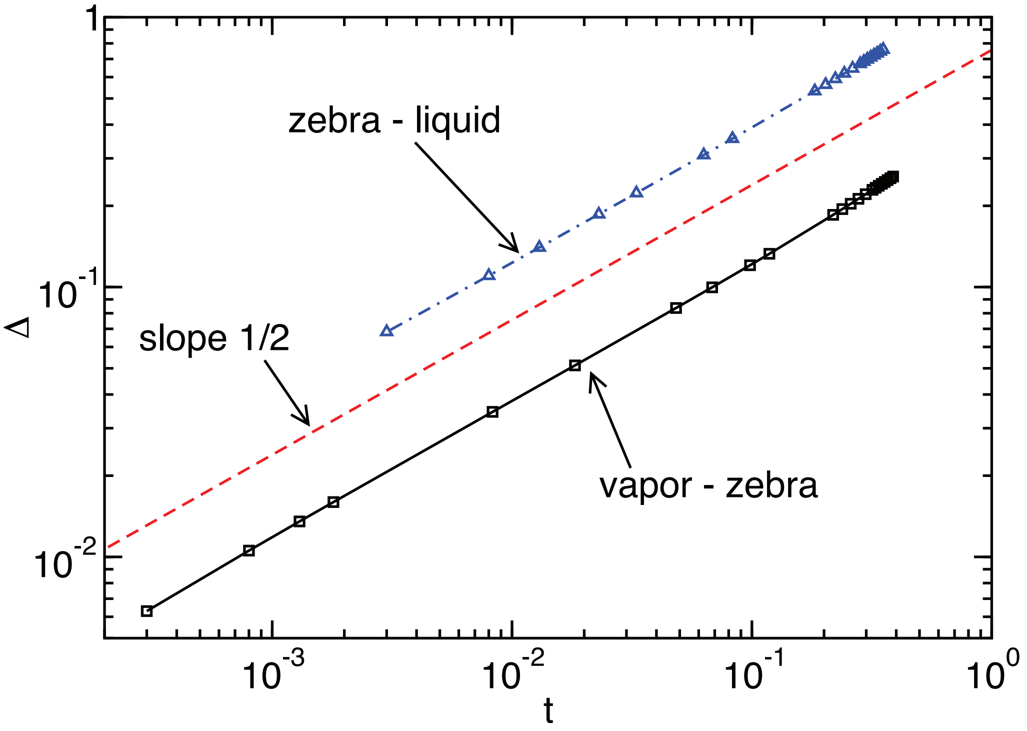

Figure 3.10: *Order parameters Δ_{vz} and Δ_{zl} depending on the distances t from their critical points ($\eta_{\mathrm{p,cr}}^{\mathrm{r,vz}} \approx 0.6817$ and $\eta_{\mathrm{p,cr}}^{\mathrm{r,zl}} \approx 0.717$). In this double logarithmic scale, the red dashed line with slope $1/2$ displays the critical exponent β.*

In a mean-field theory the order parameter is expected to decay with a power law with exponent $\beta = 1/2$ approaching the critical point,

$$\Delta_{\mathrm{x}} \propto t^{\beta}, \tag{3.28}$$

where t is defined as

$$t = \eta_{\mathrm{p}}^{\mathrm{r}} - \eta_{\mathrm{p,cr}}^{\mathrm{r,x}} > 0, \tag{3.29}$$

and x stands for vz and zl, respectively. For the further calculations, the critical points are set to $\eta_{\mathrm{p,cr}}^{\mathrm{r,vz}} \approx 0.6817$ and $\eta_{\mathrm{p,cr}}^{\mathrm{r,zl}} \approx 0.717$. Accordingly, the order parameters are computed as functions of $\eta_{\mathrm{p}}^{\mathrm{r}}$ and visualized in figure 3.10. Using a double logarithmic scale, the advantage is that a constant slope of a curve corresponds to the similar constant critical exponent. A line of slope $\beta = 1/2$ is included in dashed red. After having shifted the zebra-liquid line up by half a decade it becomes clear that both order parameters yield the expected mean-field critical exponents.

Now, the critical behavior of the vapor-zebra and zebra-liquid surface tensions

$$\gamma_{\mathrm{x}} \propto t^{\mu} \tag{3.30}$$

is examined in a similar way, with $\mathrm{x} \in (\mathrm{vz}, \mathrm{zl})$. t is defined in analogy to equation (3.29)

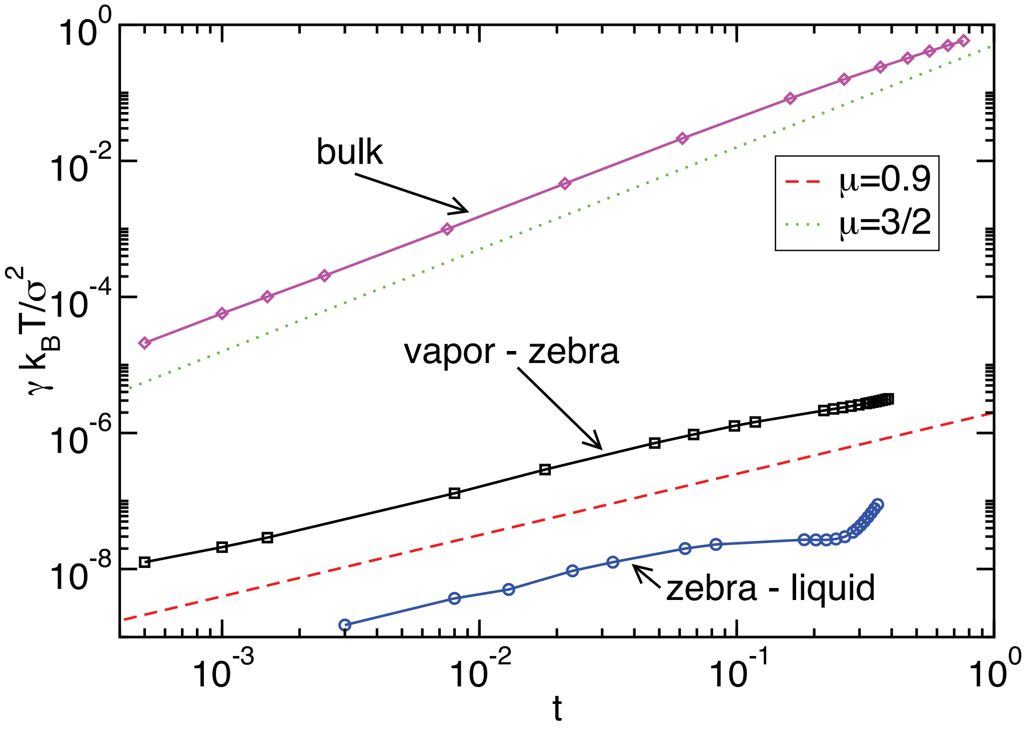

Figure 3.11: *Surface tensions* $\gamma_{\rm vz}$, $\gamma_{\rm zl}$, *and the bulk vapor-liquid surface tension* $\gamma_{\rm vl}$ *as functions of* t *similar to figure 3.10. In this double logarithmic scale, the red dashed line indicates the slope* 0.9 *and the dotted green line shows the mean-field slope* $3/2$.

so that the critical exponent in a mean-field theory is expected to be $\mu = 3/2$.

Using the results from figure 3.9 but as a function of the distance t from each critical point, the critical behavior can be plotted with a double logarithmic scale again (see figure 3.11). In addition, the results for the bulk liquid-vapor interface are computed, where no external potential is present. The latter recovers the expected mean field critical exponent but surprisingly, both other curves show a different critical behavior with exponent $\mu \approx 0.9$. The only reason for this can be that $\gamma_{\rm vz}$ and $\gamma_{\rm zl}$ do not become critical. There must be a "hidden" surface tension $\gamma_{\rm h}$ which fulfills the mean-field critical behavior. The next step is now to perform computer simulations in order to find this “hidden” surface tension and to examine the critical behavior from a second point of view.

3.3 Comparison with Monte Carlo simulations

In this section, grand canonical Monte Carlo simulations [100] performed by Richard L. C. Vink are presented. As already mentioned, the fixed state variables in the grand canonical ensemble are the temperature T, the volume V, the colloid chemical potential $\mu_{\rm c}$, and the polymer reservoir packing fraction $\eta_{\rm p}^{\rm r}$, but the number of colloids $N_{\rm c}$ and polymers $N_{\rm p}$ in the system can vary. An efficient simulation technique, namely a grand canonical cluster move [77], is used in combination with a biased sampling scheme [101]. Therefore the volume of the simulation box is $V = L_x \times L_y \times L_z$ with periodic boundaries and the imposed laser field (see equation (3.5)) propagates along the z-direction. Due to this, the length parallel to the laser field needs to fulfill $L_z = n\lambda$, with integer $n \in \mathbb{N}$, and λ the wavelength of the external potential. The examined system has the same parameters as used in the DFT calculations before, so to say a size ratio of $q = 1$, a wavelength $\lambda = 10\sigma$, and an amplitude $V_0 = 0.4k_BT$. Resulting from the simulations, the *order parameter distribution* $P(\eta_\mathrm{c})$ (OPD) defined as the probability to observe the system in a state with colloid packing fraction η_c can be obtained. The average colloid packing fraction

$$\langle\eta_\mathrm{c}\rangle = \int \mathrm{d}\eta_\mathrm{c} P(\eta_\mathrm{c})\eta_\mathrm{c}, \tag{3.31}$$

the colloidal compressibility

$$\chi_\mathrm{c} = V\left(\langle\eta_\mathrm{c}^2\rangle - \langle\eta_\mathrm{c}\rangle^2\right), \tag{3.32}$$

and the Binder cumulant [102]

$$Q := \frac{\langle m^2\rangle^2}{\langle m^4\rangle}, \quad m = \eta_\mathrm{c} - \langle\eta_\mathrm{c}\rangle \tag{3.33}$$

are computed. As common in simulations, these quantities, and the OPD, depend on the system size, the colloid chemical potential μ_c, and the polymer reservoir packing fraction $\eta_\mathrm{p}^\mathrm{r}$, as well as all other model parameters.

3.3.1 Phase diagram

At first, the phase diagram is computed by varying the colloid chemical potential μ_c at fixed polymer reservoir packing fraction $\eta_\mathrm{p}^\mathrm{r}$. In this case, phase transitions become visible as peaks in the colloidal compressibility χ_c. Thus, in figure 3.12(a), χ_c is plotted as a function of μ_c. Here, two peaks are observed, corresponding to two transitions. Where the left peak indicates the vapor-zebra transition, with the value of the chemical potential μ_c denoting the critical value $\mu_\mathrm{c}^\mathrm{vz}$. The right peak shows the zebra-liquid transition at the critical value $\mu_\mathrm{c}^\mathrm{zl}$. For polymer reservoir packing fractions $\eta_\mathrm{p}^\mathrm{r} > \eta_\mathrm{p,tr}^\mathrm{r}$ above the triple point there is only one peak in this representation, which results from the vapor-liquid transition. Consequently, the phase diagram can be obtained from the peak positions for different $\eta_\mathrm{p}^\mathrm{r}$, which are then plotted in figure 3.13(a). Here, the inverted letter Y topology predicted by DFT (see figure 3.6) is recovered.

In this phase diagram, dots are indicating the critical points which can be computed by performing a finite size scaling. That means, that with varying the colloid chemical potential μ_c at fixed polymer reservoir packing fraction $\eta_\mathrm{p}^\mathrm{r}$ and system size, the average colloid packing fraction $\langle\eta_\mathrm{c}\rangle$, the colloidal compressibility χ_c, and the Binder cumulant Q are

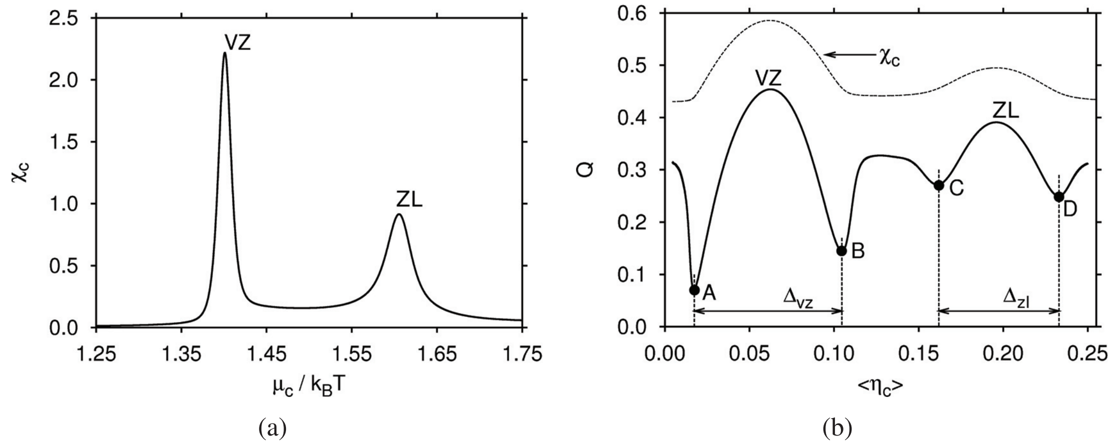

Figure 3.12: *Location of the vapor-zebra (VZ) and zebra-liquid (ZL) transitions in grand canonical simulations with* $\eta_{\mathrm{p}}^{\mathrm{r}} = 1.0$ *and box parameters* $L_x = L_y = 12\sigma$*, and* $L_z = 2\lambda = 20\sigma$*. In (a), the colloidal compressibility* χ_{c} *is plotted as a function of the colloid chemical potential* μ_{c}*, resulting in the critical values* $\mu_{\mathrm{c}}^{\mathrm{vz}}$ *and* $\mu_{\mathrm{c}}^{\mathrm{zl}}$*. In (b), the cumulant* Q *versus* $\langle\eta_{\mathrm{c}}\rangle$ *is shown as a solid line containing labeled minima* A, B, C, D *and order parameter* Δ_{vz} *and* Δ_{zl}*. The dashed line denotes the compressibility* χ_{c} *on an arbitrary scale.*

computed. In figure 3.12(b), typical values of Q and χ_{c} are plotted as functions of $\langle\eta_{\mathrm{c}}\rangle$. In this case, the main point is that the compressibility maxima of the vapor-zebra and zebra-liquid transitions match with the maxima in the cumulant. In addition to the two maxima, four minima can be figured out, where the points

$$A \equiv \left(\langle\eta_{\mathrm{c}}\rangle_{\mathrm{vz}}^{-}, Q_{\mathrm{vz}}^{-}\right), \quad B \equiv \left(\langle\eta_{\mathrm{c}}\rangle_{\mathrm{vz}}^{+}, Q_{\mathrm{vz}}^{+}\right), \tag{3.34}$$

correspond to the vapor-zebra transition, and the points

$$C \equiv \left(\langle\eta_{\mathrm{c}}\rangle_{\mathrm{zl}}^{-}, Q_{\mathrm{zl}}^{-}\right), \quad D \equiv \left(\langle\eta_{\mathrm{c}}\rangle_{\mathrm{zl}}^{+}, Q_{\mathrm{zl}}^{+}\right), \tag{3.35}$$

comply with the zebra-liquid transition. For the thermodynamic limit, it is known [103, 104] that

$$\lim_{L_x, L_y, L_z \to \infty} Q_{\mathrm{vz}} = \begin{cases} 1/3 & , \mathrm{for} \eta_{\mathrm{p}}^{\mathrm{r}} < \eta_{\mathrm{p,cr}}^{\mathrm{r,vz}}, \\ 0 & , \mathrm{for} \eta_{\mathrm{p}}^{\mathrm{r}} > \eta_{\mathrm{p,cr}}^{\mathrm{r,vz}}, \end{cases} \tag{3.36}$$

with $Q_{\mathrm{vz}} \equiv (Q_{\mathrm{vz}}^{-} + Q_{\mathrm{vz}}^{+})/2$, and $\eta_{\mathrm{p,cr}}^{\mathrm{r,vz}}$ the value of $\eta_{\mathrm{p}}^{\mathrm{r}}$ at the vapor-zebra critical point. Following this, the variation of the system size and the calculation of Q_{vz} as a function of $\eta_{\mathrm{p}}^{\mathrm{r}}$ leads to the critical point as all functions intersect at the critical polymer reservoir packing fraction $\eta_{\mathrm{p}}^{\mathrm{r}} = \eta_{\mathrm{p,cr}}^{\mathrm{r,vz}}$. For the zebra-liquid critical point this procedure can be done analogously with $Q_{\mathrm{zl}} \equiv (Q_{\mathrm{zl}}^{-} + Q_{\mathrm{zl}}^{+})/2$.

For this first finite size scaling, the box length along the potential direction $L_z = 2\lambda = 20\sigma$ is kept fixed and the other two lengths are varied simultaneously with $L_x = L_y =: L$.

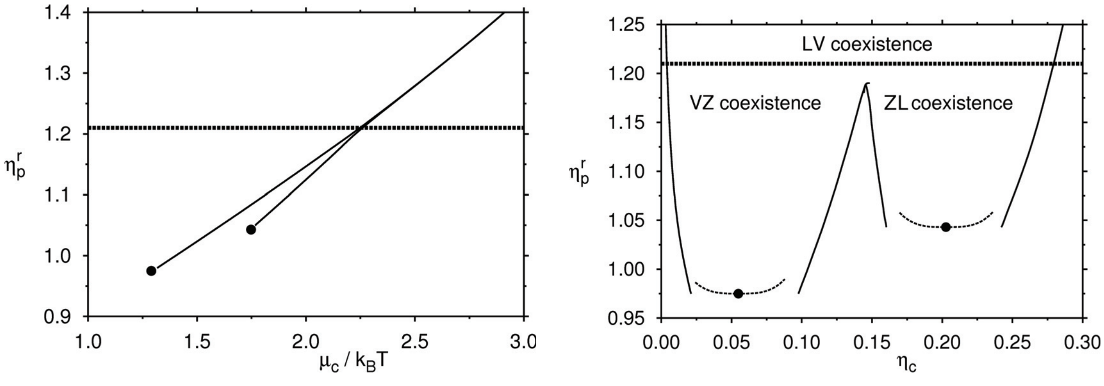

(a) (b)

Figure 3.13: *Phase diagram of the AO model in (a) ($\mu_\mathrm{c}, \eta_\mathrm{p}^\mathrm{r}$) and (b) ($\eta_\mathrm{c}, \eta_\mathrm{p}^\mathrm{r}$) representation with critical points denoted by dots, and the triple point located on the thick dashed line. The thin dashed lines in (b) result from finite size analysis (see figure 3.14).*

Along the z-direction, the system is assumed to be restricted by the external potential so that the correlation length does not diverge. This hypothesis will be constituted in the next section (3.3.2). Due to this ansatz, the critical behavior is effectively two-dimensional. The resulting Q_vz is plotted as a function of $\eta_\mathrm{p}^\mathrm{r}$ for three different box lengths L in figure 3.14(a). Following the definition in equation (3.36), an intersection point can be observed, so that the critical point results at $\eta_\mathrm{p,cr}^\mathrm{r,vz} \approx 0.975$. With the same approach, the zebra-liquid critical point can be calculated at $\eta_\mathrm{p,cr}^\mathrm{r,zl} \approx 1.043$ but which is not illustrated in a figure in this thesis. In analogy with the predictions from DFT, $\eta_\mathrm{p,cr}^\mathrm{r,zl} > \eta_\mathrm{p,cr}^\mathrm{r,vz}$ is obtained. The corresponding value of the colloid chemical potential $\mu_\mathrm{c,cr}^\mathrm{vz}$ in the thermodynamic limit results from an extrapolation of $\mu_\mathrm{c}^\mathrm{vz}$ at $\eta_\mathrm{p}^\mathrm{r} = \eta_\mathrm{p,cr}^\mathrm{r,vz}$ with the assumption $\mu_\mathrm{c,cr}^\mathrm{vz} - \mu_\mathrm{c}^\mathrm{vz} \propto 1/L$. Consequently, the estimated value for the vapor-zebra transition is $\mu_\mathrm{c,cr}^\mathrm{vz} \approx 1.29$, where the zebra-liquid transition yields $\mu_\mathrm{c,cr}^\mathrm{zl} \approx 1.75$.

In the following, the scaling behavior of the order parameter is examined. According to the cumulant minima A and B in figure 3.12(b),

$$\Delta_\mathrm{vz} = \langle \eta_\mathrm{c} \rangle_\mathrm{vz}^+ - \langle \eta_\mathrm{c} \rangle_\mathrm{vz}^- \tag{3.37}$$

is chosen as order parameter for the vapor-zebra transition. Close to the critical point, this results in $\Delta_\mathrm{vz} \propto t^\beta$, containing $t = (\eta_\mathrm{p}^\mathrm{r} - \eta_\mathrm{p,cr}^\mathrm{r,vz})/\eta_\mathrm{p,cr}^\mathrm{r,vz}$ and the critical exponent β. Accordingly, a standard finite size scaling method [105] is performed to compute this order parameter multiplied by $L^{\beta/\nu}$, where ν is the correlation length critical exponent. The results are plotted in figure 3.14(b) as a function of $tL^{\beta/\nu}$, where all curves concur for $\eta_\mathrm{p,cr}^\mathrm{r,vz}$ resulting from figure 3.14(a), $\beta/\nu \approx 0.25 - 0.35$, and $\nu \approx 0.85 - 1.10$. However, the same process can be done for C and D of figure 3.12(b) but this is not the context of this work.

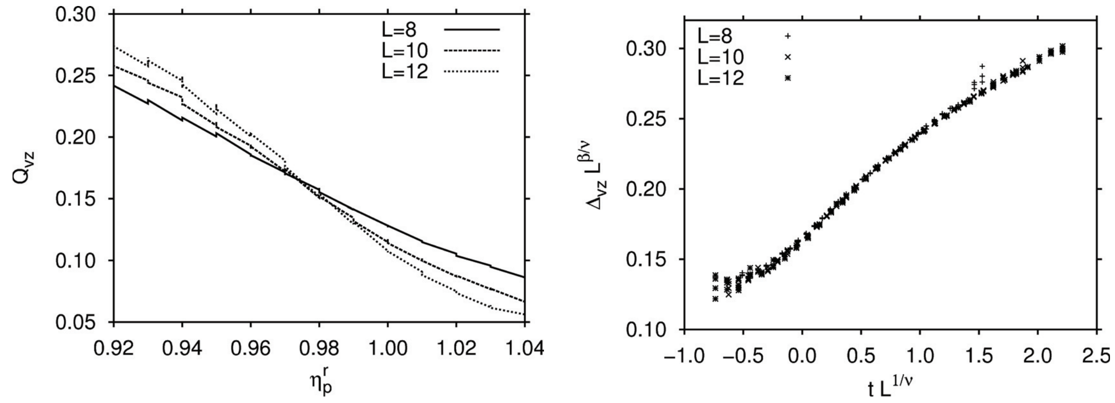

(a) (b)

Figure 3.14: *Finite size scaling analysis of the vapor-zebra critical point where* $L_x = L_y = L$ *is varied, and* $L_z = 2\lambda = 20\sigma$ *is kept fix. For different* L*, (a) illustrates the cumulant* Q_{vz} *depending on* $\eta_{\mathrm{p}}^{\mathrm{r}}$*, where the intersection point provides* $\eta_{\mathrm{p,cr}}^{\mathrm{r,vz}}$*. In (b), the rescaled order parameter* $\Delta_{\mathrm{vz}} L^{\beta/\nu}$ *is plotted as a function of* $tL^{1/\nu}$*, with* ν *and* β *chosen such that the curves collapse.*

With this knowledge, the phase diagram can be computed in the $(\eta_{\mathrm{c}}, \eta_{\mathrm{p}}^{\mathrm{r}})$ representation as done in the bulk DFT calculations (see figure 3.4(a)), and the result is shown in figure 3.13(b). Here, the dots denote the two critical points at $\eta_{\mathrm{c}} \approx 0.055$ and $\eta_{\mathrm{c}} \approx 0.203$, and the dashed line is a binodal resulting from the cumulant minima A, B, C, and D of figure 3.12(b).

3.3.2 Nature of the critical points

In the previous section, it was assumed that the system does not show a critical behavior along the direction of the external field. In order to constitute this hypothesis, the behavior of the colloid-colloid static structure factor

$$S(\mathbf{q}) = \left\langle \frac{1}{n_{\mathrm{c}}} \left| \sum_{j=1}^{n_{\mathrm{c}}} \exp(i\mathbf{q} \cdot \mathbf{r}_j) \right|^2 \right\rangle \tag{3.38}$$

is examined, consisting of a sum over all n_{c} particles with particle positions $\mathbf{r}_j$ inside a small test volume v and $\langle\rangle$ denoting the average. The wave vectors $\mathbf{q}$ are given by

$$\mathbf{q} = 2\pi \left(\frac{l}{L_x}, \frac{m}{L_y}, \frac{n}{L_z} \right), \quad \text{with } l, m, n \in \mathbb{N}, \tag{3.39}$$

where at least one integer has to be non-zero. The vapor-zebra transition is analyzed, but similar results are obtained for the zebra-liquid transition. First, a box consisting of a

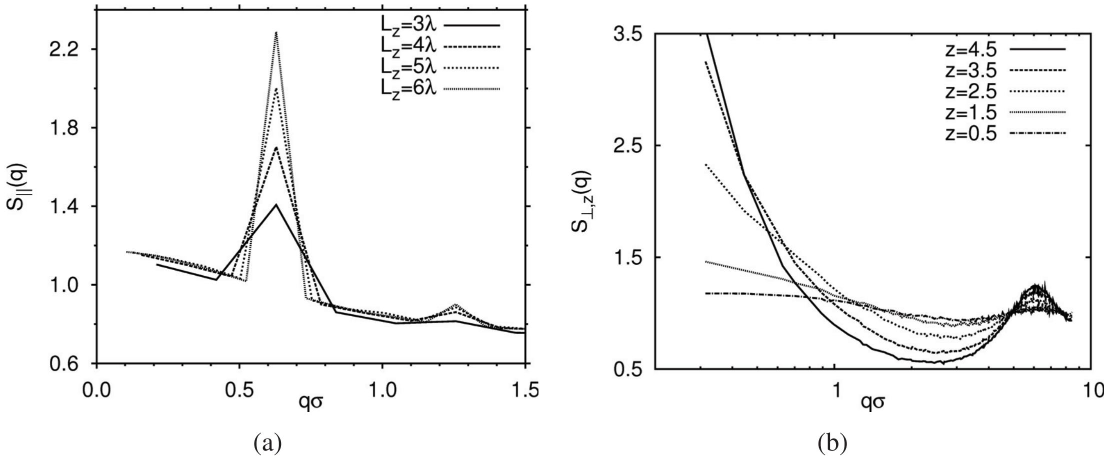

(a) (b)

Figure 3.15: *Colloid-colloid static structure factors $S(q)$ at the vapor-zebra critical point, where (a) illustrates the structure factor $S_{||}(q)$ along the direction of the external potential for different L_z, and fixed $L_x = L_y = 10\sigma$, and (b) illustrates the structure factor $S_{\perp,z}(q)$ perpendicular to the field direction at various z-positions for fixed $L_x = L_y = 20\sigma$, and $L_z = 4\lambda = 40\sigma$.*

periodic cylinder with diameter σ and volume v which is oriented along the field direction is used for the simulation. Thus, the structure factor $S_{||}(q)$ with $q = \sqrt{|\mathbf{q} \cdot \mathbf{q}|}$ can be calculated as a function of selected wave vectors $\mathbf{q}_{||} = 2\pi(0, 0, n/L_z)$. Increasing the length L_z of the cylinder, no divergence of the structure factor for $q \to 0$ is visible in figure 3.15(a), where the peak at $q \approx 0.63$ corresponds to $2\pi/\lambda$ of the external field. In other words, the behavior of the system is not critical parallel to the direction of the external potential.

Next, the structure factor $S_{\perp,z}(q)$ perpendicular to the field direction is analyzed. In this case, the test volume v is a thin cuboid of thickness Δz, with $L_x \times L_y \times \Delta z$, so that the wavevectors are given by $\mathbf{q}_{\perp} = 2\pi(l/L_x, m/L_y, 0)$. Due to the variation of the external potential along z, this structure factor depends on the position, and hence, it needs to be calculated for different values of z. The variation of $S_{\perp,z}$ with z is illustrated in figure 3.15(b), where a divergence at $q \to 0$ only occurs at selected positions. With this knowledge, a finite size scaling can be performed for the latter case, where $L_x = L_y =: L$ is varied. Thus, $S_{\perp,z}(q_{\min})$ is plotted as a function of z in figure 3.16(a). In this case, $q_{\min}$ denotes the value of the smallest accessible wave vector $q_{\min} = 2\pi/L$. The structure factor diverges when L is increased, but only in slabs, which are rich of colloids (see figure 3.16(b) for the colloid density profile). Indeed, the system is critical in these regions that are trapped between non-critical domains, where the external potential, indicated by the dashed line in figure 3.16(b), has its maxima.

The structure factor $S_{\perp,z}(q_{\min})$ diverges at z-positions with large values of the external potential, when the zebra-liquid transition is examined (see figure 3.17). In order to point

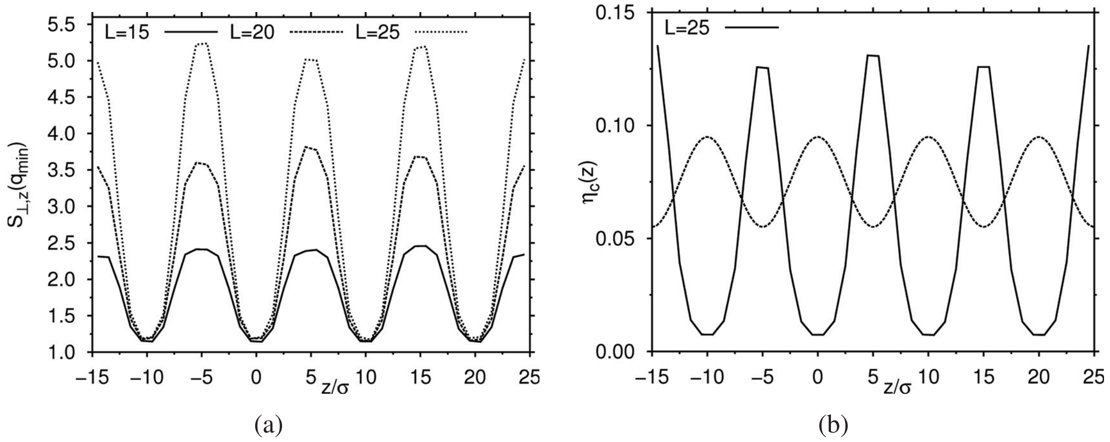

Figure 3.16: *Analysis of the vapor-zebra critical point showing the variation of $S_{\perp,z}(q_{\min})$ with z for several L in (a) and the average colloid packing fraction $\eta_c(z)$ along the z-direction as a solid line in (b), where the external potential is plotted as a dashed line in arbitrary units.*

out the critical exponent, the colloidal compressibility χ_c can be used as $S_{\perp,z}(q_{\min}) \propto \chi_c$ [106]. Thus, the structure factor in the slabs is expected [105] to fulfill

$$S_{\perp,z}(q_{\min}) \propto L^{\gamma/\nu}, \tag{3.40}$$

with the compressibility critical exponent γ. Accordingly, the peak values of figure 3.16(a) are fitted to this scaling law, resulting in $\gamma/\nu \approx 1.3-1.4$. With a similar ratio for the zebra-liquid transition, the structure factor can be normalized as shown in figure 3.17(a), where all curves coincide.

3.3.3 The coexistence regions

Next, the regions of the vapor-zebra and the zebra-liquid coexistence are regarded (cf. figure 3.13(b)). Therefore, the polymer reservoir packing fraction η_p^r needs to be lower than the triple point but higher than the corresponding critical point. The computed order parameter distributions $P(\eta_c)$ are illustrated in figure 3.18, where the left graph corresponds to the vapor-zebra transition ($\mu_c = \mu_c^{vz}$), and the right graph shows the zebra-liquid transition ($\mu_c = \mu_c^{zl}$) in a finite system. Each of the two plots consists of three peaks, where each peak corresponds to a specific phase. Regarding the vapor-zebra transition first, the leftmost peak (1) denotes the vapor phase which consists of a low colloid and high polymer density. Thus, a snapshot of this phase, as shown in figure 3.18 with label 1, hardly consists of any black colloids but only white polymers. Nevertheless, it includes small density modulations along the z-direction, as predicted by DFT (see figure 3.7), but which are not visible in the snapshot. Increasing the packing fraction η_c, a second peak (2) occurs,

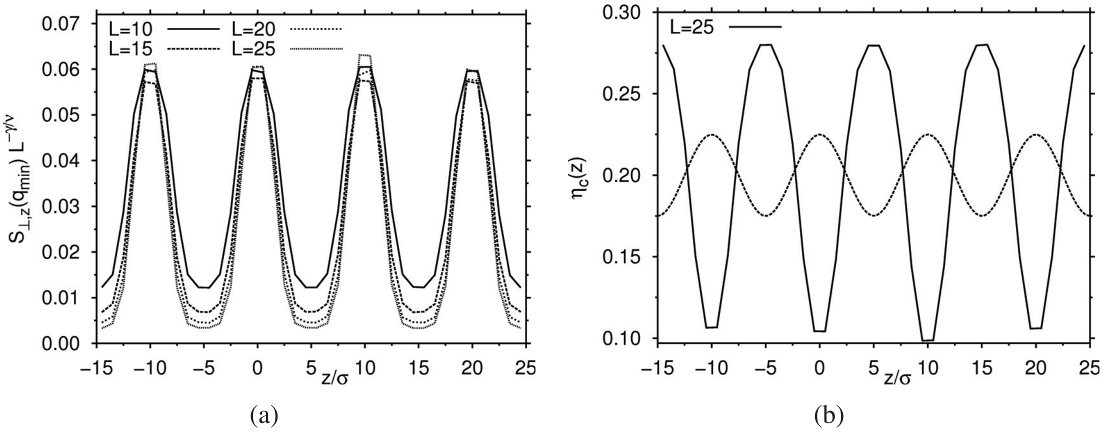

(a) (b)

Figure 3.17: *Same as figure 3.16, but for the zebra-liquid critical point, and with a rescaled representation using* $\gamma/\nu = 1.4$ *in (a).*

which depicts a coexistence state, consisting of a slap of zebra and a slab of vapor phase (snapshot 2). Consequently, there is a vapor-zebra interface inside the box in analogy to figure 3.8(b). Due to the periodic boundary conditions of the simulation box, there must exist an even number of interfaces, at least two. For even higher packing fractions η_c, a third peak is present, corresponding to a pure zebra phase which is illustrated in snapshot 3 with a density profile in analogy to figure 3.7.

Focusing on the zebra-liquid coexistence region, similar results are obtained. Here, peak (3') corresponds to the pure zebra phase at a slightly higher colloid packing fraction than for the vapor-zebra coexistence. Peak (4) occurs for the coexisting zebra and liquid phase, with a slab of zebra between a slab of vapor, or in other words the inverse of snapshot 2, and peak (5) indicates the pure vapor phase.

Not only the peaks can be examined, but also the regions between the peaks in the OPD must be analyzed. Thus, a box with $L_x = 30\sigma$, $L_y = 10\sigma$, and $L_z = 2\lambda = 20\sigma$ is considered at fixed polymer reservoir packing fraction. The results are shown in figure 3.19(a), where the logarithm of the OPD is plotted versus the colloid packing fraction. In this representation again three peaks occur for the vapor-zebra coexistence region. A snapshot of the box is illustrated in figure 3.19(b) at $\eta_c = 0.1$, located between the center and the right peak. As previously explained, vapor-zebra coexistence is visible, but in addition to this, one slab is only partially filled. In other words, there is another vapor-zebra interface perpendicular to the exposed external field, which is the “hidden” interface with area $A = \lambda L_y/2$, previously predicted by DFT.

In order to understand this interface, three configurations $(1, 2, 3)$ illustrated in figure 3.19(a) are examined. Therefore, an intersection perpendicular to the z-axis is regarded. The resulting snapshots of the partially filled slab which are located in the (x, y)-plane are schematically shown in figure 3.19(c). First (snapshot 1), a small droplet of

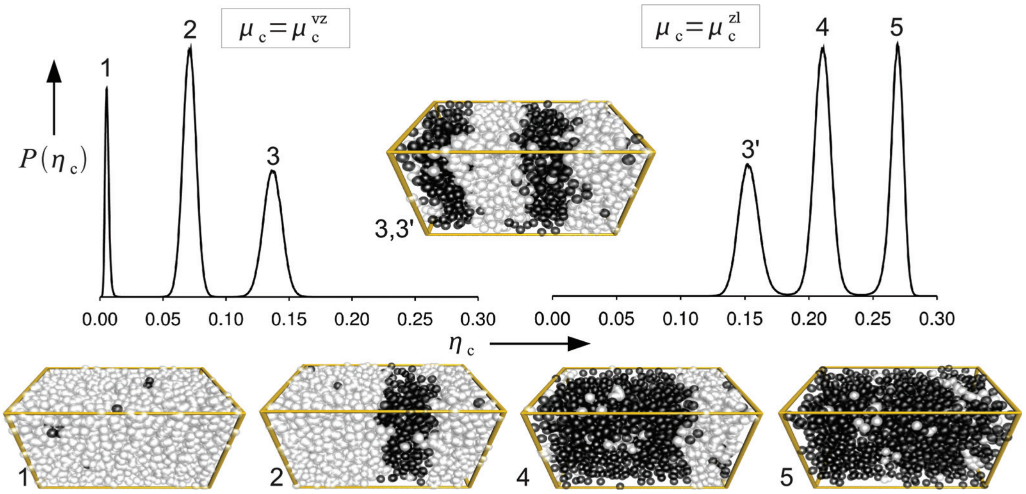

Figure 3.18: *Analysis of the OPD $P(\eta_c)$ for $\eta_p^r = 1.16$ with $L_x = L_y = 12\sigma$, and $L_z = 2\lambda = 20\sigma$. The left plot illustrates $P(\eta_c)$ for the vapor-zebra transition, and the right figure shows that of the zebra-liquid transition. In addition, a snapshot consisting of black colloids and white polymers is included for each peak.*

dense colloidal liquid is formed inside the dilute colloidal vapor phase which has a cylindrical shape aligned along the z-direction. With growing area, the droplet interacts with itself, so that a slab of colloidal liquid is formed, which has two interfaces with the vapor phase (see snapshot 2). At last, with further growing, the first scenario is inverted, resulting in a droplet of vapor inside the colloidal liquid (snapshot 3). Focusing on the second case, the "hidden" interface can be analyzed. As $L_x \gg L_y$, the interface forms perpendicular to the x-direction with no interaction of the two surfaces [107]. Accordingly, the surface tension of the "hidden" interface γ_h can be calculated as the free energy difference ΔF per area of the "hidden" interface A [102]

$$\gamma_h = \Delta F / 2A, \tag{3.41}$$

where the factor $1/2$ results from the presence of two interfaces. Hence, for $\eta_p^r = 1.16$, a typical value of $\gamma_h \approx 0.1 k_B T/\sigma^2$ is obtained. It shall be mentioned that the mechanism shown in figure 3.19(c) is the common droplet condensation for a two dimensional periodic system [108].

With this knowledge, the system can be generalized to periodic boxes with $L \times L \times L_z = n\lambda$, and large L. The results are depicted in figure 3.20, where the two outer peaks correspond to the pure vapor (V) and zebra (Z) phase, similar to the previous results. Between these peaks, the region of coexisting phases is located, where the label $1, 2, \ldots, n-1$ indicates the number of completely filled slabs. Hence, the peaks result from the period of the external potential, so that the "distance" between the peaks correlates with the system size via $d \propto 1/L_z$ in the limit of $L_z \to \infty$. In analogy to figure 3.19, the points $a, a', \ldots$

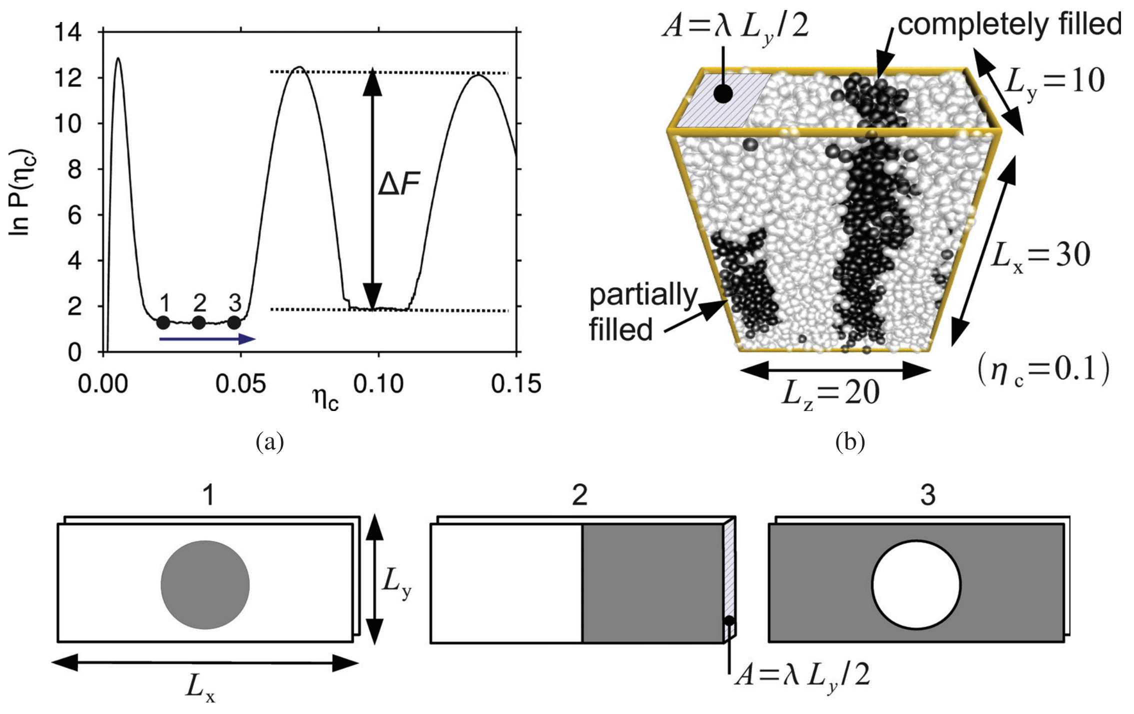

(a)

(b)

(c) different values of q

Figure 3.19: *In (a) the OPD at* $\eta_\mathrm{p}^\mathrm{r} = 1.16$ *for the vapor-zebra transition with* $\ln P(\eta_\mathrm{c})$ *is plotted against* η_c*, containing the energy barrier of the "hidden" interface* ΔF*. (b) illustrates a snapshot at* $\eta_\mathrm{c} = 0.1$*, where the direction of the external field is along* L_z*, including the "hidden" interface of area* A*. Again colloids are black and polymers white spheres. In (c) schematic snapshots are shown, for the path* $1 \rightarrow 2 \rightarrow 3$ *of (a), where the z-direction is perpendicular to the plane of the paper (dark regions correspond to colloid-rich domains).*

correspond to those conditions, where one of the slabs is only partially filled. The energy barriers for the "hidden" interface ΔF and the vapor-zebra interface ΔG and large L are expected [102] to fulfill

$$\Delta F = \gamma_\mathrm{h} \lambda L, \quad \Delta G = 2\gamma_\mathrm{vz} L^2, \tag{3.42}$$

so that in the thermodynamic limit of $L \rightarrow \infty$ the latter is dominating. Thus the resulting OPD is binodal in this case, as expected for a first-order phase transition [109]. However, this analysis can also be performed for the zebra-liquid coexistence region with similar results but slightly different numerical values.

After all, the DFT predictions about the behavior of γ_vz and γ_zl can be verified. As the critical behavior of the system is two-dimensional, or in other words, the diverging part of the interfacial free energy is proportional to L, the criticality only occurs for the "hidden" interface (see equation (3.42)) but not for γ_vz and γ_zl. In finite simulation boxes, ΔG vanishes, so that intermediate peaks occur. The ratio of the outer and inner peak heights comparing figures 3.20 and 3.18 differs which can only happen for very small surface

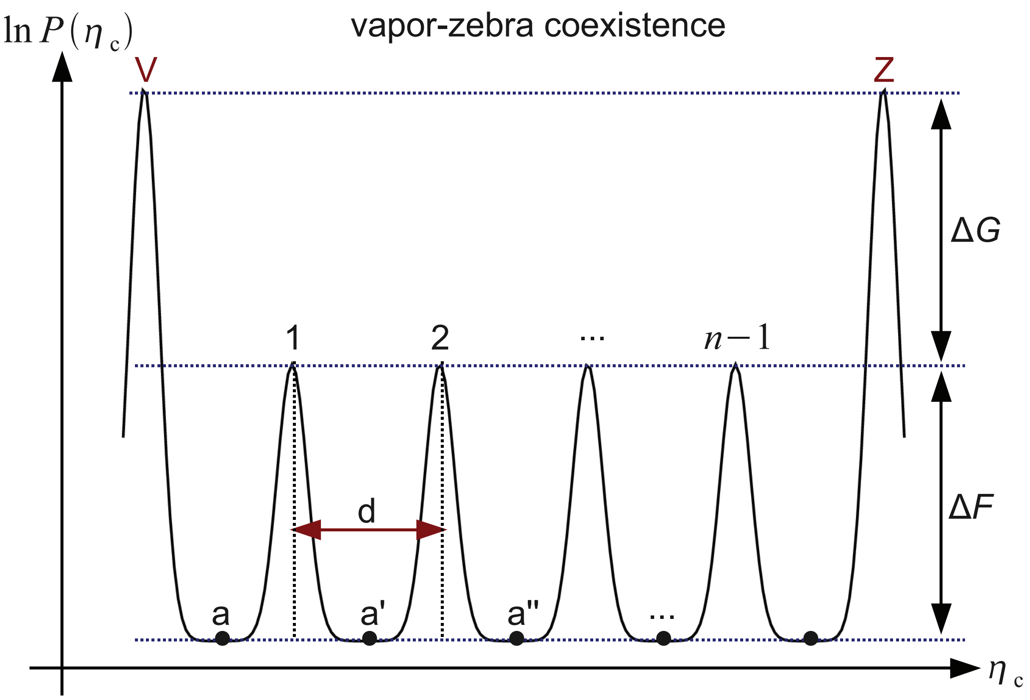

Figure 3.20: *Sketched OPD at the vapor-zebra transition ($\mu_c = \mu_c^{vz}$), in a periodic box with $L \times L \times L_z$, $L_z = n\lambda$, and large L. Shown are the peaks for the pure vapor (V) and zebra (Z) phase and intermediate peaks $1, 2, \dots, n-1$ indicating coexistence phases, where each period of the external potential is filled with one of the two phases. Phases with partially filled slabs are denoted by the minima $a, a', \dots$ (cf. figure 3.19(b)). In addition, free energy barriers of the vapor-zebra (ΔG) and the "hidden" interface (ΔF) are included.*

tensions.

At last, the triple point is examined, where all three occurring phases coexist. Hence, the OPD consists of three peaks in the thermodynamic limit. In figure 3.21, the resulting OPD is plotted for a simulation box with $L_x = L_y = 8\sigma$ and $L_z = 2\lambda = 20\sigma$ at $\eta_p^r = 1.22$, where the three pure phases are labeled with (V, Z, L). The presence of the coexistence peaks again corroborates the very low surface tensions γ_{vz} and γ_{zl} even close to the triple point where they are maximal.

3.4 Conclusions

In conclusion, fluid phase separation inside a one-dimensional periodic external potential has been examined performing density functional theory calculations and Monte Carlo computer simulations. The system was described by the Asakura-Oosawa model for a colloid-polymer mixture, but similar results can be obtained for different systems containing a bulk liquid-vapor critical point. Following the previous work [14], the critical point

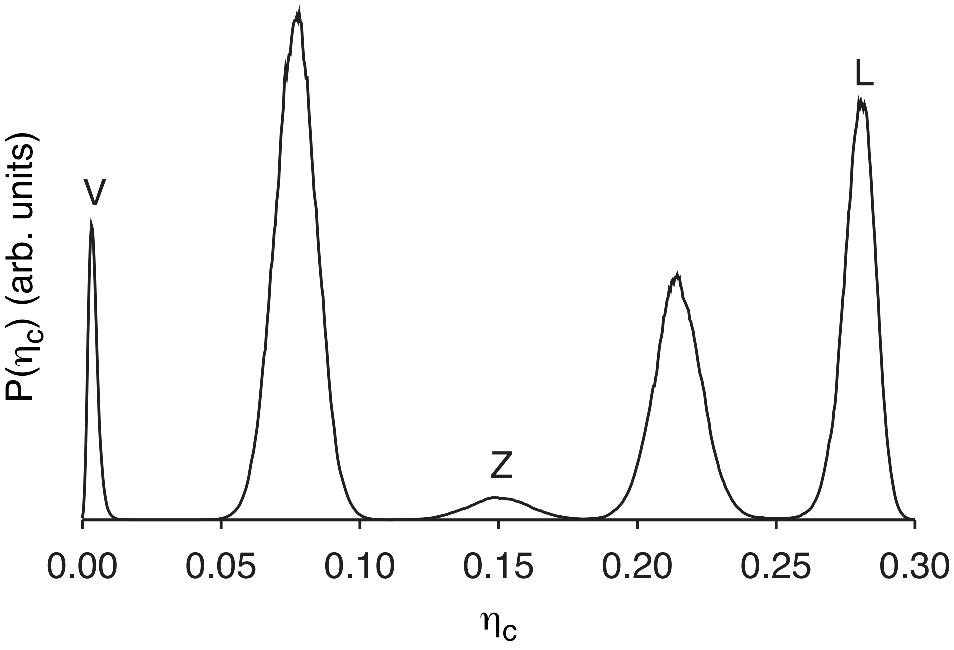

Figure 3.21: *The OPD* $P(\eta_{\mathrm{c}})$ *at* $\eta_{\mathrm{p}}^{\mathrm{r}} = 1.22$ *close to the triple point for a simulation box with* $L_x = L_y = 8\sigma$, $L_z = 2\lambda = 20\sigma$ *consisting of the vapor (V), zebra (Z), and liquid (L) phase and two coexistence phases.*

is split up into two critical points and a triple point, due to the presence of the external field. Thus, the phase diagram consists of three phases, the vapor, zebra, and liquid phase and hence, three different coexistence regions, namely the vapor-zebra, zebra-liquid, and vapor-liquid coexistence, are obtained. All three phases show density modulations along the direction of the imposed field, but those of the zebra phase are significantly larger. As a further development compared with [14], the two critical points are found to be located at different polymer reservoir packing fractions. Furthermore, surface tensions between all coexisting phases were calculated, exposing that the vapor-zebra and the zebra-liquid surface tension are extremely small. In addition, the analysis of the critical behavior disclosed critical exponents different from the expected mean-field ones.

In order to understand the predictions from DFT, computer simulations were performed which confirmed all trends. In the presence of the external field, the system is divided into effectively two dimensional slabs, perpendicular to the field direction. Thus, the critical correlations are finite along the direction of the potential and diverge inside the two-dimensional slabs. Inside each slab, interfaces can occur, which contribute to the free energy barriers. For very large systems, the system will phase separate, but for the vapor-zebra and the zebra-liquid coexistence regions this tendency is very weak. This can be explained by very low surface tensions for the vapor-liquid and the zebra-liquid case, as predicted by DFT, where the latter is of the order $10^{-6}\,k_BT/\sigma^2$. Being too small to detect in simulations, the order nevertheless can be confirmed by this due to the weak tendency of the system to macroscopically phase separate.

In real-space experiments, all results could be verified, using for example confocal microscopy [110] to examine a colloid-polymer mixture, which has already been performed for bulk criticality [111]. Furthermore, the addition of an external field by imposing a standing optical wave has been used [112, 113], but the much weaker tendency of the system to macroscopically phase separate, though it should be easily detectable, was not seen yet.

CHAPTER 4

Soft repulsive particles under gravity

In this chapter the results of publication [2] will be presented, based on simulations and theoretical calculations performed by Tobias Kruppa, computations using (dynamical) density functional theory, and work by René Messina and Harmut Löwen to link those results. Here, a binary mixture of magnetized particles with long-range repulsive interaction is considered in the presence of gravity. In experiments, it is well known that gravity can be used to separate particles of different size or species out of a mixture [114, 115]. Nevertheless, the microscopic explanation of mixing and demixing is discussed controversially [116, 117]. In granulates, shaking or vibrating can induce the *brazil-nut effect*, which means that heavier particles float on top of lighter particles. Although this effect has been known for a long time [118], it is still the subject of recent examinations [117]. However, parameter combinations as well as other details to generate this effect are debated [119–124]. Interestingly, this effect does not correspond to Archimedes' law, in which the buoyancy of a particle is stated to be similar to its weight.

In order to examine the effect of gravity on particles, colloidal mixtures can hold as model systems for static and dynamical observations [125–130]. Aiming for the phase behavior, binary charged mixtures are explored [131–134]. Thus, the *colloidal brazil-nut effect* occurs, at which the sediment of highly deionized charged colloidal mixtures is demixed into layers of different species effected by counterion lifting [135, 136]. Regarding binary mixtures, this separation effect can be explored by using the equations of state [137–139] resulting in a description which matches with Archimedes' law. In addition, this was confirmed in experimental real-space studies on soft repulsive colloidal mixtures in three dimensions [128]. Phase separation can also occur for colloid-polymer mixtures (see the previous chapter 3) under gravity in equilibrium [96, 140].

In addition, nonequilibrium examinations were performed, as inverting the direction of gravity by turning a sample to investigate the settling process of particles [125, 141]. Furthermore, the effect of gravity on crystal growth on a patterned substrate [142, 143], spatially varying temperature fields [144], and zone formation in sedimenting colloidal mixtures [145] were analyzed, but only few studies of gravity fields modified periodically in time (the analogue of granular shaking) were performed [146].

In this chapter, (dynamical) density functional theory as well as Monte Carlo and Brownian dynamics computer simulations are performed to compute the effect of a time-dependent gravity field on a binary mixture of long-range repulsive point particles. Thus, density profiles in equilibrium and time resolved nonequilibrium density profiles are examined where the latter are affected by a periodically inverted gravity field. In the following, the more repulsive particles are denoted as A-particles and the less repulsive ones are the B-particles. Due to this difference, a bubble is formed around each A-particle which in analogy to the colloid-polymer mixture in chapter 3 results in a depletion zone. Thus, the A-particles are lifted in the presence of B-particles, which can be explained by applying Archimedes' law to these bubbles. Additionally, a wall at the bottom of the sample is highly attractive for the A-particles, so that a layering effect can be observed. When the sample is inverted periodically in time, the effect of gravity is inverted analogously and similar stable layers occur in nonequilibrium. It shall be mentioned that the brazil-nut effect does not appear for common hard sphere mixtures [137] as they are treated in chapters 5 and 6. A condition is that the interaction diameter of the spheres has to be much larger than the particle diameter. In this case, as well as in the case discussed in this chapter, the interaction is soft.

The model system used in this chapter is a two-dimensional binary mixture of repulsive colloidal dipoles. An experimental realization of this model are colloidal particles at an air-water-interface in the presence of an external magnetic field which can be examined in real-space microscopy experiments [147–152]. A different set-up are colloidal particles trapped between two horizontally aligned substrates [153, 154]. The long-range repulsion is induced by an external magnetic field. Gravity can result from a tilt of the droplet or the substrates, or from a pressure due to an induced laser field [113]. In three dimensions, the effects are confirmed, so that settling experiments on dipolar or charged colloidal mixtures [128] can be performed, and charged granulates [155] as well as dusty plasmas [156, 157] can be examined.

4.1 System

A binary mixture of colloidal super-paramagnetic point particles indicated as A and B is confined to a two-dimensional planar interface. Each particle species has a different magnetic dipole moment M_A and M_B, where

$$M = M_\mathrm{B}/M_\mathrm{A} \tag{4.1}$$

indicates the dipole-strength ratio. Due to this, the dipolar behavior induced by an external magnetic field H can be written as $M_i = \chi_i H$, where χ_i indicates the magnetic susceptibility, and i labels the two species ($i = \mathrm{A}, \mathrm{B}$). The magnetic field is induced perpendicular to the examined two-dimensional plane. In order to compare the results with experiments, $M = 0.1$ is chosen in analogy to [149, 150, 152]. The relative composition of B-particles indicated by $X = N_\mathrm{B}/(N_\mathrm{A} + N_\mathrm{B})$ is set to 50%, or in other words, both species have the

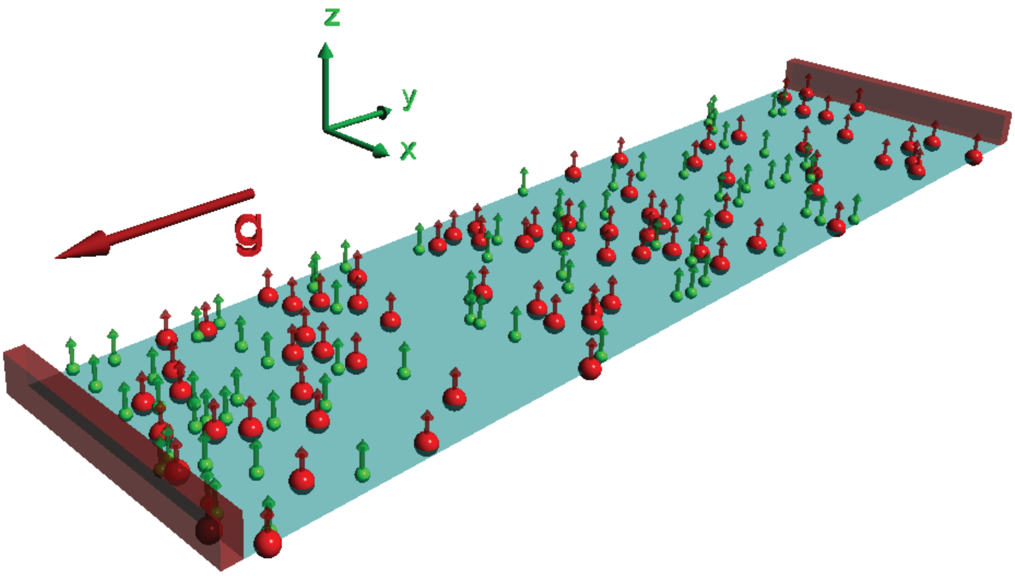

Figure 4.1: *Sketch of the examined system, where red* A*- and green* B*-particles are located on a plain surface with two walls. Small arrows above each particle indicate the direction of the dipole moment. The size of the spheres illustrates the strength of the magnetic dipole moment, but the scale is not exact (*$\frac{R_\mathrm{A}}{R_\mathrm{B}} \neq \frac{M_\mathrm{A}}{M_\mathrm{B}}$*). Gravity denoted by a red arrow is acting in* $-y$*-direction.*

same particle number. The external potential $V_{\mathrm{ext},i}(\mathbf{r})$ which acts on a particle of species i at position $\mathbf{r}$ results from gravity and the effect of the two walls at $y = 0$ and $y = L_y$[1]. Thus, it reads

$$V_{\mathrm{ext},i}(\mathbf{r}) = \begin{cases} m_i g y & , \text{ for } \quad 0 \leq y \leq L_y, \\ \infty & , \text{ otherwise,} \end{cases} \tag{4.2}$$

containing the buoyant mass m_i. Accordingly, gravity acts along the $-y$-direction. The ratio of masses is described by the dimensionless variable

$$m = m_\mathrm{B}/m_\mathrm{A} \; . \tag{4.3}$$

In figure 4.1, a sketch of the system is shown. Here, red larger spheres illustrate the more repulsive A-particles, whereas B-particles are shown as green spheres. Attached to all spheres is an arrow indicating the direction of the dipole moment, which is aligned along the z-direction. In addition, gravity is depicted as a red arrow pointing in $-y$-direction. At $y = 0$ and $y = L_y$, a hard wall is illustrated as a brown barrier. Particle interactions are given by a repulsive pair potential $\phi_{ij}(r)$ of parallel dipoles depending only on the

---

[1] In the static case, the upper wall is not affecting the particles so that the system is similar to a box with infinite height.

distance r of two particles. The interaction potential results in

$$\phi_{ij}(r) = \frac{\mu_0}{4\pi}\frac{M_i M_j}{r^3} = \frac{\mu_0}{4\pi}\frac{\chi_i \chi_j H^2}{r^3}, \tag{4.4}$$

with $i, j = \mathrm{A}, \mathrm{B}$ and μ_0 being the magnetic constant. Following [23], all static quantities at a fixed composition X and susceptibility ratio $\chi_\mathrm{B}/\chi_\mathrm{A}$, depend on the dimensionless interaction strength Γ, with

$$\Gamma = \frac{\mu_0}{4\pi}\frac{\chi_\mathrm{A}^2 H^2}{k_B T l_\mathrm{A}^3}\ , \tag{4.5}$$

also called the coupling constant. Equation (4.5) includes the thermal energy $k_B T$ and the gravitational length of A-particles, which is given by $l_\mathrm{A} = k_B T/(m_\mathrm{A} g)$. This also holds as unit length for all further calculations. In the case of a time dependent analysis, the external potential is similar to that one which is given by equation (4.2) but with a gravity constant $g(t)$ that depends on time, so that

$$V_{\mathrm{ext},i}(\mathbf{r}, t) = \begin{cases} m_i g(t) y & , \text{ for } \quad 0 \le y \le L_y, \\ \infty & , \text{ otherwise.} \end{cases} \tag{4.6}$$

Consequently, the time dependent gravity constant $g(t)$ is given by a stepwise constant function

$$g(t) = \begin{cases} g & , \text{ for } \quad n-1 < t/T_0 \le n - \vartheta, \\ -g & , \text{ for } \quad n - \vartheta < t/T_0 \le n. \end{cases} \tag{4.7}$$

$$\tag{4.8}$$

Here, $n \in \mathbb{N}$ labels the different periods, and T_0 denotes the time of each period of the modulation. $0 \le \vartheta \le 1$ is the swap fraction indicating the ratio of the two cases for the external potential — up and down. In figure 4.2, two different versions of the gravitational potential are plotted as functions of the time parameter t/T_0. Thus, each integer corresponds to one oscillation period T_0. The plotted functions $g(t)$ are normalized with the value g of the static case. The black line shows $g(t)/g$ for the symmetric case, namely $\vartheta = 1/2$, where the time of a positive $g(t)/g$ is similar to the time of a negative $g(t)/g$. In addition, a non-symmetric oscillation is plotted in red ($\vartheta = 1/4$), which is shifted up by a value of $3g$ for clarity. The amplitude of both plots is similar, given by a variation between $+g$ and $-g$ as written in equation (4.7).

Neglecting hydrodynamic interactions, the particle dynamics is set to be Brownian. The Brownian time scale is given by the short-time diffusion constant of the A-particles denoted as D_A. As the diffusion constant is proportional to the inverse of the particle radius, the particle diameters used in experiments [149, 150, 152] set the value of D_B by $D_\mathrm{B}/D_\mathrm{A} = 1.61$. Accordingly, this ratio will be used in the further work of this chapter.

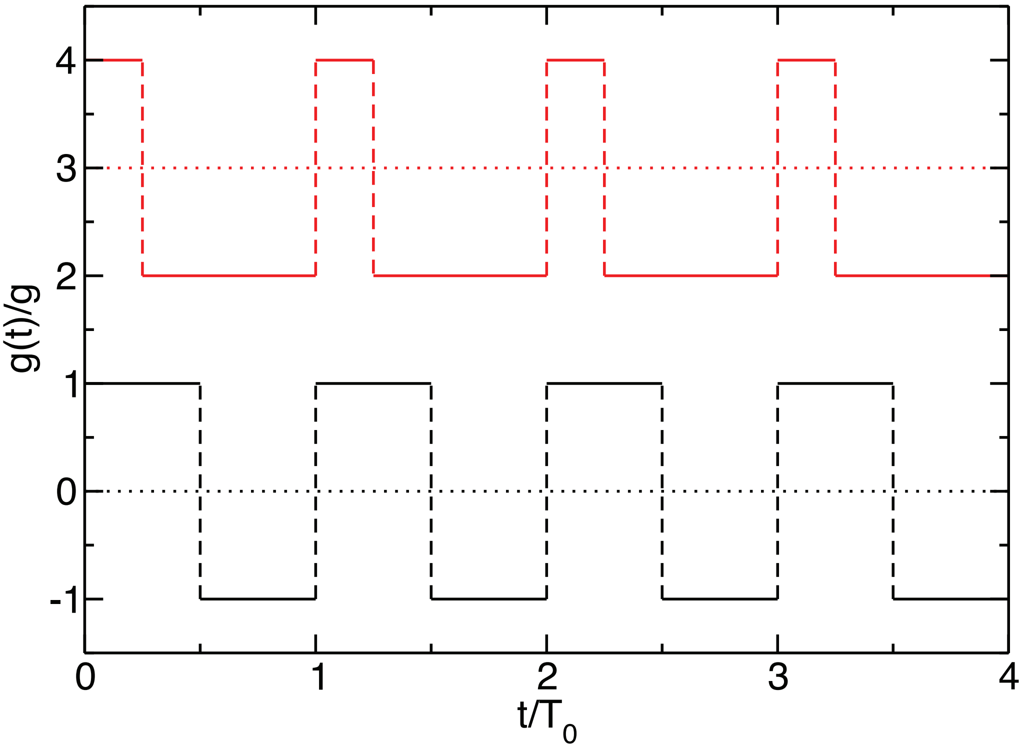

Figure 4.2: *Time dependent plot of the gravitation constant $g(t)$ normalized by the static value g as a function of time t/T_0. The black line indicates the symmetric case of $\vartheta = 1/2$, and the red line shows the case of $\vartheta = 1/4$ which is shifted up by $3g$ in order to clarify the visualization.*

4.2 Density Functional Theory

As described in section 2.2, in density functional theory the grand canonical free energy $\Omega(T, \mu_\mathrm{A}, \mu_\mathrm{B}, [\rho_\mathrm{A}(\mathbf{r}), \rho_\mathrm{B}(\mathbf{r})])$ depending on the temperature T and the chemical potentials $\mu_\mathrm{A}, \mu_\mathrm{B}$ of the two species has to be minimized with respect to the one-particle density distributions $\rho_\mathrm{A}(\mathbf{r})$ and $\rho_\mathrm{B}(\mathbf{r})$. Thus, the functional of a two-component system in two spatial dimensions reads

$$\Omega = \mathcal{F}_\mathrm{id}\left([\rho_\mathrm{A}(\mathbf{r})), \rho_\mathrm{B}(\mathbf{r})]\right) + \mathcal{F}_\mathrm{exc}\left([\rho_\mathrm{A}(\mathbf{r})), \rho_\mathrm{B}(\mathbf{r})]\right) + \sum_{i=\mathrm{A,B}} \int \mathrm{d}\mathbf{r}\rho_i(\mathbf{r})\left[V_{\mathrm{ext},i}(\mathbf{r}) - \mu_i\right], \tag{4.9}$$

containing the free energy of an ideal gas in two dimensions given by

$$\mathcal{F}_\mathrm{id} = k_B T \sum_{i=\mathrm{A,B}} \int \mathrm{d}\mathbf{r}\rho_i(\mathbf{r})\left[\ln(\Lambda_i^2\rho_i(\mathbf{r})) - 1\right]. \tag{4.10}$$

Here, Λ_i denotes the (irrelevant) thermal wavelength of particles of species i $(i = \mathrm{A}, \mathrm{B})$. The third summand includes the static external potential $V_{\mathrm{ext},i}(\mathbf{r})$ given by equation (4.2), which acts on particle species i. For the missing excess free energy part, a density expansion approximation is used (see section 2.3.1), which will be recovered here. Therefore, a simple Onsager functional is applied [158, 159]

$$\mathcal{F}_{\mathrm{exc}} = \frac{k_B T}{2} \sum_{i=\mathrm{A,B}} \int \mathrm{d}\mathbf{r} \int \mathrm{d}\mathbf{r}' f_{ij}(|\boldsymbol{r} - \boldsymbol{r}'|)\rho_i(\boldsymbol{r})\rho_j(\boldsymbol{r}'), \tag{4.11}$$

which consists of the negative of the Mayer function already introduced in section 2.3.1

$$f_{ij}(\mathrm{r}) = 1 - e^{-\beta\phi_{ij}(r)}, \tag{4.12}$$

with the interaction potential $\phi_{ij}(r)$ from equation (4.4) and the inverse temperature $\beta = (k_B T)^{-1}$. In contrast to hard interaction potentials as they are used in chapters 3, 5, and 6, this approximation holds only for low densities. It is a density expansion which reproduces the second virial coefficient of the bulk fluid equation of state only at low densities. As no other approach is present which describes high densities in a better way[2], the theory captures all trends resulting from simulations and experiments. Nevertheless, it is expected to fail to describe the details of molecular layering.

However, the density distributions in this chapter have one relevant spatial coordinate, namely the height or y-coordinate, whereas the density profile can be integrated over the x-direction. Thus, all static one-body densities become $\rho_\mathrm{A}(y)$ and $\rho_\mathrm{B}(y)$. Accordingly, the free energy of the ideal gas reads

$$\mathcal{F}_{\mathrm{id}} = k_B T L_x \sum_{i=\mathrm{A,B}} \int \mathrm{d}y \rho_i(y) \left[\ln(\Lambda_i^2 \rho_i(y)) - 1\right], \tag{4.13}$$

and the last summand in equation (4.9) results in

$$\mathcal{F}_{\mathrm{ext}} = L_x \sum_{i=\mathrm{A,B}} \int \mathrm{d}\mathbf{r} \rho_i(y) \left[V_{\mathrm{ext},i}(y) - \mu_i\right]. \tag{4.14}$$

The performance of the integration for the excess free energy given by equation (4.11) leads to

$$\begin{aligned}\mathcal{F}_{\mathrm{exc}} &= \frac{k_B T L_x}{2} \sum_{i,j=\mathrm{A,B}} \int \mathrm{d}y \int \mathrm{d}y' \int \mathrm{d}x \rho_i(y)\rho_j(y') f_{ij}(\mathbf{r} - \mathbf{r}') \\ &= \frac{k_B T L_x}{2} \sum_{i,j=\mathrm{A,B}} \int \mathrm{d}y \int \mathrm{d}y' \rho_i(y)\rho_j(y') \underbrace{\int \mathrm{d}x f_{ij}(\mathbf{r} - \mathbf{r}')}_{=:I_{ij}(\mathbf{r}-\mathbf{r}')}, \end{aligned} \tag{4.15}$$

---

[2] A Ramakrishnan-Yussouff approximation [31] was used for one-component dipoles in [160], which needs to be generalized to mixtures of more components in order to describe the system of this chapter.

with a new function I_{ij} defined as

$$I_{ij}(r) = \int \mathrm{d}x \left(1 - e^{-\beta\phi_{ij}(r)}\right). \tag{4.16}$$

Consequently, the excess free energy functional defined in equation (4.15) can be rewritten by using this new function so that it becomes

$$\begin{aligned} \mathcal{F}_{\mathrm{exc}} &= \frac{L_x}{2} \sum_{i,j=\mathrm{A,B}} \int \mathrm{d}y \int \mathrm{d}y' \rho_i(y)\rho_j(y') I_{ij}(y-y') \\ &= \frac{L_x}{2} \sum_{i,j=\mathrm{A,B}} \int \mathrm{d}y \rho_i(y) \int \mathrm{d}y' \rho_j(y') I_{ij}(y-y') \\ &= \frac{L_x}{2} \sum_{i,j=\mathrm{A,B}} \int \mathrm{d}y \rho_i(y) (\rho_j * I_{ij})(y), \end{aligned} \tag{4.17}$$

where the convolution $*$ is included in analogy to equation (2.41). In conclusion, the grand canonical free energy functional can be written as

$$\begin{aligned} \frac{\beta\Omega}{L_x} = \sum_{i=\mathrm{A,B}} &\int \mathrm{d}y \rho_i(y) \left[\ln(\Lambda_i^2 \rho_i(y)) - 1 + \beta V_{\mathrm{ext},i}(y) - \beta\mu_i\right] \\ &+ \sum_{i,j=\mathrm{A,B}} \frac{\beta}{2} \int \mathrm{d}y \rho_i(y) (\rho_j * I_{ij})(y). \end{aligned} \tag{4.18}$$

From this starting point, the equilibrium density profiles $\rho_i^{\mathrm{eq}}(y)$ can be calculated via the minimization condition

$$\left.\frac{\delta\Omega[\rho_{\mathrm{A}}(y), \rho_{\mathrm{B}}(y)]}{\delta\rho_i(y)}\right|_{\rho_i(y)=\rho_i^{\mathrm{eq}}(y)} = 0, \tag{4.19}$$

resulting in two equations for the two species which read

$$\begin{aligned} \frac{\beta}{L_x}\frac{\partial\Omega}{\partial\rho_{\mathrm{A}}(y)} &= \ln(\Lambda_{\mathrm{A}}^2\rho_{\mathrm{A}}(y)) + \beta V_{\mathrm{ext,A}}(y) - \beta\mu_{\mathrm{A}} + \beta(\rho_{\mathrm{A}} * I_{\mathrm{AA}})(y) + \beta(\rho_{\mathrm{B}} * I_{\mathrm{AB}})(y), \\ \frac{\beta}{L_x}\frac{\partial\Omega}{\partial\rho_{\mathrm{B}}(y)} &= \ln(\Lambda_{\mathrm{B}}^2\rho_{\mathrm{B}}(y)) + \beta V_{\mathrm{ext,B}}(y) - \beta\mu_{\mathrm{B}} + \beta(\rho_{\mathrm{B}} * I_{\mathrm{BB}})(y) + \beta(\rho_{\mathrm{A}} * I_{\mathrm{BA}})(y). \end{aligned} \tag{4.20}$$

where $I_{\mathrm{AB}} = I_{\mathrm{BA}}$ due to the symmetry of the definition. Solving these equations for the corresponding one-body density leads to

$$\begin{aligned}\rho_{\mathrm{A}}(y) &= \frac{1}{\Lambda_{\mathrm{A}}^2}\exp\{-\beta M_{\mathrm{A}}^2(\rho_{\mathrm{A}} * I_{\mathrm{AA}})(y) - \beta M_{\mathrm{A}} M_{\mathrm{B}}(\rho_{\mathrm{B}} * I_{\mathrm{AB}})(y) - \beta V_{\mathrm{ext,A}} + \beta\mu_{\mathrm{A}}\},\\ \rho_{\mathrm{B}}(y) &= \frac{1}{\Lambda_{\mathrm{B}}^2}\exp\{-\beta M_{\mathrm{B}}^2(\rho_{\mathrm{B}} * I_{\mathrm{BB}})(y) - \beta M_{\mathrm{A}} M_{\mathrm{B}}(\rho_{\mathrm{A}} * I_{\mathrm{AB}})(y) - \beta V_{\mathrm{ext,B}} + \beta\mu_{\mathrm{B}}\}.\end{aligned} \tag{4.21}$$

With this definition, the density distribution can be calculated by using a common Picard iteration scheme [49].

While DFT is usually formulated in the grand canonical ensemble with fixed chemical potentials μ_{A} and μ_{B}, the simulations in this chapter are performed at fixed particle numbers. Thus, the chemical potentials can be identified as Lagrange multipliers in order to fix the total line density in x-direction (perpendicular to the direction of gravity) and match it to the line density which is used in the simulations.

For the case of a time dependent gravity field, dynamical density functional theory is used, which is already introduced in section 2.4. Accordingly, the density distributions are described with the generalized diffusion equation captured again from equation (2.80) to become in the two-component case

$$\frac{\partial \rho_i(y,t)}{\partial t} = \beta D_i \nabla \left(\rho_i(y,t)\nabla \frac{\delta\Omega[\rho_{\mathrm{A}}(y,t), \rho_{\mathrm{B}}(y,t)]}{\delta\rho_i(y,t)}\right), \tag{4.22}$$

with a diffusion constant D_i in analogy to the mobility constant of equation (2.80) for each particle species $i = \mathrm{A}, \mathrm{B}$. It shall be mentioned that the DDFT equation is a density conserving equation, or in other words that a density profile corresponding to those from canonical simulations will result in a time evolution in the canonical ensemble. For this reason, the results from simulations and theory can be compared qualitatively. Similar to the static case, only height dependences (y-direction) are analyzed in this chapter, as the density profiles are integrated over the other coordinate. This approach holds only for systems far away from surface freezing [161], as they are examined in this chapter.

4.3 Simulation parameters

The equilibrium behavior of the system is analyzed by performing Monte Carlo (MC) computer simulations. The dynamical results are obtained by standard Brownian dynamics (BD) simulations [100, 162, 163] in the canonical ensemble (see section 2.1). Thus, the particle numbers N_{A} and N_{B}, as well as the temperature T, and the area A are fixed. All simulations yield a one-particle density distribution for each of the two species. In the static case, MC simulations are performed for $N_{\mathrm{A}} = 600$ A- and $N_{\mathrm{B}} = 600$ B-particles, inside a simulation box of size $L_x \times L_y$ and therefore area $A = (30 \times 120)(l_{\mathrm{A}})^2$. BD simulations for the time resolved case are performed for $N_{\mathrm{A}} = N_{\mathrm{B}} = 300$ particles inside a box of size $A = (15 \times 60)(l_\mathrm{A})^2$. Both simulation methods use a box with periodic boundary conditions in x-direction (perpendicular to the gravitational field), as well as in y-direction, where the latter is ignored due to the hard walls at both ends of the box. In both cases, an aspect ratio $L_x/L_y = 1/4$ is assumed, and the gravitational load is given by $N_\mathrm{A}/L_x = 20/l_\mathrm{A}$. Furthermore, the coupling constant Γ is set to 10. The time evolution in BD simulations is calculated for finite time steps $\delta t = 10^{-4}\tau$, with $\tau = l_\mathrm{A}^2/D_\mathrm{A}$. Density profiles are obtained which will be denoted $\rho_i^\mathrm{eq}(y)$ in the static and $\rho_i(y,t)$ in the dynamical case, with $i = \mathrm{A}, \mathrm{B}$.

4.4 Results in Equilibrium

4.4.1 Colloidal brazil-nut effect

The first approach to understand the behavior of the examined system is to perform MC simulations as well as DFT calculations for various mass ratios $0 \le m \le 1$ and dipolar ratios $0 \le M \le 1$. Throughout this chapter, the A-particles are assumed to be heavier ($m_\mathrm{A} \ge m_\mathrm{B}$) as well as stronger coupled ($M_\mathrm{A} \ge M_\mathrm{B}$) than the B-particles. The opposite case is not dealt with in this work even though it is realizable. In figure 4.3, the equilibrium density profiles $\rho_i^\mathrm{eq}(y)$ for both species are plotted as functions of the height y. Here, a fixed dipole ratio $M = 0.1$ is assumed and two different mass ratios $m = 0.1, 0.5$ are chosen. The key finding is that the density profiles of the two cases differ significantly. For $m = 0.1$ as shown in figure 4.3(a) the lighter B-particles are located above the heavier A-particles. This trend is inverted for $m = 0.5$ as can be seen in figure 4.3(b), where the heavier A-particles are on top of the lighter B-particles. In analogy to granular matter, this effect is called the *(colloidal) brazil-nut effect*.

The red line (A-particles) and green line (B-particles) without circles plotted in figure 4.3 show the equilibrium density profiles $\rho_i^\mathrm{eq}(\boldsymbol{r})$ resulting from DFT. Compared with the simulation results, only the trends are similar but no quantitative agreement is obtained. This is due to the usage of the density expansion approach for the excess free energy functional in DFT. Accordingly, the layering spacings are large, when compared with MC results but the contact density of A-particles at the bottom wall is very similar, as illustrated in the small insets in figure 4.3. However, it shall be mentioned that there are no fitting parameters used when the results are compared.

The next step is to quantify the colloidal brazil-nut effect using the criterion given by [135]. Accordingly, the average heights h_i with $i = \mathrm{A}, \mathrm{B}$ are defined via the first moment of the density field resulting in

$$h_i = \frac{\int\limits_0^\infty \mathrm{d}y\, y \rho_i^\mathrm{eq}(y)}{\int\limits_0^\infty \mathrm{d}y\, \rho_i^\mathrm{eq}(y)}. \tag{4.23}$$

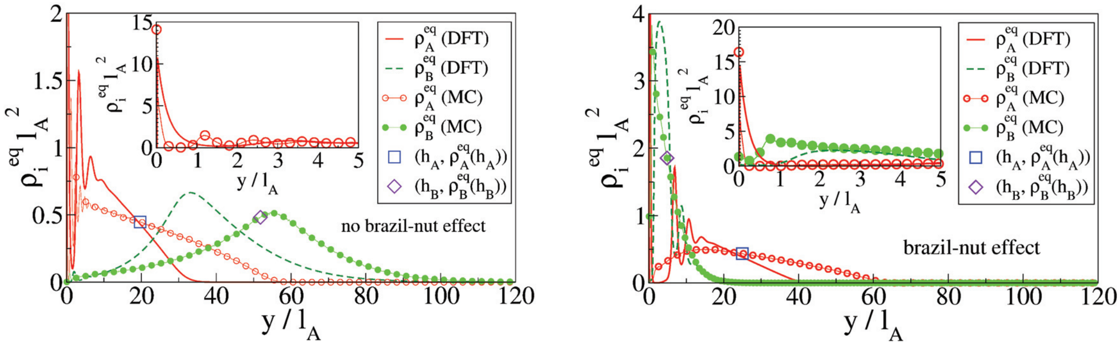

(a) $M = 0.1, m = 0.1$ (no brazil-nut effect)

(b) $M = 0.1, m = 0.5$ (brazil-nut effect)

Figure 4.3: *One-particle density profiles* $\rho_i^{\text{eq}}(\mathbf{r})$, $i = \text{A}, \text{B}$ *resulting from DFT calculations and MC simulation. Mean sedimentation heights* h_i, $i = \text{A}, \text{B}$ *are highlighted for the MC simulation results by a square and a rhomb. The insets magnify the peaks close to the bottom wall.*

These average heights are illustrated in figure 4.3 by a square and a rhomb for the simulation results. Thus, the definition for the colloidal brazil-nut effect reads

$$h_{\text{B}} < h_{\text{A}}, \tag{4.24}$$

or in other words the heavier A-particles are, on average, located above the lighter B-particles.

The results for the full parameter range $0 \leq m \leq 1$, $0 \leq M \leq 1$ are shown in figure 4.4, where the separation line between the brazil-nut effect region and the no-brazil-nut effect region is plotted for simulations (black squares), a bubble condition (red circles) explained in the following, and DFT calculations (small dots). The latter is also indicated by the background color. The brazil-nut effect is preferred when the dipole ratio M is small and in addition when the mass ratio is close to one (blue region). All results are in good agreement predicting the same trends and slope of the separation line.

4.4.2 Depletion bubble picture

In order to understand the physics behind the brazil-nut effect, a simple theory is created which results from the basic mechanisms. Therefore, the initial step is regarding a fluid of B-particles around a single A-particle. As shown in a simulation snapshot in figure 4.5, the A-particle creates a void space of radius R around it (see shaded region in figure 4.5). This *depletion bubble* does not contain any B-particles as they are repelled from the A-particle. By using the buoyancy criterion for this bubble, the area of the A-particle is increased and by this the effective weight per area reduces. Furthermore, the density distribution of the B-particles is assumed to be homogeneous $\rho_{\text{B}}(\mathbf{r}) = \bar{\rho}_{\text{B}}$, so that the A-particle will be

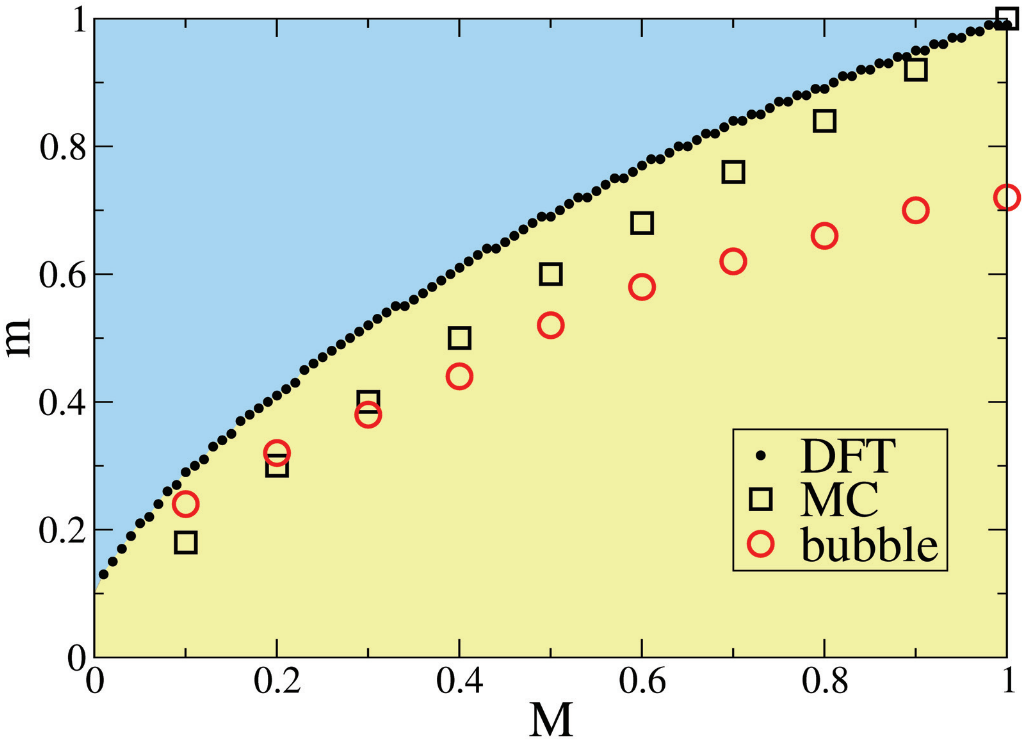

Figure 4.4: *Line separating the brazil-nut (blue) and no-brazil-nut regime (yellow) where the color code denotes the DFT results. Results from MC simulations are indicated with black squares and the separation line obtained by the bubble condition is denoted with red circles.*

lifted if

$$\frac{m_{\mathrm{A}}}{\pi R^2} < m_{\mathrm{B}}\bar{\rho}_{\mathrm{B}} \tag{4.25}$$

is fulfilled. At low densities, the density distribution of the B-particles around an A-particle located at the origin becomes

$$\bar{\rho}_{\mathrm{B}} \exp\left(-\frac{\phi_{\mathrm{AB}}(r)}{k_B T}\right) = \bar{\rho}_{\mathrm{B}} \exp\left(-\frac{M\Gamma l_{\mathrm{A}}^3}{r^3}\right), \tag{4.26}$$

so that the radius R of the depletion bubble can be extracted when the interaction potential is of the order $k_B T$. Thus, this results in

$$R = l_{\mathrm{A}}(M\Gamma)^{1/3}. \tag{4.27}$$

Substituting this into equation (4.25), the *bubble condition* for the brazil nut effect separation line can be written as

$$m > \frac{1}{\pi\,(M\Gamma)^{2/3}\,l_{\mathrm{A}}^2\bar{\rho}_{\mathrm{B}}} \tag{4.28}$$

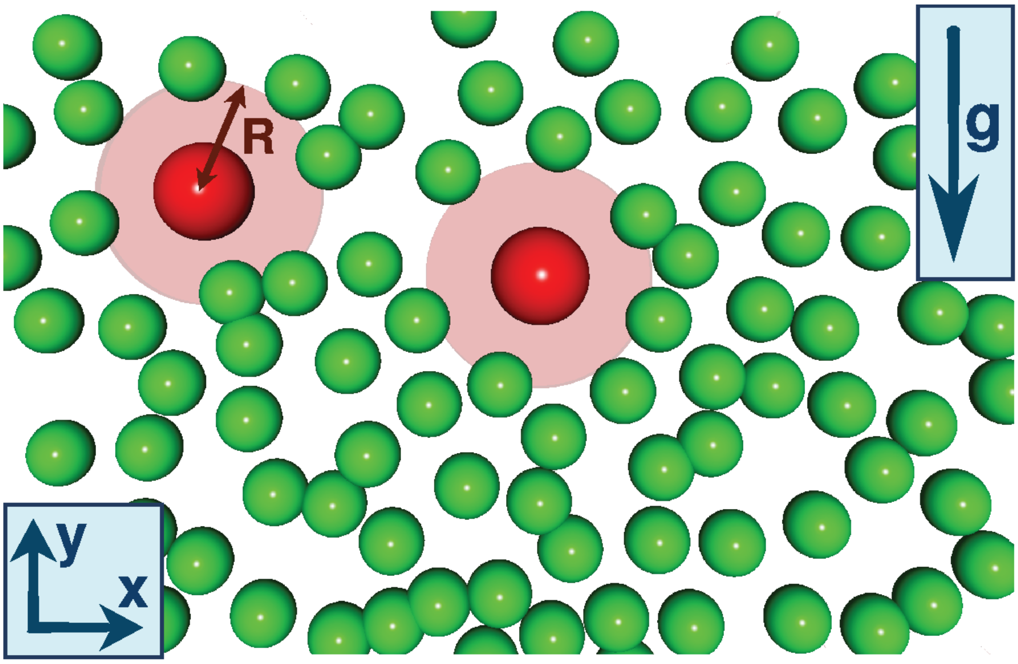

Figure 4.5: *MC simulation snapshot of two* A*-particles (red spheres) in a fluid of* B*-particles (green spheres). The depletion zone caused by the* B*-particle fluid is illustrated in faint red as a sphere of radius* R *around each* A*-particle.*

The left unknown parameter is the averaged density $\bar{\rho}_{\mathrm{B}}$ which can be obtained from simulations as the effective density at distance $2R$,

$$\bar{\rho}_{\mathrm{B}} = \rho_{\mathrm{B}}^{\mathrm{eq}}(2R). \tag{4.29}$$

As already mentioned, the results are plotted in figure 4.4 as red circles. Even though this theory is very simple, it reproduces the trends from simulation well. Based on the long-range repulsion, the mechanism will not occur for hard sphere mixtures. Nevertheless, it can be found if the interaction is described as an effective hard sphere interaction [164] so that sedimentation can be examined.

4.4.3 Boundary layering and effective interaction with the bottom wall

At last, the effect of the bottom wall and resulting layering effects are examined. Therefore, the depletion bubble of a single A-particle is regarded when the particle is close to or at the bottom wall of the system ($y = 0$). In figure 4.6, a snapshot from MC simulations is shown for $M = 0.1$ and $m = 0.5$ where a full layer of heavier A-particles is located directly at the wall. Considering a single A-particle at height $y < R$ with R denoting the radius of the depletion bubble, the closer the particle approaches the bottom wall, the

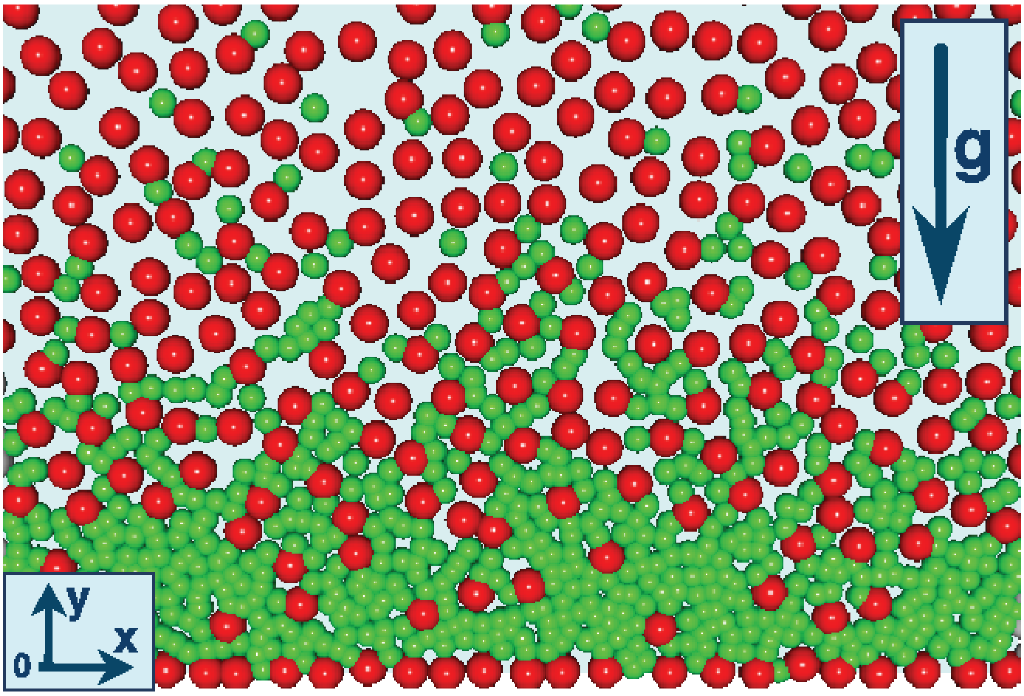

Figure 4.6: *MC simulation snapshot for $M = 0.1$, $m = 0.5$ illustrating the bottom layer of* A*-particles (red spheres) at $y = 0$ and the fluid of* B*-particles (green spheres) above. The direction of gravity is denoted by an arrow pointing to the $-y$-direction.*

more the area of the bubble reduces. In the limit when the particle is located at the wall, the area has become half of the full circle in the bulk (see situation I in figure 4.7) .

Accordingly, the area $A(y)$ of the depletion bubble depending on the height y can be described analytically under the condition that the radius R of the depletion bubble remains constant, resulting in

$$A(y) = R^2 \begin{cases} \pi - \arccos(\frac{y}{R}) + \frac{y}{R}\sqrt{1-\left(\frac{y}{R}\right)^2} & , \quad \text{for } y \leq R, \\ \pi & , \quad \text{otherwise.} \end{cases} \tag{4.30}$$

Due to the increasing area, two competing effects occur. On the one hand, work against the osmotic pressure $\bar{p}_\mathrm{B}$ of the homogeneous fluid of B-particles has to be performed as the area $A(y)$ grows. Under the assumption of a constant pressure in the examined regime, the work becomes $\bar{p}_\mathrm{B}(A(y) - A(0))$ which causes an effective attraction of the A-particle close to the bottom wall. This situation is illustrated in figure 4.7 (II). After all, this effect is similar to the depletion attraction resulting from a colloid-polymer mixture described with the AO model in chapter 3 even though these particles have a finite radius. On the other hand, the buoyancy is effected when the area $A(y)$ increases. The buoyant force reads $-m_\mathrm{A}g + \bar{\rho}_\mathrm{B} m_\mathrm{B} g A(y)$, which will become opposed to the depletion force if the weight of the bubble is lighter than that of the surrounding fluid.

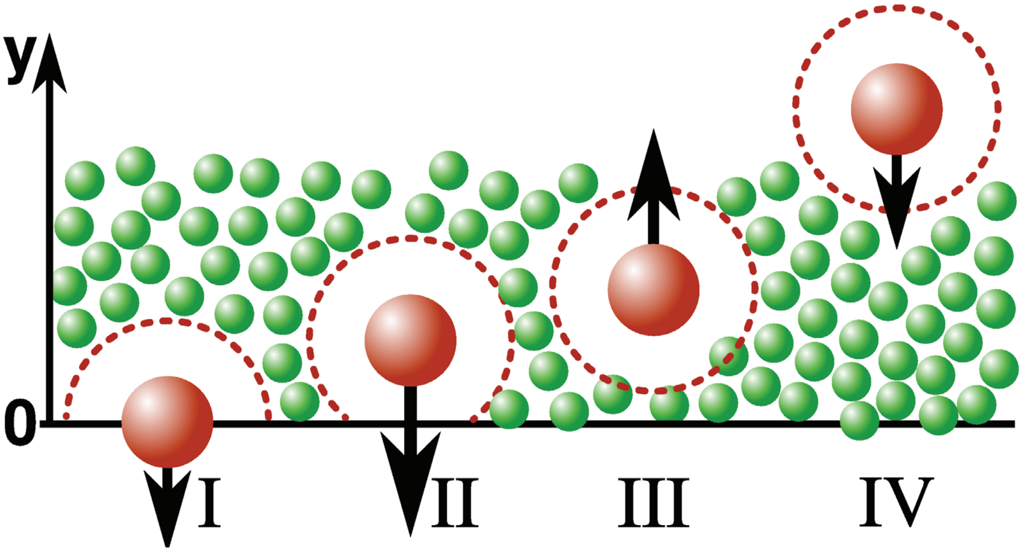

Figure 4.7: *Schematic plot of four situations of a single* A*-particle (red sphere) close to the bottom wall of the box (*$y = 0$*) in a fluid of green* B*-particles. The depletion zone for each* A*-particle is shown as a dashed circle and an arrow is indicating the effective force acting on the* A*-particle where the direction depends on the distance* y *from the bottom wall.*

Consequently, the depletion potential $V(y)$ of a single A-particle with the bottom wall can be expressed analytically resulting in

$$V(y) = \begin{cases} \bar{p}_\mathrm{B}\left(A(y) - \pi\frac{R^2}{2}\right) + m_\mathrm{A} g y - \bar{\rho}_\mathrm{B} m_\mathrm{B} g \int\limits_0^y \mathrm{d}y' A(y') & \text{for } y \geq 0 \\ \infty & \text{for } y < 0 \end{cases} \tag{4.31}$$

including an integral which becomes

$$\int\limits_0^y \mathrm{d}y' A(y') = \pi R^2 y - R^2 y \arccos\left(\frac{y}{R}\right) + R^3\sqrt{1 - \frac{y^2}{R^2}} - \frac{R^3}{3}\left(1 - \frac{y^2}{R^2}\right)^{\frac{3}{2}}. \tag{4.32}$$

As this formula requires the osmotic pressure of B-particles $\bar{p}_\mathrm{B}$, a bulk simulation of a system only consisting of B-particles is performed, so that $\bar{p}_\mathrm{B}$ results from a virial expression [165] at number density $\bar{\rho}_\mathrm{B}$.

In addition, the radius R of the depletion bubble can be renormalized by comparing it with the radius resulting from an A-particle located at the origin in a surrounding of B-particles and computing the first inflection point in the density distribution of the B-particles. The results for this R' are a bit smaller than those assessed by equation (4.27) as the latter holds only for low osmotic pressures.

Following [166, 167], the interaction of an A-particle with the bottom wall can be described as a mean-force potential. Accordingly, the effective interaction potential $V_\mathrm{eff}(y)$

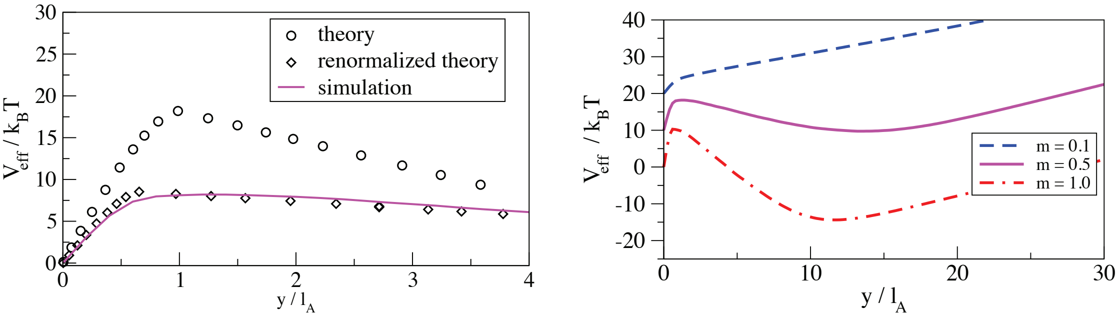

(a)

(b) $M = 0.1$

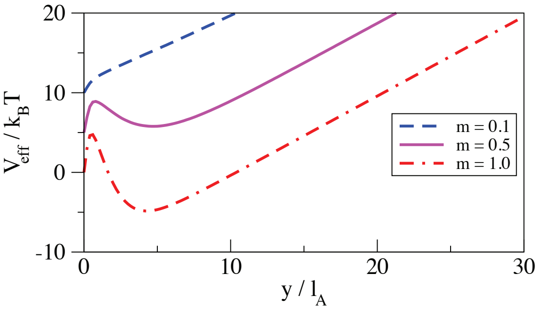

(c) $M = 0.01$

Figure 4.8: *Effective interaction potential* $V_{\text{eff}}/k_B T$ *from equation* (4.33) *for a single* A-*particle in a fluid of* B-*particles depending on the height* y/l_{A}. *(a) shows the behavior close to the bottom wall including theoretical predictions with depletion radius* R *(circles) and normalized radius* R' *(rhombs). (b) and (c) depict the effective potential for* $M = 0.1$ *and* $M = 0.01$, *respectively, where the graphs are shifted vertically for clarity.*

at height y reads

$$V_{\text{eff}}(y) = -\int_0^y \mathrm{d}y \, \langle F_{\text{A}}(y) \rangle, \tag{4.33}$$

including the canonical average of the force $\langle F_{\text{A}}(y) \rangle$ acting on the A-particle effected by the B-particles. In addition, the direct force resulting from gravity $-m_{\text{A}} g$ is included in this definition of the force $F_{\text{A}}(y)$.

However, the results from MC simulations for the effective potential $V_{\text{eff}}(y)$ are plotted in units of $k_B T$ illustrated in figure 4.8 where two possible cases can be seen. On the one hand, when the A-particle is much heavier than the B-particles (e.g., $m = 0.1$ in figures 4.8(b) and 4.8(c)), the potential is attractive throughout the whole simulation box due to gravity and depletion attraction close to the bottom wall. On the other hand, for systems where the brazil-nut effect occurs (e.g. $m = 1.0$ in figures 4.8(b) and 4.8(c)), three different regimes are examined. First, close to the bottom wall, the interaction is highly attractive resulting from the depletion attraction (cf. situations I and II in figure 4.7). When the depletion bubble is not cut by the bottom wall, the A-particle is repelled due

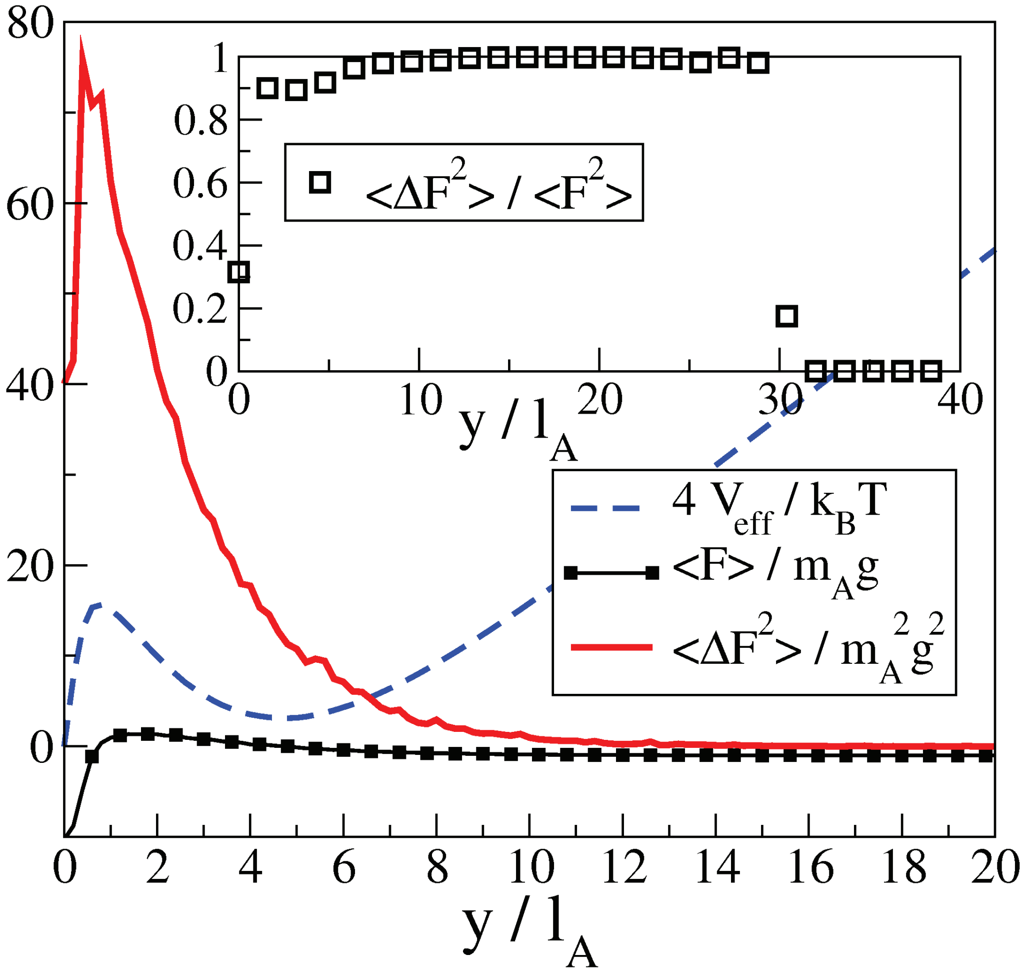

Figure 4.9: *Mean square fluctuations of the depletion force* $\langle \Delta F^2 \rangle$ *as a function of the height* y/l_{A} *as well as relative fluctuations* $\langle \Delta F^2 \rangle / \langle F^2 \rangle$ *included in the inset, both for system parameters* $M = 0.1$ *and* $m = 0.5$.

to the buoyancy (situation III in figure 4.7). At last, when the density of B-particles is decreased, the effect of the buoyancy loses gain so that the effective interaction becomes attractive again (situation IV in figure 4.7). The direction of the effective interaction force on the A-particle is also indicated by arrows included in figure 4.7.

In figure 4.8(a), the theoretical predictions from equation (4.31) are compared to the simulation results for fixed $m = 0.5$ and $M = 0.1$ close to the bottom wall. Here, the simulation data and the rhombs illustrating the results with normalized radius R' match well, but the results without normalization (radius R) denoted by circles overestimate the simulation results significantly. However, the trends are similar, exposing that the main concepts are included in the described theory.

Next, the energetic barrier ΔE close to the wall is examined where the depletion attraction regime and the buoyancy regime coincide. Again, the results from the simulations match

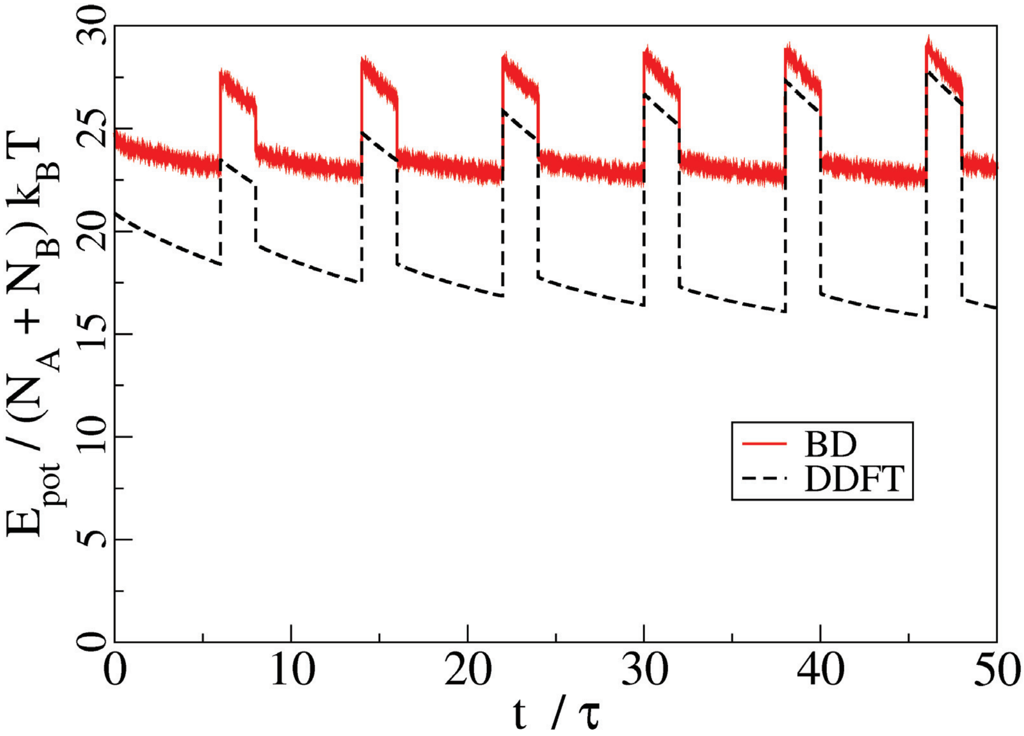

Figure 4.10: *Ensemble-averaged total potential energy $E_{\text{pot}}/(N_{\text{A}}+N_{\text{B}})$ per particle as a function of time t/τ, calculated for the time period $T_0 = 8\tau$ and the swap fraction $\vartheta = 1/4$, where the examined system parameters are $M = 0.1$ and $m = 0.24$.*

well with the predictions from theory, where both are of the order of a few k_BT. At $M = 0.1$ and $m = 0.5$, theory yields $\Delta E = 8.6k_BT$, whereas $\Delta E = 7.8k_BT$ is obtained from simulations. For a different set of parameters ($M = 0.3$ and $m = 0.9$), theory predicts $\Delta E = 15.5k_BT$ but the simulations yield $\Delta E = 9.8k_BT$. This large difference is caused by a very thin layer of B-particles.

Consequently, an A-particle trapped close to the bottom wall requires a very large time to escape as this time scales in Arrhenius-like fashion with the exponential of the barrier height ($\propto \exp(\Delta E/k_BT)$). Nevertheless, this is only the case if the barrier is treated statically. In fact, as shown in [168], the effective interaction fluctuates strongly so that the barrier is not static. Thus, the particle waits for a lowering of the potential barrier to escape from the attractive region. In order to analyze this in detail, the fluctuations of the depletion force $\langle \Delta F^2 \rangle = \langle F^2 \rangle - \langle F \rangle^2$ are computed and the results are shown in figure 4.9 as a red line. Close to the energetic barrier which is illustrated in a scaled graph in dashed blue, these fluctuations are very large decreasing with growing distance to the wall. As shown in the inset in figure 4.9, the relative fluctuations are of the order one, or in other words it becomes easy for a particle to escape from the attractive region. The key message is that even though the energetic barrier is of the order of several k_BT, A-particles can escape from the bottom wall making it is easier to equilibrate the system

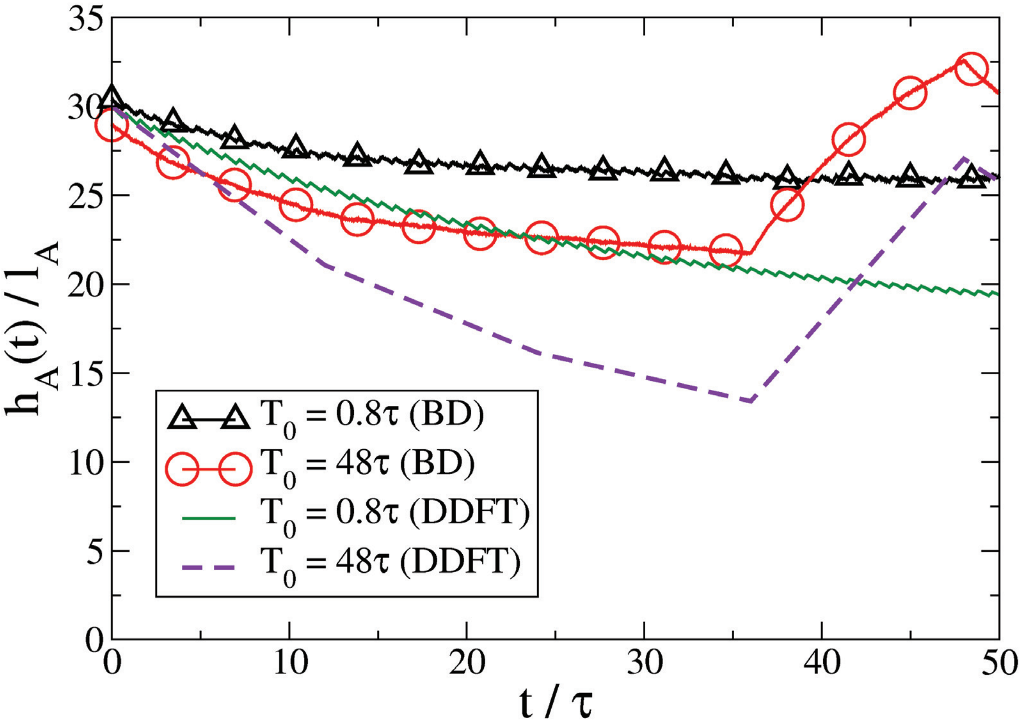

Figure 4.11: *Mean height of the* A*-particles* $h_{\mathrm{A}}(t)$ *as a function of* t/τ *for different shaking periods* T_0 *but fixed swap fraction* $\vartheta = 1/4$*. The used system parameters are* $M = 0.1$ *and* $m = 0.24$*.*

when a simulation is performed.

4.5 Results under time-dependent gravity

At last, the system is examined in the dynamical case, where the gravity field depends on time (see equation (4.6)). In order to understand this simple model of colloidal shaking, Brownian dynamics simulations as well as dynamical density functional theory calculations are performed. By varying the initial configurations of the colloid positions in the simulations resulting from bulk calculations, statistical averages can be computed which correspond to an initial homogeneous density distribution for the DDFT calculations. A non-symmetric case of the time-dependent gravity field is considered with the swap fraction $\vartheta = 1/4$ (see red plot in figure 4.2). Accordingly, averaged over time there is a net gravity acting in $-y$-direction. The steady state upon time-dependent periodic gravity is analyzed.

Thus, first the dynamical behavior needs to be examined by regarding the relaxation in time of a homogeneous fluid of A- and B-particles. Therefore, the ensemble-averaged

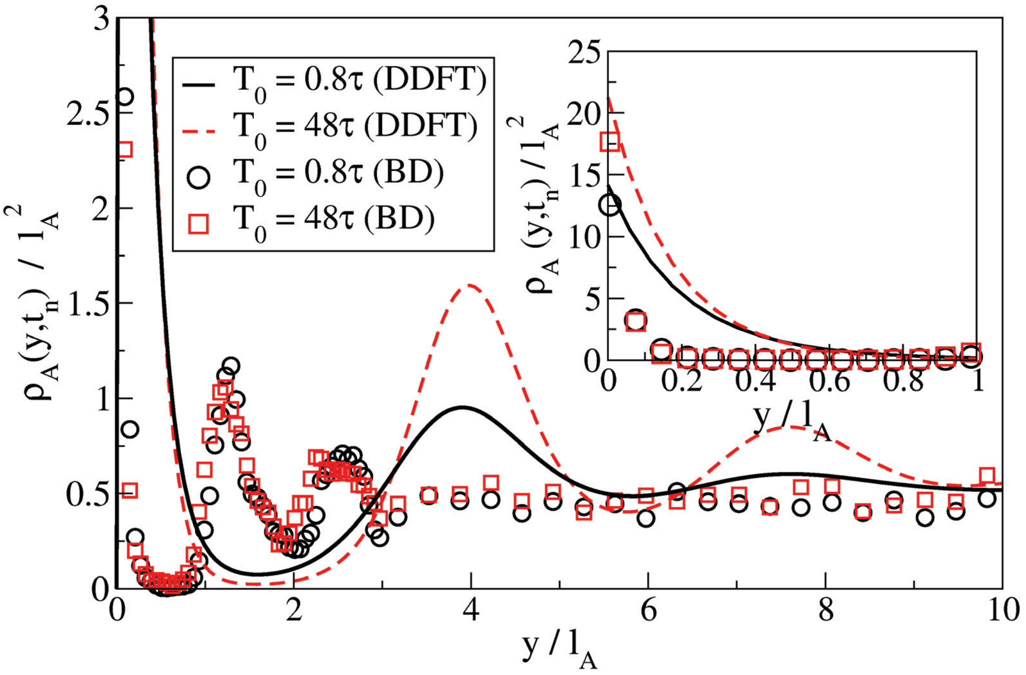

Figure 4.12: *Density profile ρ_{A} of the* A*-particles depending on the height y/l_{A} when the system is shaken with periods $T_0 = 0.8\tau$ and $T_0 = 48\tau$ at fixed swap fraction $\vartheta = 1/4$. Straight and dashed lines indicate the results from DDFT and squares as well as circles denote the BD simulation results both obtained for $M = 0.1$ and $m = 0.24$.*

total potential energy $E_{\text{pot}}(t)$ of the system (see [152]) can be observed

$$E_{\text{pot}}(t) = \frac{1}{2}\int \mathrm{d}\mathbf{r} \int \mathrm{d}\mathbf{r}' \sum_{i,j=\mathrm{A,B}} \phi_{ij}(\mathbf{r}-\mathbf{r}')\rho_i(\mathbf{r},t)\rho_j(\mathbf{r}',t) + \sum_{i=\mathrm{A,B}} \int \mathrm{d}\mathbf{r} V_{\mathrm{ext,i}}(\mathbf{r},t)\rho_i(\mathbf{r},t) \tag{4.34}$$

In figure 4.10, the time behavior of $E_{\text{pot}}(t)$ per particle is shown, where it becomes obvious that only a few oscillations are required to obtain a steady behavior. As the initial density profile is homogeneous, the amplitude of the oscillations increases with time. The results from theory and simulations differ but nevertheless, the DDFT results describe all trends of the BD simulations well but with a bigger amplitude of the oscillations.

In analogy to equation (4.23), the averaged height can be calculated using the first moment of the time dependent density profile so that it reads

$$h_i(t) = \frac{\int_0^{L_y} \mathrm{d}y\, y \rho_i(y,t)}{\int_0^{L_y} \mathrm{d}y \rho_i(y,t)}, \tag{4.35}$$

where i denotes the two species $\mathrm{A, B}$.

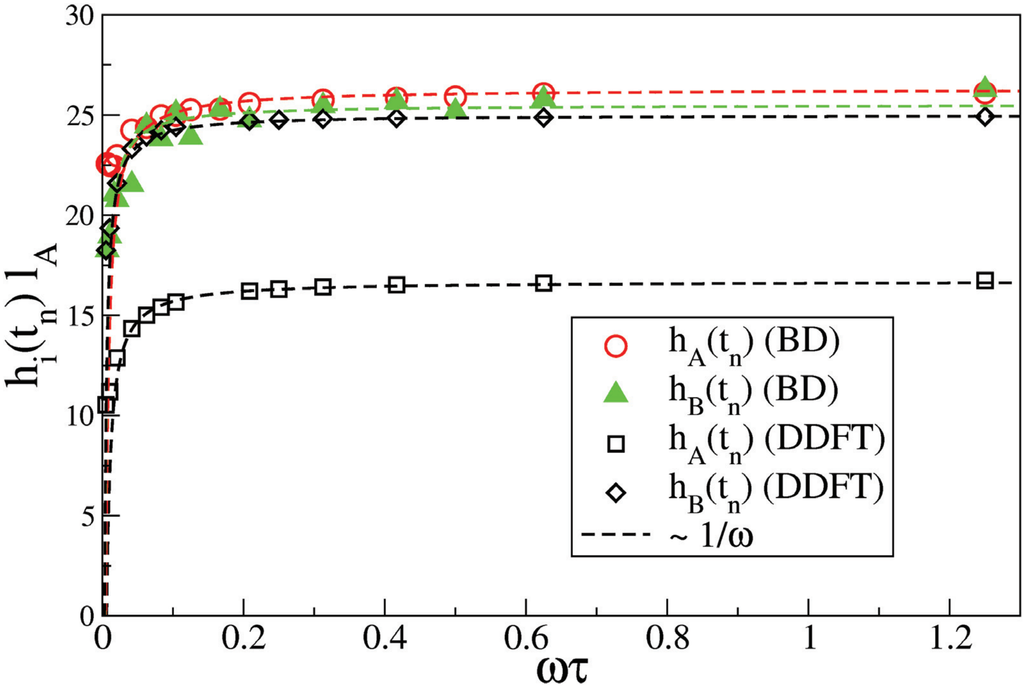

Figure 4.13: *Mean heights of* A- *and* B-*particles* h_{A} *and* h_{B} *recorded at times* t_n *plotted versus the frequency of swapping* $\omega = 2\pi/T_0$. *DDFT results (black symbols) as well as BD simulation results (colored symbols) can be fitted with the scaling law* $\propto 1/\omega$. *The chosen parameters are* $M = 0.1$ *and* $m = 0.24$.

As previously shown [169, 170], the time-dependent height can be examined as an indicative parameter to understand the dynamics of the whole system. Thus, the time dependence of the height of the A-particles $h_{\mathrm{A}}(t)$ is shown in figure 4.11 for two different frequencies of shaking $\omega = 2\pi/T_0$. Both, DDFT and simulations predict that the relaxation time is insensitive to the period T_0 but scales with the Brownian time τ. However, DDFT underestimates the heights $h_{\mathrm{A}}(t)$ in analogy to the previous results.

In order to examine the density profiles, the density distribution is regarded after the relaxation time

$$t_n = (n - \vartheta)T_0, \quad n = 1, 2, .., \tag{4.36}$$

which can be understood as the time when the cell is turned and by this, the direction of gravity is inverted. Accordingly, results from DDFT and BD simulations can be compared for different shaking frequencies and the results are presented in figure 4.12. Similar to the results for the static case, the theoretical predictions qualitatively match the results from simulations. In addition, the bottom layer still persists as shown in the inset in figure 4.12 and the amplitudes of both approaches are in good agreement. However, the deviations in DDFT result from the density expansion approach but not from the additional adiabatic approximation used to create the DDFT formalism (compare with section 2.4).

At last, the mean heights h_i with $i = \mathrm{A}, \mathrm{B}$ are analyzed for different frequencies

$\omega = 2\pi/T_0$ and the results are shown in figure 4.13. The lower the frequency is, the lower are the peak heights due to the dissipative response. In the limit of infinite frequencies $\omega \to \infty$, the system is unable to respond to the variation of the direction of gravity. Accordingly, the system remains in a state which is similar to the case of a fluid mixture confined between two parallel plates. Therefore, the peaks are much less pronounced than in the case of very low frequencies $\omega \to 0$. The latter corresponds to the static case without shaking and accordingly reproduces the results of section 4.4. In order to quantify the decay of the mean height with frequency, the crudest model of colloidal shaking is assumed, namely completely overdamped response to a periodic stimulus. Thus, the amplitude scales with the frequency of shaking via $1/\omega$. As visualized in figure 4.13, this is a good fit to the obtained data points. DDFT describes the behavior of $h_{\mathrm{B}}(t)$ well but it underestimates the heights of the A-particles. Again this can be explained by the low-density expansion which deteriorates with increasing interaction strength, so that B-particles can be described better.

4.6 Conclusions

In conclusion, a binary mixture of long-range repulsive particles has been analyzed in a two-dimensional system under the presence of gravity. Calculations using (dynamical) density functional theory as well as Monte Carlo and Brownian dynamics computer simulations were performed to obtain density profiles for each species. The more repulsive A-particles create a depletion zone induced by the B-particles which form a fluid background. Thus, the effective mass of an A-particle is decreased so that the application of Archimedes' principle results in a buoyant force lifting the A-particle. This effect can also occur when the A-particle is heavier than the B-particles, which then is called the colloidal brazil-nut effect in analogy to the granular brazil-nut effect, where heavier particles float on lighter particles after the system was shaken. This finding is in accordance with recent experimental observations [128]. These experiments were performed in a three-dimensional system with long-range repulsive interaction similar to that used in this chapter. The approach of the depletion bubble can be expanded to three dimensions. However, no brazil-nut effect occurred in the experiments as the ratios of masses and interactions were not those of the brazil-nut regime discussed in this chapter.

Using the depletion bubble picture, the effective interaction of A-particles with the bottom wall of the confining container can be computed resulting in an attraction induced by entropy. Consequently, layering can occur at the bottom which was analyzed in this chapter. Even in the case of time-dependent gravity which is similar to shaking, the boundary layer persists. However, this effect as well as the brazil-nut effect are expected to occur for other long-range repulsive interactions and for three-dimensional systems. Thus, it can be verified by future experiments on charged colloidal mixtures, charged granulates, or dusty plasmas. When the pair interaction in three dimensions is not radially symmetric, the sedimentation will become more complicated due to anisotropic effects, but this is beyond the scope of this work.

Comparing the results from density functional theory with those obtained from computer simulations, qualitative but no quantitative agreement occurs. This can be explained by the usage of a density expansion for the excess free energy functional. In order to give a quantitative prediction of the brazil-nut effect, more sophisticated functionals which are valid for soft repulsive mixtures on a wide density range have to be developed. This can be seen as a challenge for future work.

In future work, other interaction potentials can be examined as for example strongly attractive particles resulting from a binary mixture of oppositely charged colloids [171,172]. An interesting question is whether other systems also feature the brazil-nut effect. Furthermore, an additional external field as for example an electric field can be added to the gravitational potential so that the system can be tuned better [173]. The latter set-up is especially interesting for electronic ink [174,175].

CHAPTER 5

Hard disks on patterned substrates

The following chapter is based on publication [3] which consists of theoretical calculations using density functional theory, and simulations performed by Matthieu Marechal. Michael Schmiedeberg and Hartmut Löwen contributed by combining the results from both approaches.

The adsorption of a monolayer of particles on a substrate leads to a variety of interesting situations, especially when the symmetry of the substrate is incompatible to that of the phase the particles would form on an unstructured substrate. In the incompatible case, there is a competition between the two resulting phases. Already in 1937, Landau [176] showed that there is a first order phase transition in the case of incompatible symmetries. The phase behavior of particles affected by a substrate potential has been widely studied. For example, substrates with a one dimensional commensurate structure, which induce the triangular structure hard disks would form on a flat surface, have been examined [177–181]. By increasing the complexity of the substrates, additional phases can be obtained [182–195], where periodic or even aperiodic structures were examined. If the interaction between particles and a substrate is weak, the resulting phase has the same symmetry as it would form on a flat substrate. But if the interaction is strong, the symmetry of the substrate is favored. In addition, new phases can be found at intermediate substrate strengths, as it has been done for nanoparticles or micron-sized colloids [182, 185, 188, 191, 194], for vortices in type-II superconductors [196, 197], for adsorbed atoms (see for example [186, 187, 189, 190, 198, 199]) or even molecules (as presented in a recent review [200]). Defect-mediated melting theory [201] also predicts additional phases at intermediate interaction strengths.

In this chapter, a minimal model system is assumed to examine the competition of incommensurate symmetries. Accordingly, hard disks which are adsorbed on a two-dimensional substrate with square symmetry are explored under the condition, that on average only one particle is located at each minimum of the substrate. In figure 5.1, a schematic depiction is shown. In the absence of the external potential and for sufficiently high densities, hard disks form a triangular solid with a quasi-long range order [202]. Accordingly, the triangular phase is favored by the hard disks even when they are adsorbed on a substrate with square symmetry. In order to obtain the phase behavior depending on packing fraction η and strength of the particle-substrate interaction V_0, fundamental-measure density functional theory (DFT) calculations as well as Monte Carlo (MC) computer simulations were performed. At low packing fractions, the particles form a modulated fluid with square symmetry which is caused by the symmetry of the substrate. When the packing fraction is increased, a rhombic preordering is found resulting from the incompatibility of the different symmetries prior to the first order phase transition into the triangular solid which is found at higher packing fractions. This rhombic ordering consists of particles still bound to the minima of the square substrate but which are shifted from the potential minima. Every second row or every second column is displaced in one direction, while the other rows or columns are shifted to the opposite direction. Resulting from this, the disks have a larger mean distance between each other so that this ordering can be understood as a precursor for the triangular phase in which the particle distances are maximal. The mean-field DFT predicted a second-order square-fluid to rhombic phase transition what was not confirmed by the MC simulations. In contrast, the latter yielded a continuous crossover from the modulated fluid phase to the rhombic structure. These findings suggest a more general mechanism which results from two competing incommensurate symmetries. The preordering structure is formed as a consequence of the competing phases and thus, inherits its properties from both of these. In addition, there is a reentrant square-rhombic phase transition which occurs when the substrate strength is increased.

In order to confirm the results, experiments can be performed with sterically-stabilized colloids which are located on a flat surface or at an air-water interface and exposed to a laser field which creates the symmetry of the external potential. This is similar to previous experiments with colloidal particles where the external potential was caused by laser fields [177–183, 185, 191, 194, 203]. Very strong square substrates have already been examined [182, 184, 192, 204], but commonly under the condition of multiple particles per potential minimum [182, 184, 185, 192].

5.1 System

The examined system consists of hard disks on a two-dimensional substrate located in the (x, y)-plane. Thus, the particles interact via a hard-body pair potential (see equation (2.34))

$$\phi_{ij}(r) \quad = \quad \begin{cases} \infty & \text{, for} \quad r < \sigma \\ 0 & \text{, otherwise,} \end{cases} \tag{5.1}$$

where σ is the diameter of the disks. As common in DFT calculations, the system has periodic boundary conditions in both directions mimicking in an effective infinite two-dimensional system. The underlying substrate in contrast to the bulk is described by an

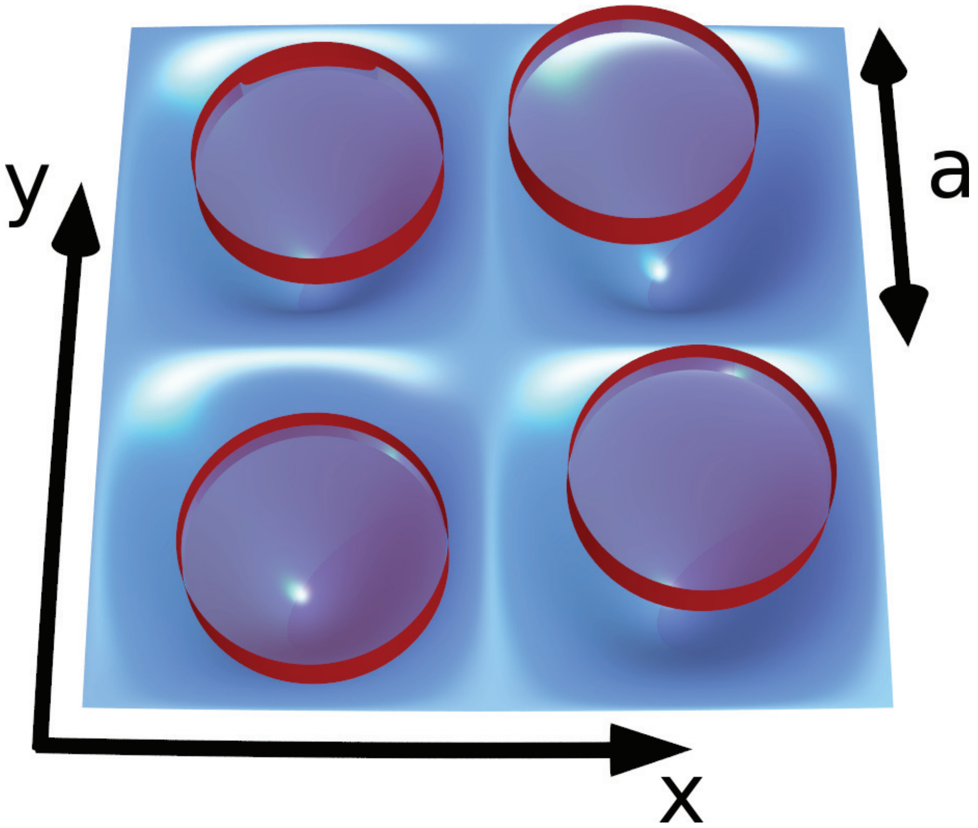

Figure 5.1: *Schematic view of the square substrate potential of lattice constant a and the particles of diameter σ where each potential minimum on average contains exactly one particle.*

external potential $V_{\text{ext}}(x,y)$ given by

$$V_{\text{ext}}(x,y) = V_0\left(1 - \frac{1}{4}\left|\sum_{j=1}^{4} e^{i\mathbf{k}_j\cdot\mathbf{r}}\right|^2\right). \tag{5.2}$$

Here, V_0 is the amplitude of the external field, which is conveniently expressed in units of k_BT. The $\{\mathbf{k}_j\}$ denote the reciprocal lattice vectors, which in this case are given by the four $\{\mathbf{k}_j\} = \{(\pm1,\pm1)\frac{\pi}{a}\}$ with lattice constant a. In order to implement this potential, a simpler, equivalent expression can be used, that is

$$V_{\text{ext}}(x,y) = V_0\left[1 - \frac{1}{4}\left(1-\cos(k_x x)\right)\left(1-\cos(k_y y)\right)\right], \tag{5.3}$$

with $k_x = k_y = \frac{2\pi}{a}$. The lattice has a square-symmetry with edge length a as illustrated in figure 5.1. Here, a three-dimensional plot of the height map of $V_{\text{ext}}(x,y)$ is shown. In addition, a schematic view of 2×2 particles of diameter σ — which also serves as length scale — is illustrated, where each of the disks on average is located near a potential minimum. Consequently, the system is examined for *unit filling* which means, that the areal number density is given by $1/a^2$ so that the dimensionless area packing fraction of the system reads

$$\eta = \pi\sigma^2/4a^2. \tag{5.4}$$

5.2 Density Functional Theory

The starting point for DFT calculations is the grand canonical free energy $\Omega(T, \mu, A, [\rho(\mathbf{r})])$ at fixed temperature T, chemical potential μ and area A. This free energy can be split up as explained in section 2.2 resulting in

$$\Omega[\rho(\mathbf{r})] = \mathcal{F}_{\text{id}}[\rho(\mathbf{r})] + \mathcal{F}_{\text{ext}}[\rho(\mathbf{r})] + \mathcal{F}_{\text{exc}}[\rho(\mathbf{r})], \tag{5.5}$$

which contains the exactly known functional for the ideal gas in two dimensions $\mathcal{F}_{\text{id}}[\rho(\mathbf{r})] = k_B T \int \mathrm{d}\mathbf{r}\rho(\mathbf{r}) \left[\ln\left(\Lambda^2\rho(\mathbf{r})\right) - 1\right]$ including the (irrelevant) thermal wavelength Λ. In addition, the coupling to the external potential of equation (5.3) is required that is given by

$$\mathcal{F}_{\text{ext}}[\rho(\mathbf{r})] = \int \mathrm{d}\mathbf{r}\rho(\mathbf{r})[V_{\text{ext}}(\mathbf{r}) - \mu]. \tag{5.6}$$

The third term is the excess free energy functional which was recently developed [49] and outlined in section 2.3.3. The excess free energy density of equation (2.59) is rewritten split up into components so that it becomes

$$\begin{aligned}\Phi = -n_0 \ln(1-n_2) + \frac{1}{4\pi(1-n_2)}\cdot \\ \left(\frac{19}{12}(n_1)^2 - \frac{5}{12}((\mathbf{n}_1)_x^2 + (\mathbf{n}_1)_y^2) - \frac{7}{6}((\hat{\mathbf{n}}_1)_{xx}^2 + 2(\hat{\mathbf{n}}_1)_{xy}^2 + (\hat{\mathbf{n}}_1)_{yy}^2\right).\end{aligned} \tag{5.7}$$

Here, $(\mathbf{n}_1)_i$ denotes the i-th entry of vector $\mathbf{n}_1$, and analogously $(\hat{\mathbf{n}}_1)_{ij}$ labels the element of the tensor $\hat{\mathbf{n}}_1$ at position ij, so that for example $(\hat{\mathbf{n}}_1)_{xx}$ indicates the upper left entry. In order to minimize the grand canonical free energy given by equation (5.5), the functional derivatives of the excess free energy density with respect to weighted densities (see equation (2.15)) need to be performed in analogy to equation (3.10). The resulting derivatives with respect to the scalar and vector weights are

$$\begin{aligned} T_2 &= \frac{n_0}{1-n_2} + \frac{1}{4\pi(1-n_2)^2}\left(\frac{19}{12}(n_1)^2 - \frac{5}{12}\mathbf{n}_1\cdot\mathbf{n}_1 - \frac{7}{6}\hat{\mathbf{n}}_1\hat{\mathbf{n}}_1\right), \\ T_1 &= \frac{19}{24\pi(1-n_2)}n_1, \\ T_0 &= -\ln(1-n_2), \\ \mathbf{T}_1 &= -\frac{5}{24\pi(1-n_2)}\mathbf{n}_1, \end{aligned} \tag{5.8}$$

while the derivatives with respect to the components of the tensorial weighted density read

$$\begin{aligned}(\hat{\mathbf{T}}_1)_{xx} &= -\frac{7}{12\pi(1-n_2)}(\hat{\mathbf{n}}_1)_{xx},\\ (\hat{\mathbf{T}}_1)_{yy} &= -\frac{7}{12\pi(1-n_2)}(\hat{\mathbf{n}}_1)_{yy},\\ (\hat{\mathbf{T}}_1)_{xy} &= -\frac{7}{6\pi(1-n_2)}(\hat{\mathbf{n}}_1)_{xy}.\end{aligned} \tag{5.9}$$

As the convolutions of the densities with the weight functions are easier to compute in Fourier space (compare with section 3.2), it is preferred to know the Fourier transforms of the weight functions analytically. This is possible in this case:

$$\begin{aligned}\mathrm{FT}(\omega_2)(k) &= \frac{R}{k}J_1(kR),\\ \mathrm{FT}(\omega_1)(k) &= RJ_0(kR),\\ \mathrm{FT}(\omega_0)(k) &= 2\pi J_0(kR),\\ \mathrm{FT}(\boldsymbol{\omega}_1)(k) &= -iR\frac{\mathbf{k}}{k}J_1(kR),\\ \mathrm{FT}(\hat{\boldsymbol{\omega}}_1(k)) &= -R\frac{\mathbf{k}\mathbf{k}}{k^2}J_2(kR)+\frac{\hat{\mathbf{1}}}{k}J_1(kR),\end{aligned} \tag{5.10}$$

where the J_n denote the Bessel functions of first kind, defined as [34]

$$J_n(z) = \left(\frac{1}{2}z\right)^n \sum_{l=0}^{\infty}(-1)^l \frac{\left(\frac{1}{4}z^2\right)^l}{l!\Gamma(n+l+1)}, \tag{5.11}$$

with the gamma-function $\Gamma(z) = \int_0^\infty \mathrm{d}t e^{-t}t^{z-1}$.

With this knowledge, the equilibrium density profiles can be obtained in analogy to the three-dimensional case, see equation (3.20).

5.3 Results on a substrate

Similar to chapter 3.2.1, the bulk behavior of hard disks can be explored as it was done previously for the density functional theory supplied above [49], resulting in a fluid and a solid phase, and a small coexistence region between both. However, under the constraint of a single particle per minimum of the external potential, the coexistence region cannot be found. In this section, first the phase diagram, depending on the area packing fraction η and the strength of the substrate interaction V_0/k_BT resulting from density functional theory calculations is shown, followed by a simpler analytic version of DFT. Finally the results from Monte Carlo simulations are presented.

5.3.1 Phase diagram from DFT

By using a common Picard iteration scheme [15], the grand-canonical free energy Ω given by equation (5.5) can be freely minimized on a fine grid. The area packing fraction η can be fixed by using the chemical potential μ as a Lagrangian multiplier and by this adapting the number of particles in analogy to the previous chapter 4. The resulting phase diagram is shown in figure 5.2. For a vanishing external potential $V_0 = 0$, the results for the hard disk freezing transition [49] between a disordered fluid and a hexagonal crystal are recovered. This freezing transition is first order in this approximation of the DFT [49]. By increasing the amplitude of the external potential V_0, the disks in the fluid phase arrange on the square substrate and by this form a modulated square fluid phase. The density profile of this modulated fluid phase is illustrated in inset (a') of the phase diagram shown in figure 5.2, where black crosses indicate the positions of the potential minima.

As the external potential suppresses the triangular structure, the phase transition to the solid phase is shifted to higher packing fractions. For reduced amplitudes higher than $V_0/k_BT = 0.82$, an additional rhombic ordering occurs (see figure 5.2, inset (a”) and 5.2(b)). This structure can be understood as a shift of all even numbered rows or columns away from the positions of the potential minima in one of the four possible directions while the odd numbered rows or columns are displaced in the opposite way. In principle, the square to rhombic transition can be continuous in analogy to a Martensitic transition [205].

However, the DFT results show that this square to rhombic transition is second order as indicated by a kink in the pressure, where the pressure is the derivative of the grand canonical free energy with respect to the packing fraction. In contrast, the transition of either the modulated fluid or the rhombic phase into the triangular solid is first order resulting from the incompatibility of the two structures. The density contour plot of the latter is shown in figure 5.2(c). This hexagonal crystal is distorted by the square substrate. In the thermodynamic limit, this is expected to be either square order, with a quasi-long range order which does not show up in the density profile, or it is long-range, distorted hexagonal.

In a specific range of area packing fractions η, there is a reentrant effect when the amplitude of the external potential V_0 is increased which can be understood from the interplay of the substrate potential and entropy. In the region of low interaction strengths, entropy, which is mainly limited by interactions with the neighboring particles, can be increased by the creation of a rhombic structure. The rhombic structure has a larger mean distance between two particles. However, at higher amplitudes V_0, all fluctuations are suppressed to a point where there is hardly any interaction between the particles, so that the square structure of the external potential is adopted.

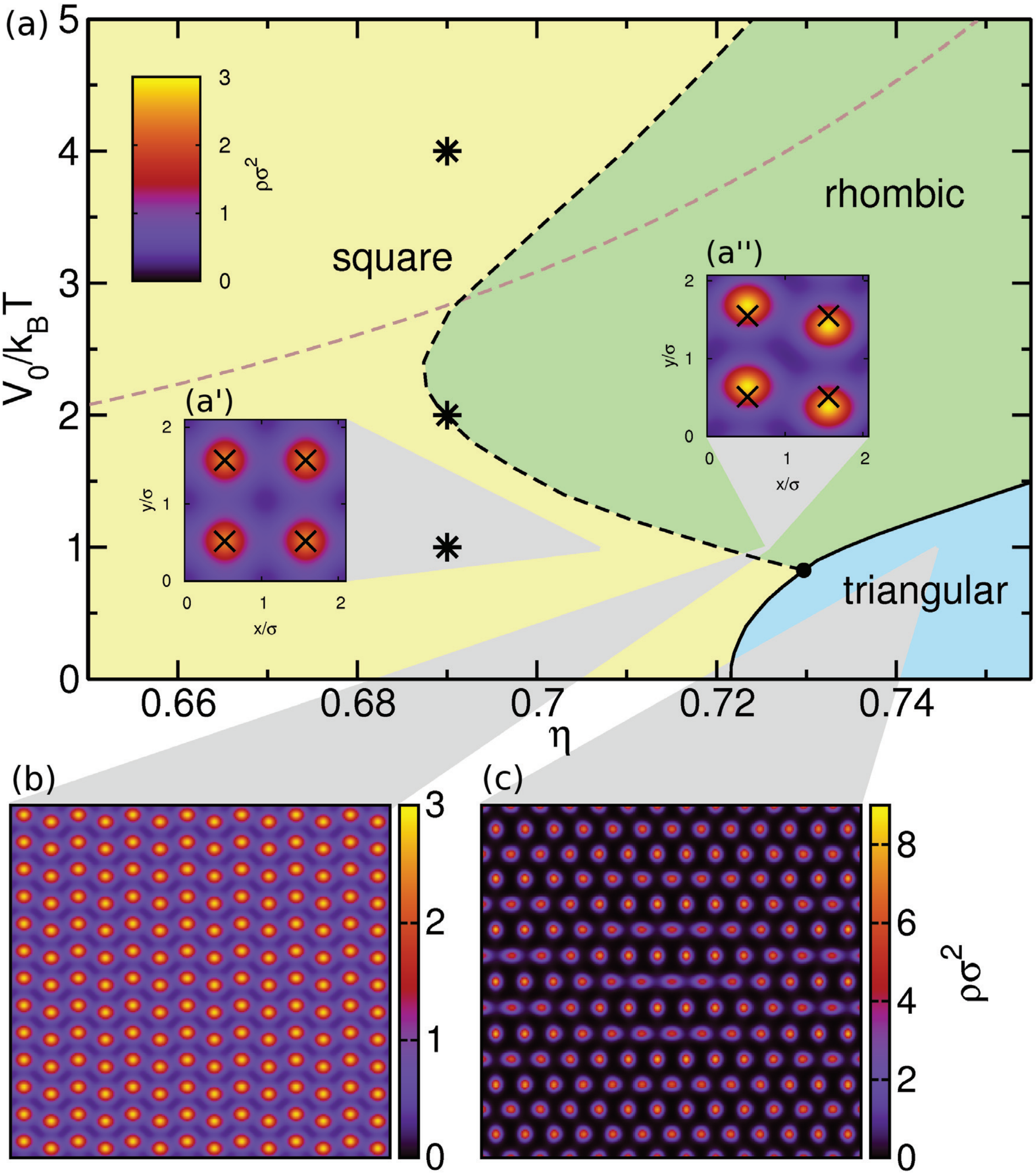

Figure 5.2: *(a) Phase diagram for hard disks on a square-substrate showing the three different phases, square modulated fluid (yellow), rhombic (green), and triangular crystal (blue). The dashed line indicates the second order and the solid line the first order phase transition, where the dot denotes the triple point. In dashed brown the results from the Gaussian approximation of section 5.3.2 are plotted. Density contour plots of the three phases are included obtained for a fixed external potential with* $V_0/k_BT = 1$ *and packing fractions (a')* $\eta = 0.7069$, *[(a”), (b)]* $\eta = 0.7257$, *and (c)* $\eta = 0.7383$. *The stars indicate the simulation parameters for figure 5.4.*

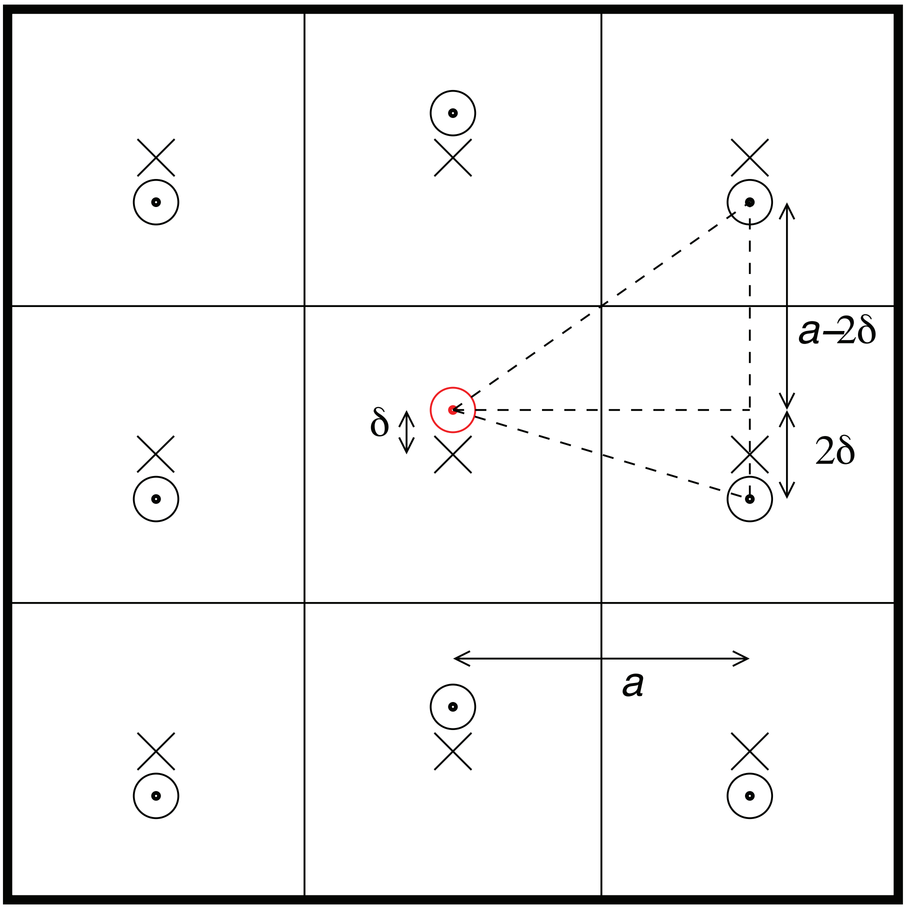

Figure 5.3: *Schematic view of a particle (red circle) and its eight nearest neighbor particles (black circles) forming a rhombic phase and thus, shifted by a length δ from the positions of the potential minima (black crosses) of a square potential with length a.*

5.3.2 Gaussian approximation

The competition between nearest neighbor interactions and the interaction with the substrate potential can still be studied with a much simpler analytic model that consists of a grand canonical free energy functional resulting from a convolution with a Gaussian weight function of range σ. This approach is presented in the following.

For the grand canonical free energy, the same ansatz as in equation (5.5) is applied which reads

$$\Omega[\rho(\mathbf{r})] = \mathcal{F}_{\text{id}}[\rho(\mathbf{r})] + \mathcal{F}_{\text{exc}}[\rho(\mathbf{r})] + \mathcal{F}_{\text{ext}}[\rho(\mathbf{r})]. \tag{5.12}$$

However, the excess free energy is assumed in analogy to [31, 206] by

$$\mathcal{F}_{\text{exc}}[\rho(\mathbf{r})] = \int \mathrm{d}\mathbf{r} \int \mathrm{d}\mathbf{r}' \rho(\mathbf{r})\rho(\mathbf{r}')c(|\mathbf{r} - \mathbf{r}'|), \tag{5.13}$$

which contains a convolution of the density distribution $\rho(\mathbf{r})$ with an interaction kernel given by

$$c(r) = Me^{-r^2/\nu^2}. \tag{5.14}$$

This kernel corresponds to soft inter-particle interactions with $\nu = \sigma/2$ for particles with diameter σ. In order to normalize this kernel, the prefactor M is chosen such that the second moment of the two-dimensional fitted Percus-Yevick direct correlation function $c^{(2)}(r)$ is recovered. The latter was derived to be [207]

$$c^{(2)}(r) = a\Delta V + b\Delta A + g, \tag{5.15}$$

where a and b are two functions given by

$$\begin{aligned} a =& \frac{1 + \chi(2\eta - 1) + 2\eta g}{\eta}, \\ b =& \frac{\chi(1-\eta) - 1 - 3\eta g}{\eta}, \end{aligned} \tag{5.16}$$

including

$$\begin{aligned} g =& \sqrt{\frac{2 + 0.256\eta + 0.081\eta^2 + 0.213\eta^3 - 0.12\eta^4)}{2(1-\eta)^3}}, \\ \chi =& \frac{1 + \eta + 0.384\eta^2 - 0.02\eta^3 + 0.246\eta^4 - 0.18\eta^5}{(1-\eta)^3}, \end{aligned} \tag{5.17}$$

and the volume and area elements which are

$$\begin{aligned} \Delta V =& \frac{2}{\pi}\left(\arccos\left(\frac{r}{\sigma}\right) - \frac{r}{\sigma}\sqrt{1 - \left(\frac{r}{\sigma}\right)^2}\right), \\ \Delta A =& \frac{2}{\pi}\arccos\left(\frac{r}{\sigma}\right). \end{aligned} \tag{5.18}$$

Performing the calculation of the second moment, the normalization factor using the previously defined value of $\nu = \sigma/2$ becomes

$$M = a + 3b + 8g. \tag{5.19}$$

However, only nearest neighbor interaction is assumed, so that a particle interacts only with eight of its neighbors. In figure 5.3, a particle (red circle) with its nearest neighbors (black circles) is schematically illustrated. Particle i is located at position $\mathbf{R}_i$, which is shifted from the position of the minimum of the underlying square potential by a value δ. Consequently, the density distribution of a single particle i can be described by a Gaussian peak of width α located at position $\mathbf{R}_i$. Hence, the density distribution of all particles is given by

$$\rho(\mathbf{r}) = \frac{4\eta\alpha}{\pi^2\sigma^2} \sum_j e^{-\alpha(\mathbf{r}-\mathbf{R}_j)^2}, \tag{5.20}$$

where the sum runs over all nearest neighbors j. Resulting from this, the grand canonical free energy can be calculated analytically but the minimization needs to be performed numerically. The resulting square-rhombic transition line is included in figure 5.2 as the dashed, brown line. This approximative theory for soft interactions recovers the trends of the more exact approach explained before. Accordingly, a rhombic preordering can be expected for any system which favors locally triangular structures but is forced to conform to a square lattice caused by any external mean. Nevertheless, this analytic model lacks the reentrant behavior, or in other words, there is no prediction of a transition from the rhombic back into the square phase when the substrate strength is decreased. In the case of small interaction strengths, the system becomes fluid with small modulations caused by the substrate potential. While the fluid phase and thus, the reentrant transition is not included in this analytic model, it can be predicted with DFT and this prediction is confirmed by Monte Carlo simulations as shown in the following section.

5.3.3 Simulation results

In order to perform Monte Carlo simulations, a system with fixed particle number N, area $A = Na^2$, and temperature T is assumed. In figure 5.4, typical configurations for three different substrate strengths V_0 are shown, along with the corresponding scattering function or structure factor $S(\mathbf{k})$ at fixed packing fraction $\eta = 0.69$ well below the bulk phase transition described before. In the regime of weak substrate potentials, small clusters of hexagonal order are formed, which also occur in the fluid in the absence of an external potential ($V_0 = 0$). Due to the external field, the clusters are aligned such that rows of particles occupy the minima of the external potential in one of the two possible directions. The scattering function of this constellation shows a twelve-fold symmetry resulting from the superposition of two scattering profiles as predicted by Nelson [201]. Both of these two scattering profiles exhibit hexagonal local order but the second profile is rotated by an angle of 90° compared to the first profile. In the case of $V_0/k_BT = 2$, as shown in figure 5.4(b), the resulting structure is completely different. A locally rhombic structure is obtained caused by the competition of the substrate potential which is minimized by a square phase, and the free volume which is increased for a triangular local structure. The formation of *equilibrium* rhombic clusters, that are aligned along the two different directions, leads to a finite ranged rhombic order. The shifted rows cause large peaks at $\mathbf{k} = (2\pi/a)\,(1, 1/2)$ in between the main peaks, which can be seen in the scattering function plot in figure 5.4(b). For large amplitudes, $V_0/k_BT = 4$ (illustrated in figure 5.4(c)), the particles are forced to be close to one of the potential minima forming a square structure.

The scattering functions $S(\mathbf{k})$ plotted in figure 5.4 are calculated using a Fast Fourier transform $\mathrm{FT}(\rho_{\mathrm{inst}})(\mathbf{k})$ of the instantaneous density profiles of the corresponding snapshots on

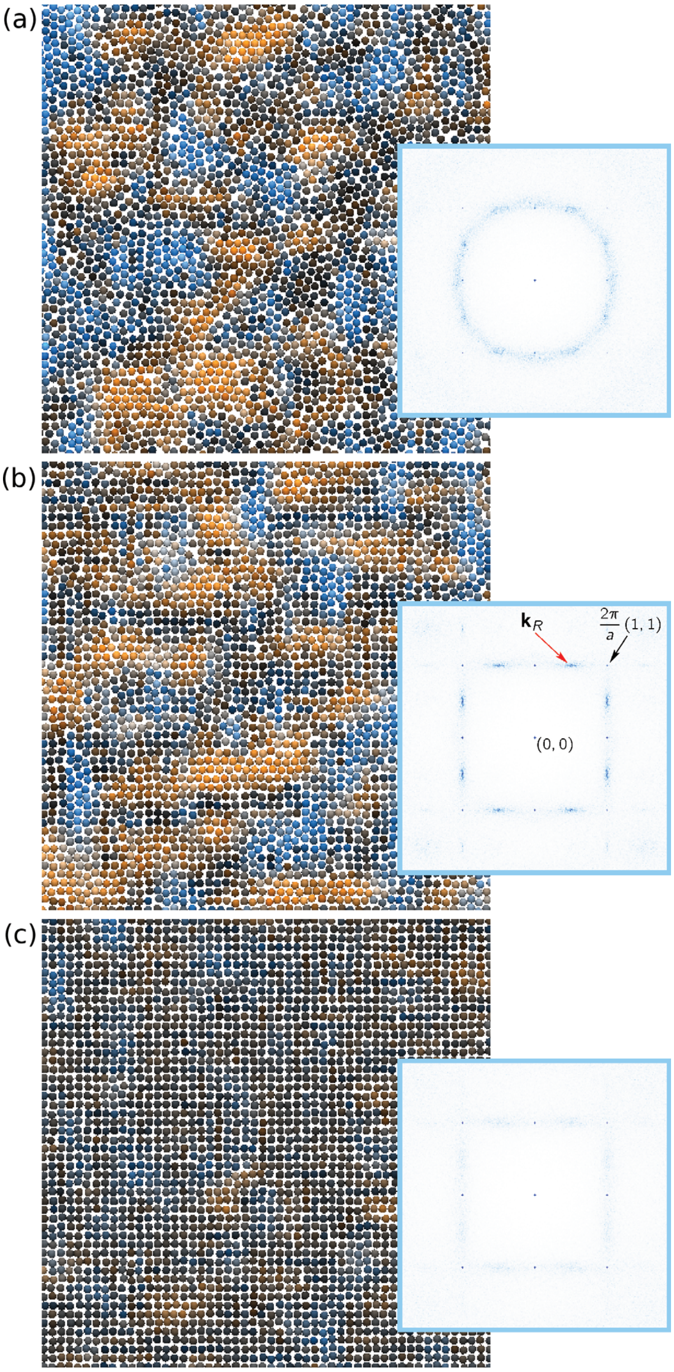

Figure 5.4: *Particle configurations from Monte Carlo simulations for a system with* 128^2 *particles (only a small section of the system is shown) and the corresponding scattering function (insets) for a packing fraction* $\eta = 0.69$ *and external field strength (a)* $V_0/k_BT = 1$, *(b)* 2 *and (c)* 4 *(indicated as stars in figure 5.2). The particles are colored according to their local structure: black denotes no rhombic order, orange and blue denote perfect rhombic order with rows along the* x*- and* y*-directions, respectively. The scattering peak at* $\mathbf{k}_R = (2\pi/a)\,(1,1/2)$ *due to the rhombic preordering is figured out in the inset of (b).*

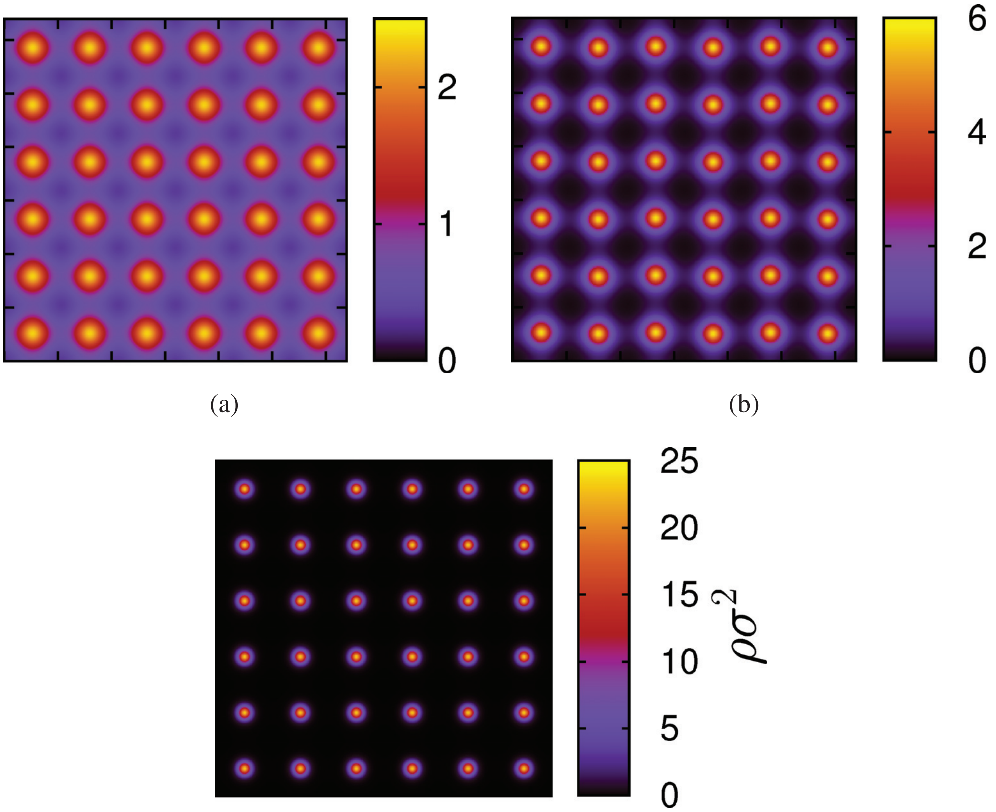

(a) (b)

(c)

Figure 5.5: *Density contour plots at the state points indicated by black stars in figure 5.2 in analogy to figure 5.4 illustrating a (a) square modulated fluid, (b) rhombic, and (c) strongly pinned square phase.*

a two-dimensional grid resulting in

$$S_{\text{inst}}(\mathbf{k}) = \frac{|\text{FT}(\rho_{\text{inst}})(\mathbf{k})|^2}{N}. \tag{5.21}$$

Thus, the peaks are slightly broadened, so that the four peaks at $\mathbf{k} = (2\pi/a)\,(\pm 1, \pm 1)$, which usually are point-like have a finite width. The scattering profile in figure 5.4(a) results from a more precise calculation of the average scattering function, given by

$$S(\mathbf{k}_R) = \frac{1}{N}\left\langle \left[\sum_{n=1}^{N} e^{i\mathbf{k}_R\cdot\mathbf{R}_n}\right]^2 \right\rangle. \tag{5.22}$$

This is averaged over many configurations obtained during the simulations and over different symmetry related vectors in reciprocal space $\mathbf{k}_R$.

In addition to the information about the position of each particle plotted in the snapshot

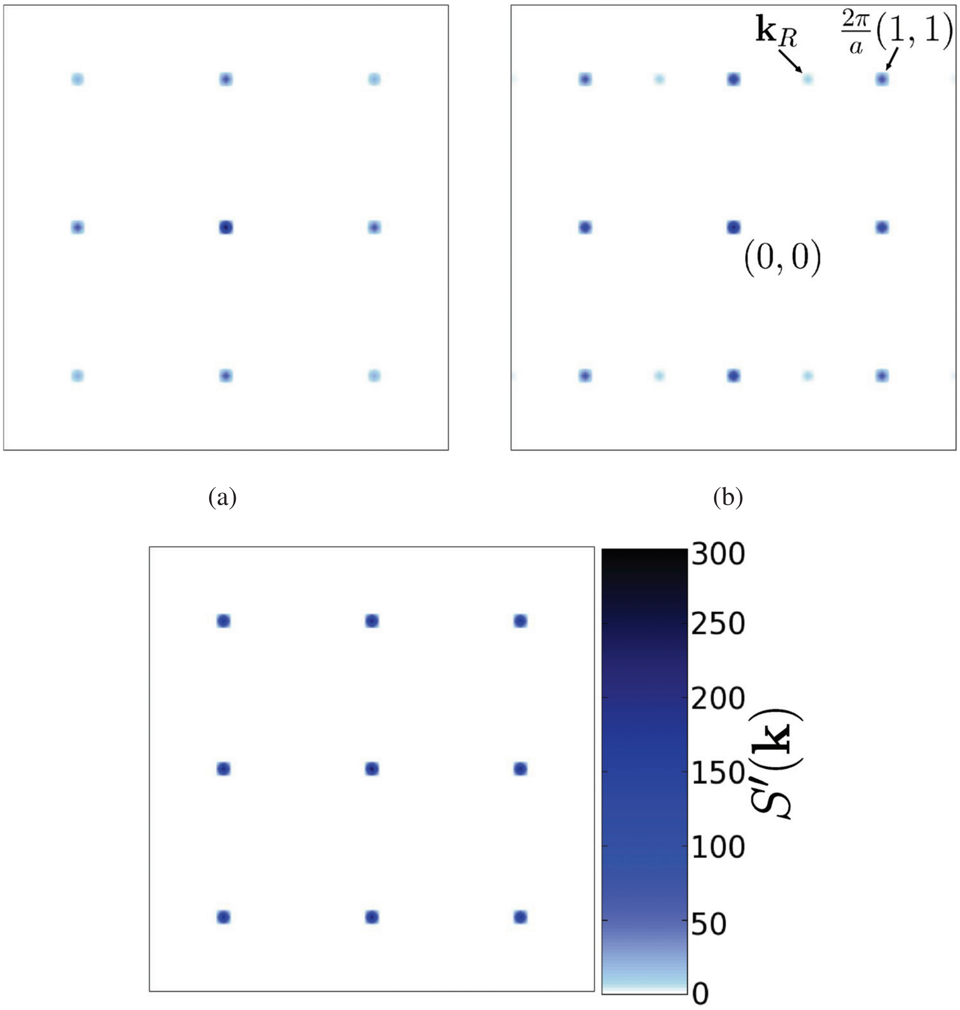

(a) (b)

(c)

Figure 5.6: $S'(\mathbf{k})$ *corresponding to the density profiles shown in figure 5.5.*

in figure 5.4, a color code is included which results from $S_x^{(R)}(i)$ and $S_y^{(R)}(i)$ defined by

$$S_x^{(R)}(i) \equiv \max_{\sigma=\pm 1} \frac{1}{N_i} \sum_j \cos\left(\frac{2\pi}{a}\left(\hat{x} + \sigma\frac{\hat{y}}{2}\right)[\mathbf{R}_j - \mathbf{R}_i]\right) \tag{5.23}$$

and $S_y^{(R)}(i)$, obtained by interchanging x and y in this definition. The sum over j is limited to the N_i particles that are in a square of width $5a$ centered around the position $\mathbf{R}_i$ of particle i.

A similar analysis can be performed from DFT results. Regarding the state points illustrated by black stars in figure 5.2, density profiles are calculated using DFT and shown in figure 5.5. For low packing fractions a modulated fluid with square symmetry is obtained

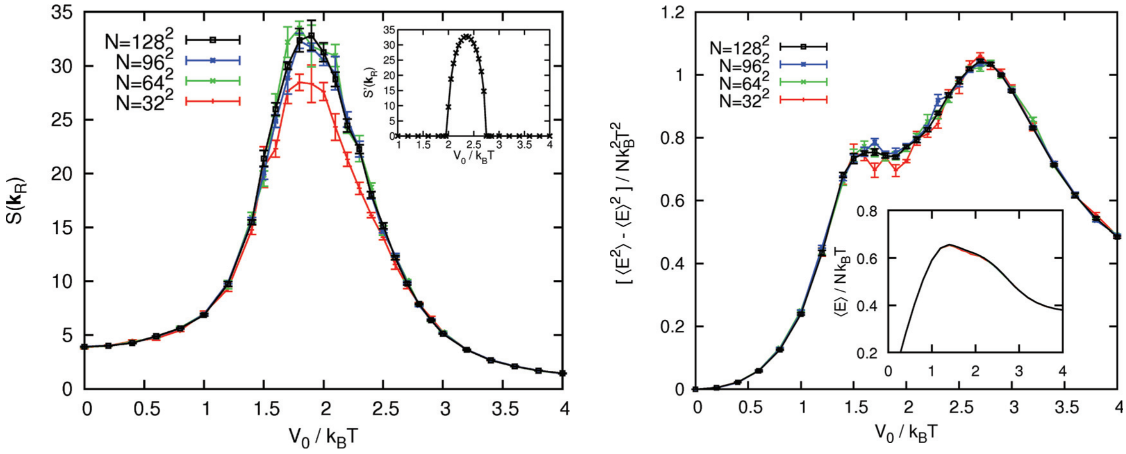

(a) (b)

Figure 5.7: *Monte Carlo simulation results for a fixed packing fraction* $\eta = 0.69$ *and varied system sizes* $N = 32^2$, 64^2, 96^2 *and* 128^2. *(a) The scattering function* $S(\mathbf{k})$ *at the* k*-vector that is indicative of rhombic order,* $\mathbf{k}_R \equiv 2\pi/a(1, 1/2)$, *is plotted as a function of the amplitude* V_0 *of the external field. The inset visualizes* $S'(\mathbf{k}_R)$ *from DFT. (b) The fluctuations of the energy divided by the system size* N *computed as a function of* V_0. *The inset shows the average energy per particle, for which the error is of order of the line thickness.*

(see figure 5.5(a)), whereas for high packing fractions the square phase is strongly pinned as visualized by very high peaks in figure 5.5(c). The intermediate profile (figure 5.5(b)) has a rhombic symmetry but the shift of the density peaks from the positions of the external potential is small.

Based on these profiles, a structure factor related quantity can be computed in analogy to equation (5.22). As DFT yields mean density profiles, it can be approximated using the Fourier transform of the mean density profile $\hat{\rho}(\mathbf{k})$ so that it reads

$$S'(\mathbf{k}) = \frac{|\hat{\rho}(\mathbf{k})|^2}{S_0}, \tag{5.24}$$

where the average and the Fourier transform are performed in opposite way compared with the definition in equation (5.22). The normalization factor $1/S_0$ results from a comparison with the simulation results and will be explained later. The obtained $S'(\mathbf{k})$ are shown in figure 5.6 revealing similar results as the MC simulations but the peaks are more localized. At low packing fractions (figure 5.6(a)), the peaks are smaller compared with those at high packing fractions (figure 5.6(c)). In the rhombic phase, additional peaks occur corresponding to the different symmetry between the existing peaks at $\mathbf{k} = \frac{2\pi}{a}(\pm 1, \pm 1)$. The simulation snapshot (figure 5.4(b)) consists of both possible directions of dislocation causing intermediate peaks at $\mathbf{k}_R = \frac{2\pi}{a}(\pm\frac{1}{2}, \pm 1)$ as well as $\mathbf{k}_R = \frac{2\pi}{a}(\pm 1, \pm\frac{1}{2})$. In contrast, density profiles obtained from DFT lack one of the directions and thus, there are intermediate peaks only at $\mathbf{k}_R = \frac{2\pi}{a}(\pm\frac{1}{2}, \pm 1)$ in the structure factor shown in figure 5.6(b).

From the scattering profiles it becomes clear that the peak height at position $\mathbf{k}_R$ holds as a good order parameter for a rhombic ordering. Thus, $S(\mathbf{k}_R)$ is calculated as a function of the amplitude of the external potential V_0 and shown in figure 5.7(a) for different system sizes and the inset illustrates the peak heights of $S'(\mathbf{k}_R)$ obtained from DFT. The DFT curve is normalized such that the peak height is similar to that calculated by the simulations and the resulting factor $1/S_0$ is used for all $S'(\mathbf{k})$. When the system size is larger than the largest rhombic cluster size occurring in the system ($N > 32^2$), no finite size dependence will occur in the scattering function which is an unambiguous sign of an exponential decay with distance of the rhombic positional order. However, in the regime where DFT predicts a stable rhombic phase, the structure factor $S(\mathbf{k}_R)$ is much larger what is equivalent to a larger rhombic order. Thus, phase transitions are expected at the values of the amplitude where $S(\mathbf{k}_R)$ changes most sharply. Accordingly, the averaged potential energy, as well as the mean squared energy fluctuations divided by the particle number N are plotted in figure 5.7(b). The first is discontinuous in case of a first order transition while the second would show a peak increasing with system size at a second order phase transition. As both cases do not occur, the transition is neither first nor second order but nevertheless, it has a clear structural signature. This is a very unusual type of transition but the reentrant behavior predicted by DFT is confirmed.

5.4 Conclusions

In conclusion, density functional theory calculations have been performed to study the phase behavior of hard disks on a substrate with square symmetry. A rhombic preordering was found and confirmed with Monte Carlo computer simulations. Hence, DFT is a suitable method to describe freezing on incommensurate structures. An analysis of the square to rhombic phase transition with DFT underestimated the order of the phase transition due to the mean-field type of DFT.

However, the presented results explain freezing on a substrate which has a structure that is incompatible with the symmetry of the bulk crystal of the examined hard disks. A new intermediate ordering was found which is a compromise between these two competing symmetries. In the examined model, the competition applies between square and hexagonal structure so that the new emerging phase has a rhombic symmetry. Nevertheless, this scenario can be anticipated to be a general one so that a comparable phase behavior is expected to occur also for other competing symmetries. It is not immediately self-evident how a possible preordering, corresponding to the rhombic phase presented in this chapter, might look like on substrates with other symmetries. Consequently, it is interesting to ask — on the basis of the results of this chapter — whether the intermediate phases shown for substrates with incompatible symmetries as for example the phases with 20-fold bond orientational order [188], or the Archimedean-like tiling phases [191, 194] on substrates with decagonal quasicrystalline symmetry, are reminiscent of a preordering before a first order transition. In addition, it would be interesting to study other model systems in which the boundaries induce the incompatibility of the symmetries [208–210], or where the incompatibility results from an incommensurate filling fraction of the substrate minima [182, 185], as well as to study the modification of friction due to the different phases [211].

CHAPTER 6

Crystal growth on patterned substrates

Results from this chapter have been published in paper [4] written jointly with Michael Schmiedeberg and Hartmut Löwen.

The novel material properties of ultrathin films carry the promise of fabricating technologically relevant optical switching devices, high-density information storage media and nanofilters with controlled porosity. In many cases, these films are crystalline monolayers which are grown on a patterned substrate acting as a template for solidification. Pivotal examples for these two-dimensional arrays range from sheets of graphene [212, 213] and organic molecules [214, 215] to soft matter films composed of nanoparticles [216, 217], proteins [218], polymers [219] or colloidal particles [184, 193, 195, 204, 220].

There are various techniques to prepare crystalline layers on a structured substrate. Using heteroepitaxy from the gas phase [221], crystalline islands are formed first on the substrate which then expand until they merge to a covering layer while exhibiting layer-by-layer growth into the direction perpendicular to the substrate at the same time. Crystals on a patterned substrate can also be grown out of the liquid phase where typically a layer-by-layer growth is obtained perpendicular to the wall [161, 204, 222–224]. A complementary technique uses self-assembly within the monolayer, e.g. by drying out the films [217, 220] or using electrophoretic deposition in the first place [225] which corresponds to a two-dimensional crystallization process.

In order to control and steer the formation of crystalline sheets on a template, a detailed understanding of the crystallization process on the scale of the individual particles is necessary. Colloidal suspensions are excellent model systems to study the crystallization process on the particle scale [226]. A structured substrate can be realized by superimposing optical laser fields [203] which constrain the colloidal particle to a modulated external potential and confine them to a two-dimensional layer [191, 227]. They thus offer the unique opportunity to observe the two-dimensional crystallization process in real-space.

In this chapter, the crystallization of a colloidal monolayer on a structured template starting from a few-particle nucleus, is explored. There is a crucial competition between the substrate structure and that of the growing crystal (typically hexagonal for spherical particles) which gives rise to a new crystal growth scenario. Unlike in crystal growth in the bulk [228] or on unstructured substrates [222] where a well-defined and connected crystal-fluid interface grows into the fluid possibly via faceting, branching or dendrite formation [229], a mechanism can be identified where a “compatibility wave” of the prescribed nucleus with the underlying substrate structure dictates the growth direction and efficiency. The compatibility wave describes the commensurability of the substrate structure with the stable hexagonal bulk crystal. Correspondingly, the growth process is strongly anisotropic and proceeds via transient island formation in front of an initial solid-fluid interface breaking the assumption of a well-defined single-connected interface topology. The concept of the compatibility wave is valid for a large variety of substrate structures, e.g. for a square-lattice and a quasicrystalline pattern.

Dynamical density functional theory is employed for colloidal hard spheres providing a microscopic approach to the crystallization process. The predictions arising from these numerical studies can be verified by performing experiments on confined colloids and they also have implications for molecular crystal growth on structured substrates. Finally, by quenching the transient emerging crystal during growth it might be possible to fabricate remarkable extended and hollow crystal structures with new possible technological applications.

6.1 System

As in the previous chapter, a system of hard disks of diameter σ is considered, positioned on a substrate with square symmetry. In figure 6.1(a), the system is presented in a schematic illustration. There is a nucleus consisting of hexagonally arranged disks with inter-particle distance a_Δ placed on the substrate with lattice constant a_V. The nucleus is rotated counter-clockwise by an angle ϕ with respect to a symmetry axis of the substrate and it is surrounded by a fluid which is modulated by the substrate potential. Figures 6.1(b)-(f) display a typical series of snapshots of the growth dynamics of the crystal. In contrast to the growth behavior in the bulk, there is no well-defined crystal-fluid interface growing, but instead the substrate potential influences the dynamics such that those regions which are matching better with the positions of the substrate minima grow earlier than the less compatible ones.

The substrate potential induces a modulation of the local density. When the nucleus is positioned on the substrate, the hexagonal symmetry of the nucleus causes a modulation which starts growing but differs from the symmetry of the substrate potential. The superposition of the two different patterns is called a compatibility wave that drives the growth process. The compatibility wave possesses maxima at the positions where the two patterns coincide.

In the sketch in figure 6.1(a), the color code indicates the distance of two neighboring peaks of the crystal lattice and the substrate minima. Thus, the compatibility regions are denoted by darker red spheres, while less compatible regions are lighter. The snapshots

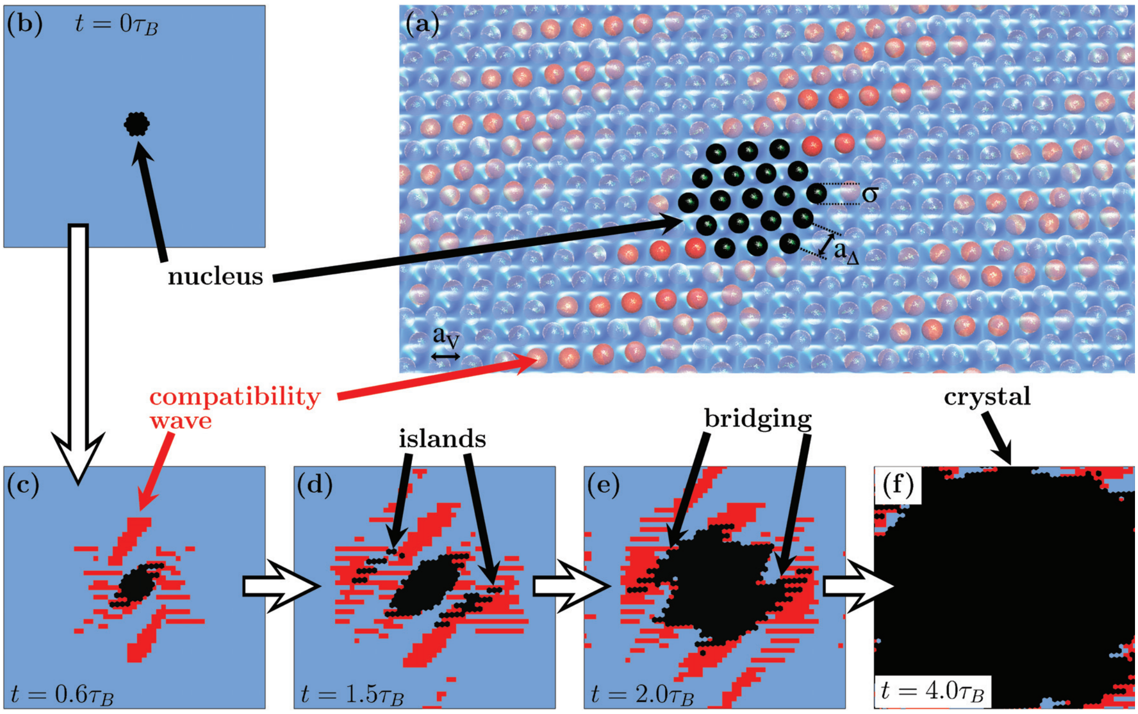

Figure 6.1: *(a) Schematic representation of a nucleus of hard disks with diameter σ located on a two-dimensional substrate with square symmetry rotated counterclockwise by an angle $\phi = 5^\circ$ relative to a symmetry direction of the substrate and lattice constant a_V. The snapshots (b)-(f) illustrate the growth of a spherical nucleus influenced by the substrate with amplitude $V_0 = 0.5k_BT$ at times (b) $t = 0$, (c) $t = 0.6\tau_\mathrm{B}$, (d) $t = 1.5\tau_\mathrm{B}$, (e) $t = 2\tau_\mathrm{B}$, and (f) $t = 4\tau_\mathrm{B}$, where τ_B is the Brownian time. Red regions display the compatibility wave and are defined by density peaks above a threshold value $\rho_\mathrm{th}\sigma^2 = 1.5061$. Black regions denote crystalline areas ($\rho_\mathrm{th}\sigma^2 = 2.0$), whereas blue regions remain fluid ($\rho_\mathrm{th}\sigma^2 \leq 1.5060$).*

illustrated in figures 6.1(c)-(f) denote the compatibility regions in red while crystalline regions are shown in black and fluid areas remain blue.

In correspondence to the static case (see equation (5.3)), the substrate potential $V_\mathrm{ext}(\mathbf{r})$ is given by

$$V_\mathrm{ext}(\mathbf{r}) = V_0 \left[1 - \frac{1}{4}\left(1 - \cos(k_x x)\right)\left(1 - \cos(k_y y)\right)\right], \tag{6.1}$$

with the components of the reciprocal lattice vector $\mathbf{k}$ given by $k_x = k_y = 2\pi/a_\mathrm{V}$ and the amplitude denoted with V_0. The latter is measured in units of the thermal energy k_BT, where T is the temperature and k_B is Boltzmann's constant. In the following, a fixed packing fraction $\eta = 0.74$ and an interaction strength $V_0 = 0.5k_BT$ is chosen which results in a hexagonal crystalline phase (see figure 5.2) under the constraint of a single particle per substrate minimum.

In order to obtain the initial nucleus, a density profile which is modulated by the substrate potential is used. For a short time of $0.07\tau_\mathrm{B}$ (τ_B is the Brownian time), an external pinning potential with Gaussian shape given by

$$V_{\mathrm{p}}(\mathbf{r}) = \sum_i V_{\mathrm{p}}^{(0)} e^{-\alpha(\mathbf{r}-\mathbf{r}_i)^2} \tag{6.2}$$

with a strong amplitude $V_{\mathrm{p}}^{(0)}/k_B T = 4$ and a width $\alpha\sigma^2 = 6$ is added to the external substrate potential so that the density peaks grow at the pinning positions $\mathbf{r}_i$. After this time, the pinning potential is switched off and the only remaining external potential is induced by the substrate pattern.

6.2 Dynamical Density Functional Theory

The dynamics of dispersed Brownian particles can be described by the use of dynamical density functional theory (DDFT). As explained in section 2.4, this theory is based on classical DFT [15, 18, 24, 33] and can be derived from the exact Smoluchowski equation [55, 56, 230]. Reformulating equation (2.80), the time-dependence of the density profiles $\rho(\mathbf{r}, t)$ can be written by using a generalized diffusion equation

$$\frac{\partial\rho(\mathbf{r},t)}{\partial t} = (k_B T)^{-1} D \nabla \cdot \left(\rho(\mathbf{r},t) \nabla \frac{\delta\Omega[T, A, \mu, \rho(\mathbf{r},t)]}{\delta\rho(\mathbf{r},t)} \right), \tag{6.3}$$

which contains the short time diffusion coefficient D. In analogy to all preceding chapters, the grand canonical free energy $\Omega(T, A, \mu, [\rho(\mathbf{r}, t)])$ depends on the temperature T, the area of the system A, and the chemical potential μ which is used as a Lagrangian multiplier to fix the average particle number in the system. Additionally, Ω is a functional of the time-dependent local density $\rho(\mathbf{r}, t)$. In the spirit of chapter 5, the grand canonical free energy can be separated into a sum of three different parts. There is a contribution of the ideal gas which reads

$$\mathcal{F}_{\mathrm{id}}[\rho(\mathbf{r})] = k_B T \int \mathrm{d}\mathbf{r}\rho(\mathbf{r}) \left[\ln\left(\Lambda^2 \rho(\mathbf{r})\right) - 1 \right], \tag{6.4}$$

including the (irrelevant) thermal wavelength Λ. A second contribution results from the interaction of particles with the external potential of equation (6.1) leading to

$$\mathcal{F}_{\mathrm{ext}}[\rho(\mathbf{r})] = \int \mathrm{d}\mathbf{r}\rho(\mathbf{r})[V_{\mathrm{ext}}(\mathbf{r}) - \mu]. \tag{6.5}$$

The third part — the excess free energy $\mathcal{F}_{\mathrm{exc}}[\rho(\mathbf{r})]$ — recovers the inter-particle interactions. For this part, a recently developed approach from fundamental measure theory [49] is used, as mentioned in chapter 2 and described in detail in section 5.2.

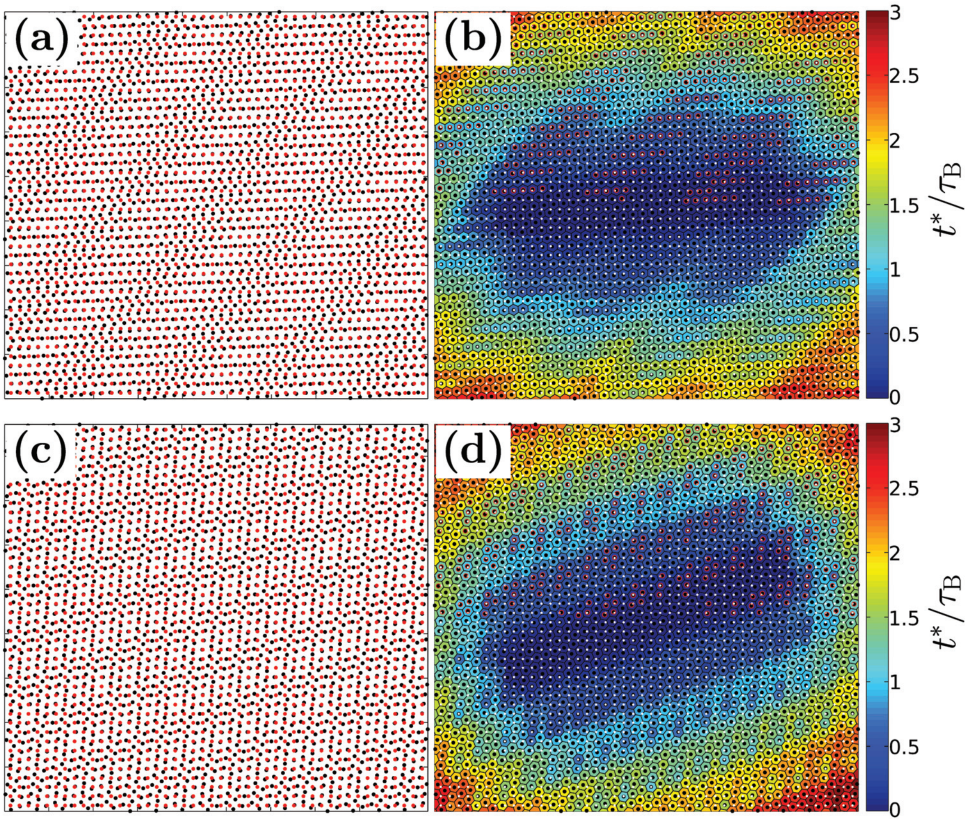

Figure 6.2: *A stripe of hard disks located on a square substrate at two different angles (a, b)* $\phi = 5^\circ$ *and (c, d)* $\phi = 20^\circ$*. The color code in (b, d) indicates the time* t^*/τ_B *at which the local density peak has reached a threshold value* $\rho_\mathrm{th}\sigma^2 = 1.75$*. The left plots (a) and (c) show the corresponding positions of the substrate minima (red) and the particle positions of the final crystal (black). From these, compatibility regions can be extracted by measuring the distances between the points of both patterns.*

6.3 Results

The nucleus shown in figure 6.1(a) has a curved surface and thus, the growth process is influenced by this curvature. In order to suppress this effect, in the following, a nucleus consisting of three rows of particles is considered and the growth is analyzed in the direction perpendicular to the elongation of the stripe. In analogy to the curved nucleus, compatibility regions result from a comparison of the positions of the substrate minima and the lattice sites at which the crystal is intended to grow. Depending on the angle of rotation ϕ, the patterns which result from overlaying the substrate minima and the crystal lattice sites differ. In figures 6.2(a) and (c), these patterns are shown for two different angles ϕ. At less dense regions, the two underlying symmetries match better so that at first glance, compatibility regions can be extracted. At smaller angles ϕ, the resulting pattern consists of broader and less frequent stripes (see figure 6.2(a)), while at larger angles, more stripes are visible which have merged compared to the smaller angle situation. Additionally, the orientation of the stripes differs when the rotation angle is varied. In figures 6.2(b) and (d), the time resolved growth of the initial nucleus is shown for the corresponding rotation angles. The color code indicates the time t^* in units of the Brownian time τ_{B} at which the local density value $\rho(\mathbf{r}, t)$ has passed a threshold value ρ_{th}. The growth dynamics are strongly coupled to the corresponding patterns shown in figures 6.2(a) and (c). The growth is anisotropic as islands not linked to the nucleus form in front of the crystal-fluid interface.

When the nucleus is positioned on the substrate, the inter-particle distance is given by a_Δ. Influenced by the substrate potential, the grown crystal is slightly distorted so that a modified lattice constant a'_Δ needs to be introduced in order to recover the correct symmetry of the resulting lattice.

Next, the growth behavior perpendicular to the elongation of the nucleus is analyzed quantitatively. As described previously, there are two competing length scales: the mean particle-particle distance of the grown hexagonal crystal a'_Δ on the one hand and the lattice constant of the substrate potential $\tilde{a}_{\mathrm{V}}$ measured in the direction of crystal growth on the other. In order to obtain the compatibility regions, the detune ratio $\tilde{a}_{\mathrm{V}}/a'_\Delta$ can be considered. Therefore, the difference between integer multiples of both of these two length scales $n\tilde{a}_{\mathrm{V}} - ma'_\Delta$ is calculated for several integer values $n, m \in \mathbb{N}$. The resulting difference varies for different integer values so that local minima for the detune ratio can be found. These minima predict the compatibility positions in the explored direction. In figure 6.3(a), the x-positions of the compatibility regions are shown for different detune ratios. In the limit of identical length scales $\tilde{a}_{\mathrm{V}}/a'_\Delta = 1$, all positions are compatible. For a very small detune, the first compatible region occurs at a very large distance x. By increasing the detune ratio further, the distance to the first compatible position decreases while all other compatible positions approach each other. Consequently, a larger detune ratio leads to a more frequent occurrence of compatibility regions but the effect of each single compatible region is expected to decrease. The growth shown in figure 6.2 is now analyzed quantitatively and the results are displayed in figures 6.3(b) and (c) for the corresponding angles of rotation ϕ. In order to calculate the detune ratio, the lattice constant of the substrate potential in the direction perpendicular to the elongation of the nucleus needs to be known. A simple geometric argument shows

$$\tilde{a}_{\mathrm{V}}(\phi) = \frac{a_{\mathrm{V}}}{\cos(\phi)}. \tag{6.6}$$

With this knowledge, the positions of best compatibility can be read off from figure 6.3(a) as the detune ratio is known and the prediction can be compared with the results of the DDFT calculations of the growth dynamics. DDFT yields a time-dependent local density $\rho(\mathbf{r}, t)$ which can be evaluated at the lattice sites of the grown crystal or more precisely at the positions in the direction of growth, perpendicular to the initial crystal-fluid interface. Similar to figure 6.2, a threshold value ρ_{th} is chosen and the critical time t^* at which this threshold density is reached is measured. The time values t^* for the considered system

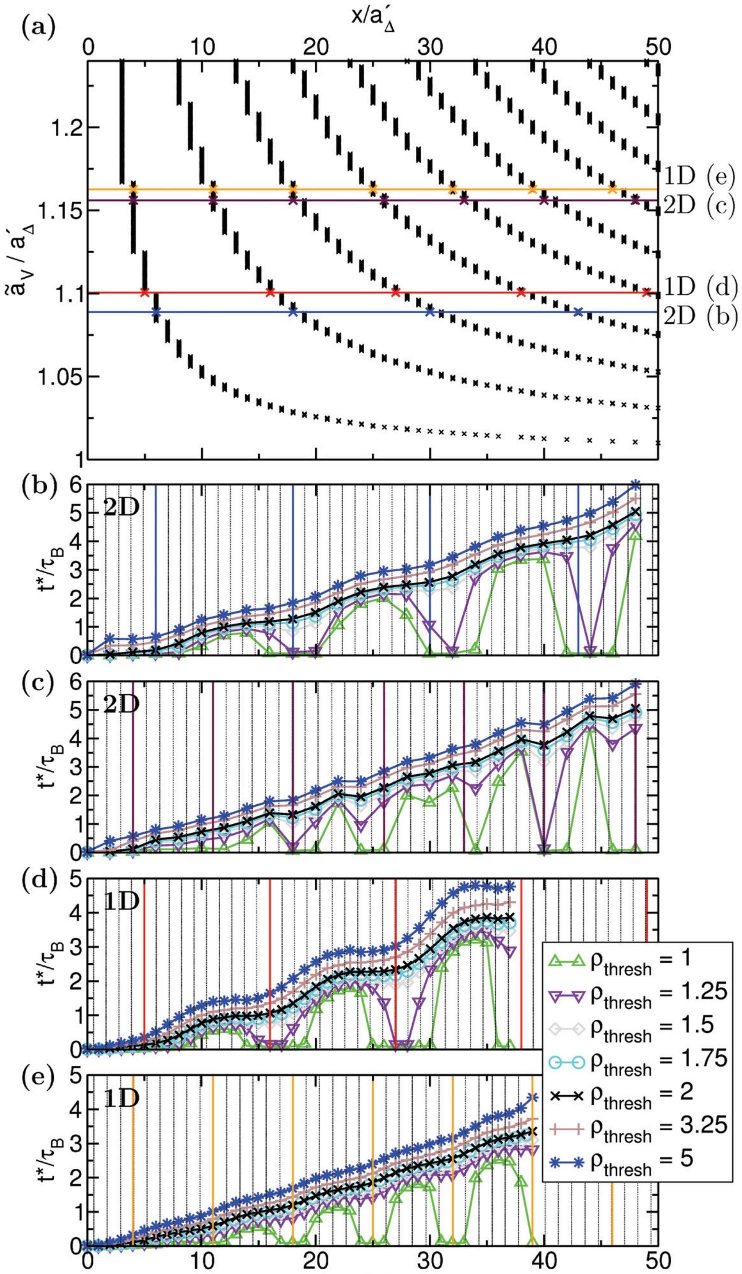

Figure 6.3: *Depending on the detune ratio of the lattice constants of the hexagonal crystal* a'_Δ *and of the substrate potential* $\tilde{a}_V$ *measured in the direction of growth, the discrete positions of best compatibility are plotted in (a). (b-e) Times* t^* *at which the local density peaks of a growing crystal exceeds a given threshold value* ρ_{th}*. The curves are obtained for a two-dimensional system (b, c) as well as for one-dimensional channels (d, e) as functions of the detune ratio* $\tilde{a}_V/a'_\Delta$*. Plots (b-e) are spatially normalized to the lattice constant of the hexagonal crystal* a'_Δ*, such that the best matching positions, indicated by colored vertical lines, can be obtained from (a).*

are shown in figures 6.3(b) and (c) while the latter corresponds to a larger angle ϕ. By comparing local dips in the curve with the occurrence of compatibility regions, a good agreement is obtained. For smaller values of ϕ, the anisotropy in the growth dynamics is more pronounced, caused by less dense compatible regions. At small values of ρ_{th}, very short times are sufficient for the local density to reach the threshold values at the proposed compatibility regions. Here, the modulation due to the external potential already causes this effect. For a sufficiently large threshold value, the effect of the square modulation is neglected, so that the actual growth is recovered in the critical times t^*. The slope of the curves which corresponds to an inverse speed of growth is related to the compatibility regions as these locally speed up the growth. Still, the effect is more pronounced for smaller detune ratios (see figure 6.3(b)).

In a next step, the growth is analyzed in an effectively one-dimensional channel. In this case, the substrate potential is simplified to a one-dimensional cosine-wave which varies in the regarded direction and is given by

$$V_{\mathrm{ext}}(x) = \frac{V_0}{2}\Big(1 + \cos(k_x x)\Big), \tag{6.7}$$

with the lattice constant a_{V} included in the reciprocal lattice vector $k_x = 2\pi/a_{\mathrm{V}}$ and the amplitude V_0. The time-resolved growth is computed for similar packing fractions η and detune ratios $a_{\mathrm{V}}/a'_{\Delta}$ and the obtained results are presented in figures 6.3(d) and (e). In the two-dimensional case, the substrate affects the growth not only in the examined direction but also perpendicular to it. Naturally, the one-dimensional case lacks the perpendicular effect and thus, compared with the corresponding 2D plot, the shape of the curves is smoother. Still, regions of higher compatibility coincide with dips in the critical times t^* revealing the compatibility wave as these regions preferentially grow earlier than those of lower compatibility.

Furthermore, the growth scenario with a compatibility wave is expected to be important for a variety of other substrate symmetries when the length scales which indicate the substrate are incommensurate with the length scale given by the hexagonal nucleus. Thus, it is sufficient to know the detune ratio in order to predict the dynamics of growth when a hexagonal nucleus is positioned on a patterned substrate with any symmetry. In the following, three different substrate symmetries are analyzed to corroborate this expectation. In figure 6.4(a), a substrate with hexagonal symmetry is depicted, so that the superstructure of the two existing patterns has a six-fold symmetry which is slightly rotated in analogy to the rotation of the nucleus. The same symmetry occurs for a honeycomb lattice as it is presented in figure 6.4(c). A different superstructure occurs for a quasicrystalline substrate as shown in figure 6.4(e). The underlying quasicrystalline pattern consists of squares and triangles (see, e.g., [231]). It possesses two incommensurate length scales per direction (other quasicrystals posses even more length scales), so that the compatibility regions are no longer periodic. In this case, the compatibility regions are given by the length scale resulting from the growing crystal and one length scale of the quasicrystalline substrate. Thus, the pattern shown in figure 6.4(e) has a six-fold symmetry. Due to the second

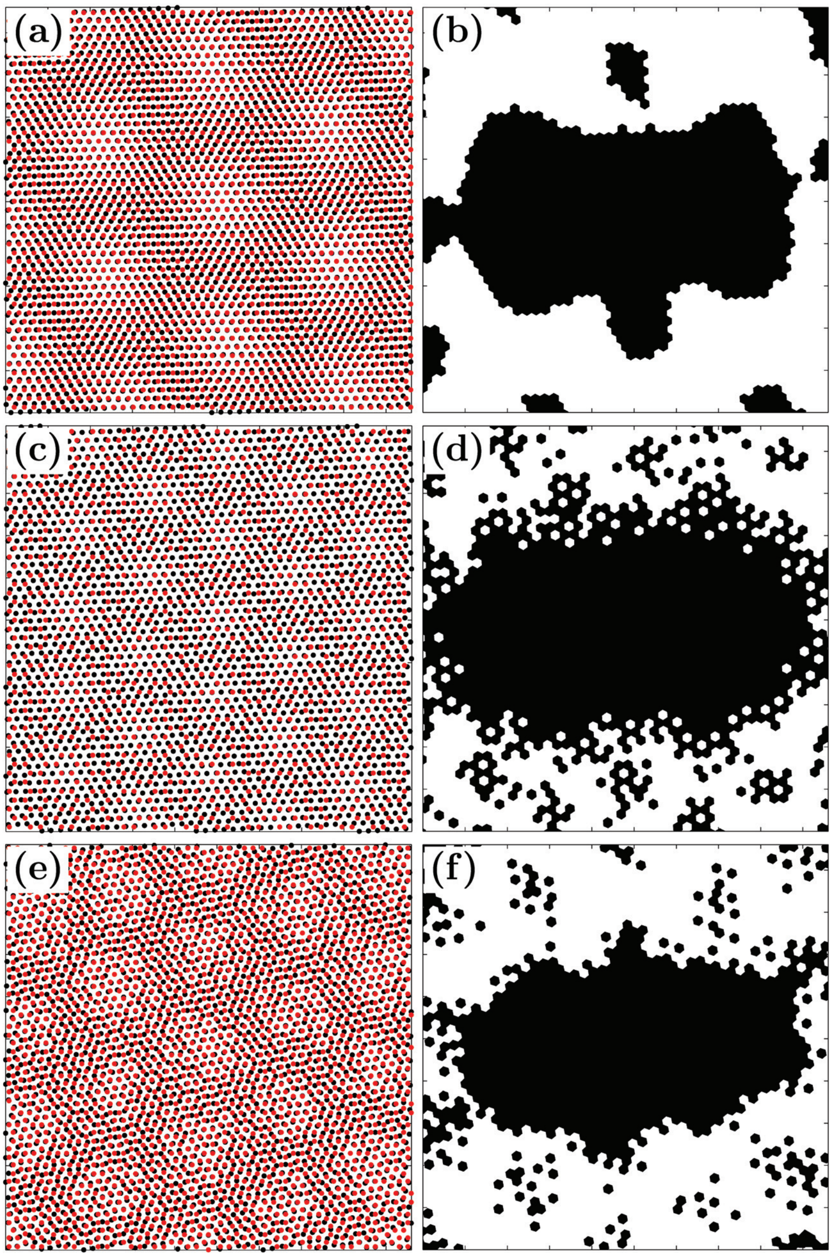

Figure 6.4: *Superposition of a hexagonal lattice and the minima of a substrate potential with (a) triangular, (c) honeycomb, (e) twelve-fold quasicrystalline symmetry. The detune ratio* $a_{\mathrm{V}}/a'_{\Delta}$*, as well as the rotation angle of the hexagonal lattice, are varied leading to three different combinations: (a)* $a_{\mathrm{V}}/a'_{\Delta} = 1.05$*,* $\phi = 2°$*, (c)* $a_{\mathrm{V}}/a'_{\Delta} = 1.1$*,* $\phi = 3°$*, and (e)* $a_{\mathrm{V}}/a'_{\Delta} = 1.0$*,* $\phi = 10°$*. The quasicrystalline pattern is given by a square-triangle tiling (see, e.g., [231]). (b, d, f) Snapshots of the growth of an initial stripe on the corresponding substrate potential with threshold values (b)* $\rho_{\mathrm{th}}\sigma^2 = 1.1$*, (d)* $\rho_{\mathrm{th}}\sigma^2 = 1.0$*, and (f)* $\rho_{\mathrm{th}}\sigma^2 = 1.35$ *at time* $t = 0.5\tau_{\mathrm{B}}$*. The system parameters in (b, f) are packing fraction* $\eta = 0.73$*, and interaction strength* $V_0 = 0.1k_BT$ *while in (d) the interaction strength is* $V_0 = 0.2k_BT$*.*

length scale of the substrate, all compatible regions differ in structure.

For all of the three cases, the growth of a nucleus with stripe symmetry is regarded and snapshots are displayed in the corresponding figures 6.4(b), (d), and (f). Regions with density peaks above the threshold density ρ_{th} are covered in black, while regions with local densities below the threshold are shown in white. The black areas not belonging to the crystal coincide with the predicted compatible regions in all three cases. Thus, it can be inferred that this behavior can be expected for other kinds of substrate potentials. Here, the mechanism of crystal growth will be predicted by the compatibility wave which dictates the direction as well as the efficiency of growth.

6.4 Conclusions

In conclusion, in this chapter, the dynamics of growth have been examined for a nucleus of hard particles positioned on a patterned substrate. There are two incommensurate length scales competing in the system — one length scale given by the hexagonal crystal which is about to grow, and a second one induced by the substrate symmetry. Due to this, no well-defined and connected crystal-fluid interface can be obtained. In contrast, the growth is dictated by a compatibility wave which is a superposition of the two competing symmetries. The same scenario can be applied to growth on more complex substrate patterns. Here, the only relevant parameter to predict the structure of the compatibility regions is the detune ratio of the two length scales occurring.

A possible application of the compatibility wave concept is that a crystal is grown and impurities are confined at positions predefined by the compatibility regions. As islands form before the crystal-fluid interface, impurities can be locally trapped instead of being pushed in front of the interface. As a second application, it can be possible to deduce the structure and the properties of the initial nucleus from the occurrence of the compatibility regions and the positions of the islands.

Furthermore, the growth behavior of a nucleus on a patterned substrate in a three-dimensional system may be strongly related to the presented 2D results. Therefore, compatibility waves are important for a large number of systems where crystal growth on substrates with detuned length scales is studied. Consequently, the growth via a compatibility wave is a more suitable description than any other scenario which requires a connected interface between the fluid and the crystalline phase.

Summary

In physics, there are three different ways of examining a system - experiment, simulation, and theory. This thesis focuses on the theory of colloidal systems, but also simulations are performed to corroborate the theoretical predictions. The analysis of all different kinds of systems studied in this thesis is based on (dynamical) density functional theory – (D)DFT. Neither the classical nor the dynamical DFT describe the positions of particles in the system, but all occurring configurations are averaged resulting in a mean density field which relates to the probability of particles to be located at specific positions. With DFT the energetically favored state of a system can be computed while DDFT yields a time-resolved analysis of the Brownian particles.

In this thesis, spherical colloids are studied affected by various external fields. The simplest model for spherical colloids are hard spheres, which can be compared to billiard balls, as they do not interact except for the case of contact. An overlap of two hard spheres is forbidden. Polymers, which are modeled as spherical particles, can be added to a suspension of hard spheres so that an effective attraction of the spherical colloids is caused. This leads to different bulk phases compared with the pure hard-sphere system. Additionally, a static external periodic field is induced, so that a so called zebra phase can occur where slabs of colloid-rich and colloid-poor regions alternate. This exposes an untypical type of critical behavior which results from additional “hidden” interfaces within a single slab instead of just interfaces between two slabs.

Influenced by gravity, a binary mixture of repulsive spherical colloids is examined either in a static or a shaken box. In analogy to granular matter, a situation can be found when heavier particles on average float on top of lighter particles. This so called brazil-nut effect is known from everyday life as it also occurs in mixtures of cereals, where a shaking leads to a lift of heavier berries out of the mixture of smaller grains. In this thesis, the occurence of this effect is studied in a colloidal system depending on the system parameters as the static as well as the dynamic case yield a colloidal brazil-nut effect.

Furthermore, hard disks – the 2D-projection of hard spheres – are considered on a patterned square substrate. In equilibrium, there is a competition between the triangular phase favored by the particles and the square symmetry induced by the substrate. This leads to a rhombic preordering of the disks before they form a crystalline phase. With the knowledge of the equilibrium phase diagram, growth dynamics are studied, when a triangular few-particle nucleus is placed on the substrate. Due to the competing symmetries, the growth proceeds via transient island formation without a well-defined crystal-fluid interface and the direction and efficiency is dictated by a compatibility wave.

Summing up, this thesis justifies that density functional theory is a suitable method to study several systems of spherical colloids with different interaction potentials influenced by external fields of various kinds and symmetries — both in a fluid and a crystalline phase.

Zusammenfassung

Um physikalische Systeme zu untersuchen gibt es drei Methoden - Experiment, Simulation und Theorie. Diese Dissertation legt den Schwerpunkt auf die Theorie von weicher Materie, jedoch werden auch Simulationsergebnisse dargestellt um die theoretischen Vorhersagen zu untermauern. Die Analyse aller in dieser Arbeit untersuchten Systeme basiert auf (dynamischer) Dichtefunktionaltheorie – (D)DFT. Weder die klassische, noch die dynamische DFT beschreiben die Positionen der einzelnen Teilchen im System. Stattdessen wird über alle möglichen Konfigurationen gemittelt. Daraus resultiert ein mittleres Dichtefeld, welches die Wahrscheinlichkeit angibt, ein Teilchen an einer bestimmten Position zu detektieren. Mit Hilfe von DFT kann der energetisch günstigste Zustand eines Systems berechnet werden. Die DDFT beschreibt die zeit-aufgelöste Bewegung der dispergierten Brownschen Teilchen.

In dieser Dissertation werden kugelförmige Kolloide unter dem Einfluss verschiedener externer Feldern untersucht. Das einfachste Modell-System sind harte Kugeln, vergleichbar mit Billardkugeln, da sie ausser im Falle des Kontaktes nicht wechselwirken. Ein Überlapp zweier Kugeln ist nicht möglich. Durch die Zugabe von Polymeren, im Modell als kugelförmige Teilchen beschrieben, zu einer Lösung harter kugelförmiger Kolloide kann aufgrund von Entropie eine kurzreichweitige effektive Anziehungskraft zwischen den Kolloiden erzeugt werden. Daraus resultieren andere Gleichgewichts-Phasen als in einem System ohne Polymere. Wird von aussen ein statisches periodisches Feld induziert, kann sich eine so genannte Zebra-Phase bilden. Diese ist durch Streifen charakterisiert, die abwechselnd aus vielen und wenigen Kolloiden bestehen. Zusätlich zu gewöhnlichen Grenzflächen zwischen kolloidreichen und kolloidarmen Bereichen gibt es Grenzflächen innerhalb der Streifen, die zu einem untypischen kritischen Verhalten führen.

Unter dem Einfluss von Gravitation wird eine binäre Mischung von repulsiven kugelförmigen Kolloiden sowohl in einer unbewegten als auch in einer geschüttelten Box untersucht. In Analogie zu granularen Systemen, kann ein Zustand gefunden werden, bei dem im Mittel schwerere Teilchen oberhalb von leichteren Teilchen angeordnet sind. Dieser so genannte Paranuss-Effekt tritt auch in Müsli-Packungen auf. Wird eine Müsli-Tüte geschüttelt, können die großen Beeren nach oben transportiert werden, obwohl sie schwerer sind als die kleinen Körner. In dieser Dissertation, wird untersucht unter welchen Bedingungen dieser Effekt in einem kolloidalen System beobachtet werden kann, da er sowohl im statischen als auch im dynamischen Fall auftritt.

Zusätzlich werden harte Scheiben – die Projektion von harten Kugeln auf zwei Dimensionen – auf strukturierten Substraten untersucht. Im Gleichgewicht gibt es einen Wettstreit zwischen der Dreiecksphase, in der sich kugelförmige Teilchen bevorzugt anordnen, und der Quadratsymmetrie, welche das Substrat induziert. Dies führt zu einer rhombischen Vorordnung der Scheiben bevor sich eine kristalline Dreiecksphase bildet. Auf dem Gleichgewichts-Phasendiagramm aufbauend kann auch die Wachstums-Dynamik in diesem System untersucht werden, wenn ein Keim mit dreieckiger Struktur auf dem Substrat platziert wird. Der Kristall wächst dann in die umgebene flüssige Phase indem sich kurzzeitig Inseln bilden. Folglich kann keine klare Grenzfläche zwischen Kristall und Flüssigkeit definiert werden. Die Richtung als auch die Effizienz des Wachstums werden dabei durch eine Kompatibilitätswelle bestimmt.

Zusammenfassend untermauert diese Dissertation, dass Dichtefunktionaltheorie eine sinnvolle Methode ist um verschiedene Systeme kugelförmiger Kolloide unterschiedlichster Wechselwirkungen unter dem Einfluss von mannigfaltigen externen Feldern zu untersuchen, sowohl in der Flüssigkeit als auch im Kristall.

Danksagung

An dieser Stelle möchte ich mich noch bei einigen Menschen bedanken, die mir während meiner Promotionszeit geholfen haben.

Als erstes danke ich meinem Betreuer Prof. Hartmut Löwen dass ich mit ihm zusammen arbeiten konnte, sein immer offenes Ohr, auch in stressigen Zeiten, und die vielen guten Ratschläge und interessanten Geschichten. Ebenso danke ich Prof. Stefan Egelhaaf dafür, dass er die Zweitkorrektur dieser Arbeit übernommen hat.

Ich danke Michael Schmiedeberg, der mich vor allem in der zweiten Hälfte meiner Promotion immer unterstützt und somit viele gute Resultate ermöglicht hat. Zusätzlich danke ich Richard Vink, Tobias Kruppa, René Messina und Matthieu Marechal für die erfolgreiche Kooperation und die guten Gespräche, Tobias und Matthieu auch für das Korrekturlesen dieser Arbeit.

Ein großer Dank geht an diejenigen, mit deren Hilfe viele Probleme einfach wurden. Hier sollen vor allem Ronald Blaak, Robert Evans, Andreas Härtel, Götz Lehmann, Martin Oettel und Adam Wysocki erwähnt werden, sowie meine Kollegen am Lehstuhl für Theoretische Physik II.

Einen wesentlichen Beitrag zum Erstellen dieser Arbeit haben die freundlichen Korrekturleser, Jörg Bewerunge, Kevin Mutch, Torben Ott, Brigitte Schumann und Urs Zimmermann, geleistet. Ohne ihre Hilfe wären vermutlich etlich mehr Fehler in dieser Arbeit übrig geblieben. Vielen Dank dafür!

Natürlich geht ein großer Dank an meine Freunde und Familie, die nie meiner ewigen Erklärungen und Erzählungen über Physik müssig wurden, mich unterstützt haben und zumindest stets so taten als interessiere sie das alles.

Ebenso danke ich noch allen, die hier namentlich unerwähnt bleiben, die aber auf die eine oder andere Weise zum erfolgreichen Gelingen meiner Promotion beigetragen haben.

Als letztes danke ich dir, Jessica, für die bedingungslose Unterstützung und jeden einzelnen Tag mit dir.

Bibliography

[1] R. L. C. Vink, T. Neuhaus, and H. Löwen. Fluid phase separation inside a static periodic field: An effectively two-dimensional critical phenomenon. J. Chem. Phys. **134**, 204907 (2011).

[2] T. Kruppa, T. Neuhaus, R. Messina, and H. Löwen. Soft repulsive mixtures under gravity: Brazil-nut effect, depletion bubbles, boundary layering, nonequilibrium shaking. J. Chem. Phys. **136**, 134106 (2012).

[3] T. Neuhaus, M. Marechal, M. Schmiedeberg, and H. Löwen. Rhombic preordering on a square substrate. Phys. Rev. Lett. **110**, 118301 (2013).

[4] T. Neuhaus, M. Schmiedeberg, and H. Löwen. Compatibility waves drive crystal growth on patterned substrates. submitted to New J. Phys. , (2013).

[5] P.-G. de Gennes. *Nobel Lecture: Soft Matter* (World Scientific Publishing Co., Singapore, 1997).

[6] R. A. L. Jones. *Soft Condensed Matter* (Oxford University Press, 2002).

[7] P. N. Pusey and W. van Megen. Phase behaviour of concentrated suspensions of nearly hard colloidal spheres. Nature **320**, 340 (1986).

[8] H. Löwen. Colloidal soft matter under external control. J. Phys. **13**, R415 (2001).

[9] S. Asakura and F. Oosawa. On interaction between two bodies immersed in a solution of macromolecules. J. Chem. Phys. **22**, 1255 (1954).

[10] S. Asakura and F. Oosawa. Interaction between particles suspended in solutions of macromolecules. J. Polym. Sci. **33**, 183 (1958).

[11] A. Vrij. Polymers at interfaces and the interactions in colloidal dispersions. Pure Appl. Chem. **48**, 471 (1976).

[12] M. Dijkstra, J. M. Brader, and R. Evans. Phase behaviour and structure of model colloid-polymer mixtures. J. Phys. **11**, 10079 (1999).

[13] M. Schmidt, H. Löwen, J. M. Brader, and R. Evans. Density functional for a model colloid-polymer mixture. Phys. Rev. Lett. **85**, 1934 (2000).

[14] I. O. Götze, J. M. Brader, M. Schmidt, and H. Löwen. Laser-induced condensation in colloid-polymer mixtures. Mol. Phys. **101**, 1651 (2003).

[15] R. Roth. Fundamental measure theory for hard-sphere mixtures: a review. J. Phys. **22**, 063102 (2010).

[16] P. Hohenberg and W. Kohn. Inhomogeneous electron gas. Phys. Rev. **136**, B864 (1964).

[17] W. Kohn. *Nobel Lecture: Electronic Structure of Matter - Wave Functions and Density Functionals* (World Scientific Publishing Co., Singapore, 2003).

[18] R. Evans. The nature of the liquid-vapour interface and other topics in the statistical mechanics of non-uniform, classical fluids. Adv. Phys. **28**, 143 (1979).

[19] J. C. Maxwell. On the dynamical theory of gases. Philos. Trans. Roy. Soc. London **157**, pp. 49 (1867).

[20] L. Boltzmann. *Weiter Studien über das Wärmegleichgewicht unter Gasmolekülen* (Sitzungsberichte Akad. Wiss. Wien 66:275, 1872; English transl.: S. G. Brush, *Kinetic theory*, Vol. 2, Irreversible Processes, 88-175, 1966). bib: phy a530.

[21] J. Gibbs, H. Bumstead, and R. van Name. *Scientific Papers of J. Willard Gibbs - Volume One: Thermodynamics* (Longmans, Green and Company, 1906).

[22] J.-L. Barrat and J.-P. Hansen. *Basic concepts for simple and complex liquids* (Cambridge Univ. Press., 2003).

[23] J.-P. Hansen and I. McDonald. *Theory of simple liquids* (Elsevier, 2006).

[24] P. Tarazona, J. A. Cuesta, and Y. Martinez-Raton. Density functional theories of hard particle systems. Lect. Notes Phys. **753**, 247 (2008).

[25] J. F. Lutsko. Recent developments in classical density functional theory. Adv. Chem. Phys. **144**, 1 (2010).

[26] R. Evans. Density functional theory for inhomogeneous fluids i. in *Lectures at 3rd Warsaw School of Statistical Physics, Kazimierz Dolny*, (2009).

[27] H. Löwen. Density functional theory for inhomogeneous fluids ii. in *Lectures at 3rd Warsaw School of Statistical Physics, Kazimierz Dolny*, (2009).

[28] N. D. Mermin. Thermal properties of the inhomogeneous electron gas. Phys. Rev. **137**, A1441 (1965).

[29] C. Ebner, W. F. Saam, and D. Stroud. Density-functional theory of simple classical fluids. i. surfaces. Phys. Rev. A **14**, 2264 (1976).

[30] J. K. Percus. Equilibrium state of a classical fluid of hard rods in an external field. J. Stat. Phys. **15**, 505 (1976). 10.1007/BF01020803.

[31] T. V. Ramakrishnan and M. Yussouff. First-principles order-parameter theory of freezing. Phys. Rev. B **19**, 2775 (1979).

[32] A. D. J. Haymet and D. W. Oxtoby. A molecular theory for the solid–liquid interface. J. Chem. Phys. **74**, 2559 (1981).

[33] Y. Rosenfeld. Free-energy model for the inhomogeneous hard-sphere fluid mixture and density-functional theory of freezing. Phys. Rev. Lett. **63**, 980 (1989).

[34] F. W. Olver, D. W. Lozier, R. F. Boisvert, and C. W. Clark. *NIST Handbook of Mathematical Functions* (Cambridge University Press, New York, NY, USA, 2010).

[35] E. Kierlik and M. L. Rosinberg. Free-energy density functional for the inhomogeneous hard-sphere fluid: Application to interfacial adsorption. Phys. Rev. A **42**, 3382 (1990).

[36] S. Phan, E. Kierlik, M. L. Rosinberg, B. Bildstein, and G. Kahl. Equivalence of two free-energy models for the inhomogeneous hard-sphere fluid. Phys. Rev. E **48**, 618 (1993).

[37] Y. Rosenfeld, M. Schmidt, H. Löwen, and P. Tarazona. Dimensional crossover and the freezing transition in density functional theory. J. Phys. **8**, L577 (1996).

[38] Y. Rosenfeld, M. Schmidt, H. Löwen, and P. Tarazona. Fundamental-measure free-energy density functional for hard spheres: Dimensional crossover and freezing. Phys. Rev. E **55**, 4245 (1997).

[39] P. Tarazona and Y. Rosenfeld. From zero-dimension cavities to free-energy functionals for hard disks and hard spheres. Phys. Rev. E **55**, R4873 (1997).

[40] P. Tarazona. Density functional for hard sphere crystals: A fundamental measure approach. Phys. Rev. Lett. **84**, 694 (2000).

[41] R. Roth, R. Evans, A. Lang, and G. Kahl. Fundamental measure theory for hard-sphere mixtures revisited: the white bear version. J. Phys. **14**, 12063 (2002).

[42] H. Hansen-Goos and R. Roth. Density functional theory for hard-sphere mixtures: the white bear version mark ii. J. Phys. **18**, 8413 (2006).

[43] H. Hansen-Goos and R. Roth. A new generalization of the carnahan-starling equation of state to additive mixtures of hard spheres. J. Chem. Phys. **124**, 154506 (2006).

[44] A. Härtel, M. Oettel, R. E. Rozas, S. U. Egelhaaf, J. Horbach, and H. Löwen. Tension and stiffness of the hard sphere crystal-fluid interface. Phys. Rev. Lett. **108**, 226101 (2012).

[45] E. Kierlik and M. L. Rosinberg. Density-functional theory for inhomogeneous fluids: Adsorption of binary mixtures. Phys. Rev. A **44**, 5025 (1991).

[46] Y. Rosenfeld. Free energy model for inhomogeneous fluid mixtures: Yukawa-charged hard spheres, general interactions, and plasmas. J. Chem. Phys. **98**, 8126 (1993).

[47] H. Hansen-Goos and K. Mecke. Fundamental measure theory for inhomogeneous fluids of nonspherical hard particles. Phys. Rev. Lett. **102**, 018302 (2009).

[48] H. Hansen-Goos and K. Mecke. Tensorial density functional theory for non-spherical hard-body fluids. J. Phys. **22**, 364107 (2010).

[49] R. Roth, K. Mecke, and M. Oettel. Communication: Fundamental measure theory for hard disks: Fluid and solid. J. Chem. Phys. **136**, 081101 (2012).

[50] C. Caccamo, J.-P. Hansen, and G. Stell. *NATO Science Series C: Mathematical and Physical Science 529: New Approaches to Problems in Liquid State Theory Inhomogeneities and Phase Separation in Simple, Complex and Quantum Fluids*, volume 529 of *NATO Science Series C: (closed)*, (1998).

[51] M. Schmidt, H. Löwen, J. M. Brader, and R. Evans. Density functional theory for a model colloid-polymer mixture: bulk fluid phases. J. Phys. **14**, 9353 (2002).

[52] D. Henderson, F. F. Abraham, and J. A. Barker. The ornstein-zernike equation for a fluid in contact with a surface. Mol. Phys. **31**, 1291 (1976).

[53] M. M. Telo Da Gama and R. Evans. The density profile and surface tension of a lennard-jones fluid from a generalized van der waals theory. Mol. Phys. **38**, 367 (1979).

[54] J. W. Cahn. Phase separation by spinodal decomposition in isotropic systems. J. Chem. Phys. **42**, 93 (1965).

[55] U. M. B. Marconi and P. Tarazona. Dynamic density functional theory of fluids. J. Chem. Phys. **110**, 8032 (1999).

[56] A. J. Archer and R. Evans. Dynamical density functional theory and its application to spinodal decomposition. J. Chem. Phys. **121**, 4246 (2004).

[57] J. M. Brader, R. Evans, and M. Schmidt. Statistical mechanics of inhomogeneous model colloid-polymer mixtures. Mol. Phys. **101**, 3349 (2003).

[58] H. N. W. Lekkerkerker, W. C. K. Poon, P. N. Pusey, A. Stroobants, and P. B. Warren. Phase behaviour of colloid + polymer mixtures. Europhys. Lett. **20**, 559 (1992).

[59] W. C. K. Poon. The physics of a model colloid-polymer mixture. J. Phys. **14**, R859 (2002).

[60] R. Tuinier, P. A. Smith, W. C. K. Poon, S. U. Egelhaaf, D. G. A. L. Aarts, H. N. W. Lekkerkerker, and G. J. Fleer. Phase diagram for a mixture of colloids and polymers with equal size. Europhys. Lett. **82**, 68002 (2008).

[61] P. G. Bolhuis, A. A. Louis, and J.-P. Hansen. Influence of polymer-excluded volume on the phase-behavior of colloid-polymer mixtures. Phys. Rev. Lett. **89**, 128302 (2002).

[62] J. Dzubiella, A. Jusufi, C. N. Likos, C. von Ferber, H. Löwen, J. Stellbrink, J. Allgaier, D. Richter, A. B. Schofield, P. A. Smith, W. C. K. Poon, and P. N. Pusey. Phase separation in star-polymer–colloid mixtures. Phys. Rev. E **64**, 010401 (2001).

[63] G. A. Vliegenthart and H. N. W. Lekkerkerker. Measurement of the interfacial tension of demixed colloid-polymer suspensions. Prog. Coll. Pol. Sci. **105**, 27 (1997).

[64] E. H. A. de Hoog and H. N. W. Lekkerkerker. Measurement of the interfacial tension of a phase-separated colloid-polymer suspension. J. Phys. Chem. B **103**, 5274 (1999).

[65] B.-H. Chen, B. Payandeh, and M. Robert. Order parameter and interfacial tension of a colloid-polymer system. Phys. Rev. E **62**, 2369 (2000).

[66] B.-H. Chen, B. Payandeh, and M. Robert. Turbidity and critical behavior of a colloid-polymer system. Phys. Rev. E **64**, 042401 (2001).

[67] D. G. A. L. Aarts, J. H. van der Wiel, and H. N. W. Lekkerkerker. Interfacial dynamics and the static profile near a single wall in a model colloid-polymer mixture. J. Phys. **15**, S245 (2003).

[68] W. K. Wijting, N. A. M. Besseling, and M. A. Cohen Stuart. Wetting behavior in colloid-polymer mixtures at different substrates. J. Phys. Chem. B **107**, 10565 (2003).

[69] W. K. Wijting, N. A. M. Besseling, and M. A. Cohen Stuart. Wetting in a colloidal liquid-gas system. Phys. Rev. Lett. **90**, 196101 (2003).

[70] J. O. Indekeu, D. G. A. L. Aarts, H. N. W. Lekkerkerker, Y. Hennequin, and D. Bonn. Thermal fluctuation forces and wetting layers in colloid-polymer mixtures: Derivation of an interface potential. Phys. Rev. E **81**, 041604 (2010).

[71] D. G. A. L. Aarts, M. Schmidt, and H. N. W. Lekkerkerker. Direct visual observation of thermal capillary waves. Science **304**, 847 (2004).

[72] R. L. C. Vink, J. Horbach, and K. Binder. Capillary waves in a colloid-polymer interface. J. Chem. Phys. **122**, 134905 (2005).

[73] M. Laurati, G. Petekidis, N. Koumakis, F. Cardinaux, A. B. Schofield, J. M. Brader, M. Fuchs, and S. U. Egelhaaf. Structure, dynamics, and rheology of colloid-polymer mixtures: From liquids to gels. J. Chem. Phys. **130**, 134907 (2009).

[74] A. Stradner, H. Sedgwick, F. Cardinaux, W. C. K. Poon, S. U. Egelhaaf, and P. Schurtenberger. Equilibrium cluster formation in concentrated protein solutions and colloids. Nature **432**, 492 (2004).

[75] K. N. Pham, A. M. Puertas, J. Bergenholtz, S. U. Egelhaaf, A. Moussaid, P. N. Pusey, A. B. Schofield, M. E. Cates, M. Fuchs, and W. C. K. Poon. Multiple glassy states in a simple model system. Science **296**, 104 (2002).

[76] E. Zaccarelli, H. Löwen, P. P. F. Wessels, F. Sciortino, P. Tartaglia, and C. N. Likos. Is there a reentrant glass in binary mixtures? Phys. Rev. Lett. **92**, 225703 (2004).

[77] R. L. C. Vink and J. Horbach. Grand canonical Monte Carlo simulation of a model colloid–polymer mixture: Coexistence line, critical behavior, and interfacial tension. J. Chem. Phys. **121**, 3253 (2004).

[78] M. Dijkstra and R. van Roij. Entropic wetting and many-body induced layering in a model colloid-polymer mixture. Phys. Rev. Lett. **89**, 208303 (2002).

[79] T. Zykova-Timan, J. Horbach, and K. Binder. Monte carlo simulations of the solid-liquid transition in hard spheres and colloid-polymer mixtures. J. Chem. Phys. **133**, 014705 (2010).

[80] P. P. F. Wessels, M. Schmidt, and H. Löwen. The contact angle of the colloidal liquid-gas interface and a hard wall. J. Phys. **16**, S4169 (2004).

[81] P. P. F. Wessels, M. Schmidt, and H. Löwen. Wall tensions of model colloid-polymer mixtures. J. Phys. **16**, L1 (2004).

[82] K. Binder, J. Horbach, R. Vink, and A. De Virgiliis. Confinement effects on phase behavior of soft matter systems. Soft Matter **4**, 1555 (2008).

[83] A. de Virgiliis, R. L. C. Vink, J. Horbach, and K. Binder. From capillary condensation to interface localization transitions in colloid-polymer mixtures confined in thin-film geometry. Phys. Rev. E **78**, 041604 (2008).

[84] A. de Virgiliis, R. L. C. Vink, J. Horbach, and K. Binder. Colloid-polymer mixtures between asymmetric walls: Evidence for an interface localization transition. Europhys. Lett. **77**, 60002 (2007).

[85] R. L. C. Vink, K. Binder, and H. Löwen. Critical behavior of colloid-polymer mixtures in random porous media. Phys. Rev. Lett. **97**, 230603 (2006).

[86] A. Fortini, M. Schmidt, and M. Dijkstra. Phase behavior and structure of model colloid-polymer mixtures confined between two parallel planar walls. Phys. Rev. E **73**, 051502 (2006).

[87] M. Schmidt, A. Fortini, and M. Dijkstra. Capillary condensation of colloid-polymer mixtures confined between parallel plates. J. Phys. **15**, S3411 (2003).

[88] J. M. Brader and R. Evans. The fluid-fluid interface of a model colloid-polymer mixture. Europhys. Lett. **49**, 678 (2000).

[89] R. Evans, J. M. Brader, R. Roth, M. Dijkstra, M. Schmidt, and H. Löwen. Interfacial properties of model colloid-polymer mixtures. Philos. T. Roy. Soc. A **359**, 961 (2001).

[90] J. M. Brader, R. Evans, M. Schmidt, and H. Löwen. Entropic wetting and the fluid-fluid interface of a model colloid-polymer mixture. J. Phys. **14**, L1 (2002).

[91] P. P. F. Wessels, M. Schmidt, and H. Löwen. Capillary condensation and interface structure of a model colloid-polymer mixture in a porous medium. Phys. Rev. E **68**, 061404 (2003).

[92] P. P. F. Wessels, M. Schmidt, and H. Löwen. Wetting, drying, and layering of colloid-polymer mixtures at porous interfaces. Phys. Rev. Lett. **94**, 078303 (2005).

[93] G. Pellicane, R. L. C. Vink, C. Caccamo, and H. Löwen. Colloid-polymer mixtures in the presence of quenched disorder: a theoretical and computer simulation study. J. Phys. **20**, 115101 (2008).

[94] R. L. C. Vink, K. Binder, and H. Löwen. Colloid-polymer mixtures in random porous media: finite size scaling and connected versus disconnected susceptibilities. J. Phys. **20**, 404222 (2008).

[95] R. L. C. Vink. Critical behavior of soft matter fluids in bulk and in random porous media: from Ising to random-field Ising universality. Soft Matter **5**, 4388 (2009).

[96] M. Schmidt, M. Dijkstra, and J.-P. Hansen. Floating liquid phase in sedimenting colloid-polymer mixtures. Phys. Rev. Lett. **93**, 088303 (2004).

[97] E. A. G. Jamie, H. H. Wensink, and D. G. A. L. Aarts. Probing the critical behavior of colloidal interfaces by gravity. Soft Matter **6**, 250 (2010).

[98] P. Chaudhuri, C. Das, C. Dasgupta, H. R. Krishnamurthy, and A. K. Sood. Laser-induced reentrant freezing in two-dimensional attractive colloidal systems. Phys. Rev. E **72**, 061404 (2005).

[99] K. Franzrahe and P. Nielaba. Controlled structuring of binary hard-disk mixtures via a periodic, external potential. Phys. Rev. E **79**, 051505 (2009).

[100] D. Frenkel and B. Smit. *Understanding Molecular Simulation* (Academic Press, San Diego, 2001).

[101] P. Virnau and M. Müller. Calculation of free energy through successive umbrella sampling. J. Chem. Phys. **120**, 10925 (2004).

[102] K. Binder. Finite size scaling analysis of ising model block distribution functions. Z. Phys. B **43**, 119 (1981).

[103] Y. C. Kim and M. E. Fisher. Fluid coexistence close to criticality: scaling algorithms for precise simulation. Comput. Phys. Commun. **169**, 295 (2005).

[104] Y. C. Kim and M. E. Fisher. Asymmetric fluid criticality. ii. finite-size scaling for simulations. Phys. Rev. E **68**, 041506 (2003).

[105] M. E. J. Newman and G. T. Barkema. *Monte Carlo Methods in Statistical Physics* (Clarendon Press, Oxford, 1999).

[106] J. S. Rowlinson and B. Widom. *Molecular Theory of Capillarity* (Clarendon Press, Oxford, Oxfordshire, 1982).

[107] B. Grossmann and M. L. Laursen. The confined-deconfined interface tension in quenched QCD using the histogram method. Nucl. Phys. B **408**, 637 (1993).

[108] T. Fischer and R. L. C. Vink. The Widom-Rowlinson mixture on a sphere: elimination of exponential slowing down at first-order phase transitions. J. Phys. **22**, 104123 (2010).

[109] K. Vollmayr, J. D. Reger, M. Scheucher, and K. Binder. Finite size effects at thermally-driven first order phase transitions: A phenomenological theory of the order parameter distribution. Z. Phys. B **91**, 113 (1993).

[110] D. L. J. Vossen, A. van der Horst, M. Dogterom, and A. van Blaaderen. Optical tweezers and confocal microscopy for simultaneous three-dimensional manipulation and imaging in concentrated colloidal dispersions. Rev. Sci. Instrum. **75**, 2960 (2004).

[111] C. P. Royall, D. G. A. L. Aarts, and H. Tanaka. Bridging length scales in colloidal liquids and interfaces from near-critical divergence to single particles. Nat. Phys. **3**, 636 (2007).

[112] F. Freire, D. O'Connor, and C. R. Stephens. Dimensional crossover and finite-size scaling below t_c. J. Stat. Phys. **74**, 219 (1994).

[113] M. C. Jenkins and S. U. Egelhaaf. Colloidal suspensions in modulated light fields. J. Phys. **20**, 404220 (2008).

[114] A. P. Philipse. Colloidal sedimentation (and filtration). Curr. Opin. Colloid Interface Sci. **2**, 200 (1997).

[115] V. N. Manoharan, M. T. Elsesser, and D. J. Pine. Dense packing and symmetry in small clusters of microspheres. Science **301**, 483 (2003).

[116] M. Rasa and A. P. Philipse. Evidence for a macroscopic electric field in the sedimentation profiles of charged colloids. Nature **429**, 857 (2004).

[117] A. Moncho-Jordá, A. A. Louis, and J. T. Padding. Effects of interparticle attractions on colloidal sedimentation. Phys. Rev. Lett. **104**, 068301 (2010).

[118] A. Rosato, K. J. Strandburg, F. Prinz, and R. H. Swendsen. Why the brazil nuts are on top: Size segregation of particulate matter by shaking. Phys. Rev. Lett. **58**, 1038 (1987).

[119] T. Shinbrot and F. J. Muzzio. Reverse buoyancy in shaken granular beds. Phys. Rev. Lett. **81**, 4365 (1998).

[120] D. C. Hong, P. V. Quinn, and S. Luding. Reverse brazil nut problem: Competition between percolation and condensation. Phys. Rev. Lett. **86**, 3423 (2001).

[121] J. A. Both and D. C. Hong. Variational approach to hard sphere segregation under gravity. Phys. Rev. Lett. **88**, 124301 (2002).

[122] X. Yan, Q. Shi, M. Hou, K. Lu, and C. K. Chan. Effects of air on the segregation of particles in a shaken granular bed. Phys. Rev. Lett. **91**, 014302 (2003).

[123] S. Godoy, D. Risso, R. Soto, and P. Cordero. Rise of a brazil nut: A transition line. Phys. Rev. E **78**, 031301 (2008).

[124] V. Garzó. Brazil-nut effect versus reverse brazil-nut effect in a moderately dense granular fluid. Phys. Rev. E **78**, 020301 (2008).

[125] A. Wysocki, C. P. Royall, R. G. Winkler, G. Gompper, H. Tanaka, A. van Blaaderen, and H. Löwen. Direct observation of hydrodynamic instabilities in a driven non-uniform colloidal dispersion. Soft Matter **5**, 1340 (2009).

[126] H. Löwen. Particle-resolved instabilities in colloidal dispersions. Soft Matter **6**, 3133 (2010).

[127] G. Brambilla, S. Buzzaccaro, R. Piazza, L. Berthier, and L. Cipelletti. Highly nonlinear dynamics in a slowly sedimenting colloidal gel. Phys. Rev. Lett. **106**, 118302 (2011).

[128] C. G. Serrano, J. J. McDermott, and D. Velegol. Sediments of soft spheres arranged by effective density. Nat. Mater. **10**, 716 (2011).

[129] T. Biben, R. Ohnesorge, and H. Löwen. Crystallization in sedimentation profiles of hard spheres. Europhys. Lett. **28**, 665 (1994).

[130] K. Milinković, J. T. Padding, and M. Dijkstra. Hydrodynamic rayleigh-taylor-like instabilities in sedimenting colloidal mixtures. Soft Matter **7**, 11177 (2011).

[131] N. J. Lorenz, H. J. Schöpe, and T. Palberg. Phase behavior of a de-ionized binary mixture of charged spheres in the presence of gravity. J. Chem. Phys. **131**, 134501 (2009).

[132] T. Okubo, A. Tsuchida, S. Takahashi, K. Taguchi, and M. Ishikawa. Kinetics of colloidal alloy crystallization of binary mixtures of monodispersed polystyrene and/or colloidal silica spheres having different sizes and densities in microgravity using aircraft. Colloid Polym. Sci. **278**, 202 (2000).

[133] E. C. M. Vermolen, A. Kuijk, L. C. Filion, M. Hermes, J. H. J. Thijssen, M. Dijkstra, and A. van Blaaderen. Fabrication of large binary colloidal crystals with a nacl structure. Proc. Natl. Acad. Sci. USA **106**, 16063 (2009).

[134] J. F. Gilchrist, A. T. Chan, E. R. Weeks, and J. A. Lewis. Phase behavior and 3d structure of strongly attractive microsphere-nanoparticle mixtures. Langmuir **21**, 11040 (2005).

[135] A. Esztermann and H. Löwen. Colloidal brazil-nut effect in sediments of binary charged suspensions. Europhys. Lett. **68**, 120 (2004).

[136] J. Zwanikken and R. van Roij. The sediment of mixtures of charged colloids: Segregation and inhomogeneous electric fields. Europhys. Lett. **71**, 480 (2005).

[137] T. Biben and J.-P. Hansen. Localized density profiles in binary colloidal suspensions. Mol. Phys. **80**, 853 (1993).

[138] J. S. Vesaratchanon, A. Nikolov, D. Wasan, and D. Henderson. The importance of oscillatory structural forces in the sedimentation of a binary hard-sphere colloidal suspension. Ind. Eng. Chem. Res. **48**, 6641 (2009).

[139] X. L. Chu, A. D. Nikolov, and D. T. Wasan. Effects of interparticle interactions on stability, aggregation and sedimentation in colloidal suspensions. Chem. Eng. Commun. **148-150**, 123 (1996).

[140] M. Schmidt, M. Dijkstra, and J.-P. Hansen. Competition between sedimentation and phase coexistence of colloidal dispersions under gravity. J. Phys. **16**, S4185 (2004).

[141] C. P. Royall, J. Dzubiella, M. Schmidt, and A. van Blaaderen. Nonequilibrium sedimentation of colloids on the particle scale. Phys. Rev. Lett. **98**, 188304 (2007).

[142] J. P. Hoogenboom, D. Derks, P. Vergeer, and A. van Blaaderen. Stacking faults in colloidal crystals grown by sedimentation. J. Chem. Phys. **117**, 11320 (2002).

[143] I. B. Ramsteiner, K. E. Jensen, D. A. Weitz, and F. Spaepen. Experimental observation of the crystallization of hard-sphere colloidal particles by sedimentation onto flat and patterned surfaces. Phys. Rev. E **79**, 011403 (2009).

[144] A. S. Mehrotra, S. Puri, and D. V. Khakhar. Gradient monte carlo simulations: Hard spheres in spatially varying temperature and gravitational fields. Phys. Rev. E **83**, 061306 (2011).

[145] M. Leocmach, C. P. Royall, and H. Tanaka. Novel zone formation due to interplay between sedimentation and phase ordering. Europhys. Lett. **89**, 38006 (2010).

[146] B. L. Smorodin, B. I. Myznikova, and J. C. Legros. Evolution of convective patterns in a binary-mixture layer subjected to a periodical change of the gravity field. Physics of Fluids **20**, 094102 (2008).

[147] M. Kollmann, R. Hund, B. Rinn, G. Nägele, K. Zahn, H. König, G. Maret, R. Klein, and J. K. G. Dhont. Structure and tracer-diffusion in quasi-two-dimensional and strongly asymmetric magnetic colloidal mixtures. Europhys. Lett. **58**, 919 (2002).

[148] H. König, R. Hund, K. Zahn, and G. Maret. Experimental realization of a model glass former in 2d. Eur. Phys. J. E **18**, 287 (2005).

[149] F. Ebert, P. Keim, and G. Maret. Local crystalline order in a 2d colloidal glass former. Eur. Phys. J. E **26**, 161 (2008).

[150] S. Mazoyer, F. Ebert, G. Maret, and P. Keim. Dynamics of particles and cages in an experimental 2d glass former. Europhys. Lett. **88**, 66004 (2009).

[151] F. Ebert, G. Maret, and P. Keim. Partial clustering prevents global crystallization in a binary 2d colloidal glass former. Eur. Phys. J. E **29**, 311 (2009).

[152] L. Assoud, F. Ebert, P. Keim, R. Messina, G. Maret, and H. Löwen. Ultrafast quenching of binary colloidal suspensions in an external magnetic field. Phys. Rev. Lett. **102**, 238301 (2009).

[153] A. Pertsinidis and X. S. Ling. Diffusion of point defects in two-dimensional colloidal crystals. Nature **413**, 147 (2001).

[154] Z. Wang, A. M. Alsayed, A. G. Yodh, and Y. Han. Two-dimensional freezing criteria for crystallizing colloidal monolayers. J. Chem. Phys. **132**, 154501 (2010).

[155] A. Tilmatine, K. Medles, M. Younes, A. Bendaoud, and L. Dascalescu. Roll-type versus free-fall electrostatic separation of tribocharged plastic particles. IEEE T. Ind. Appl. **46**, 1564 (2010).

[156] V. N. Tsytovich, G. Morfill, U. Konopka, and H. Thomas. Collision-dominated dust sheaths and voids - observations in micro-gravity experiments and numerical investigation of the force balance relations. New J. Phys. **5**, 66 (2003).

[157] G. E. Morfill and A. V. Ivlev. Complex plasmas: An interdisciplinary research field. Rev. Mod. Phys. **81**, 1353 (2009).

[158] L. Onsager. The effects of shape on the interaction of colloidal particles. Ann. N.Y. Acad. Sci. **51**, 627 (1949).

[159] H. H. Wensink and H. Löwen. Aggregation of self-propelled colloidal rods near confining walls. Phys. Rev. E **78**, 031409 (2008).

[160] S. van Teeffelen, C. N. Likos, N. Hoffmann, and H. Löwen. Density functional theory of freezing for soft interactions in two dimensions. Europhys. Lett. **75**, 583 (2006).

[161] M. Heni and H. Löwen. Surface freezing on patterned substrates. Phys. Rev. Lett. **85**, 3668 (2000).

[162] M. Allen and D. Tildesley. *Computer Simulation of Liquids* (Clarendon Press, Oxford, 1989).

[163] T. Stirner and Sun. Molecular dynamics simulation of the structural configuration of binary colloidal monolayers. Langmuir **21**, 6636 (2005).

[164] H. Löwen, J.-N. Roux, and J.-P. Hansen. Mapping of charge polydispersity onto size polydispersity in colloidal suspensions. J. Phys. **3**, 997 (1991).

[165] H. Löwen. Structure and brownian dynamics of the two-dimensional yukawa fluid. J. Phys. **4**, 10105 (1992).

[166] W. G. McMillan Jr. and J. E. Mayer. The statistical thermodynamics of multicomponent systems. J. Chem. Phys. **13**, 276 (1945).

[167] J.-P. Hansen and H. Löwen. Effective interactions between electrics double layers. Ann. Rev. Phys. Chem. **51**, 209 (2000).

[168] G. A. Vliegenthart and P. van der Schoot. Kinetics of depletion interactions. Europhys. Lett. **62**, 600 (2003).

[169] M. Rex and H. Löwen. Dynamical density functional theory with hydrodynamic interactions and colloids in unstable traps. Phys. Rev. Lett. **101**, 148302 (2008).

[170] M. Rex and H. Löwen. Dynamical density functional theory for colloidal dispersions including hydrodynamic interactions. Eur. Phys. J. E **28**, 139 (2009).

[171] M. E. Leunissen, C. G. Christova, A.-P. Hynninen, C. P. Royall, A. I. Campbell, A. Imhof, M. Dijkstra, R. van Roij, and A. van Blaaderen. Ionic colloidal crystals of oppositely charged particles. Nature **437**, 235 (2005).

[172] T. Vissers, A. Wysocki, M. Rex, H. Löwen, C. P. Royall, A. Imhof, and A. van Blaaderen. Lane formation in driven mixtures of oppositely charged colloids. Soft Matter **7**, 2352 (2011).

[173] G. P. Hoffmann and H. Löwen. Melting of dusty plasma crystals in oscillating external fields. J. Phys. **12**, 7359 (2000).

[174] B. Comiskey, J. D. Albert, H. Yoshizawa, and J. Jacobson. An electrophoretic ink for all-printed reflective electronic displays. Nature **394**, 253 (1998).

[175] G. H. Gelinck, H. E. A. Huitema, E. van Veenendaal, E. Cantatore, L. Schrijnemakers, J. B. P. H. van der Putten, T. C. T. Geuns, M. Beenhakkers, J. B. Giesbers, B.-H. Huisman, E. J. Meijer, E. M. Benito, F. J. Touwslager, A. W. Marsman, B. J. E. van Rens, and D. M. de Leeuw. Flexible active-matrix displays and shift registers based on solution-processed organic transistors. Nat. Mater. **3**, 106 (2004).

[176] L. D. Landau. Zur Theorie der Phasenumwandlungen I. Phys. Z. Sowjetunion **11**, 26 (1937).

[177] A. Chowdhury, B. J. Ackerson, and N. A. Clark. Laser-induced freezing. Phys. Rev. Lett. **55**, 833 (1985).

[178] J. Chakrabarti, H. R. Krishnamurthy, and A. K. Sood. Density functional theory of laser-induced freezing in colloidal suspensions. Phys. Rev. Lett. **73**, 2923 (1994).

[179] J. Chakrabarti, H. R. Krishnamurthy, A. K. Sood, and S. Sengupta. Reentrant melting in laser field modulated colloidal suspensions. Phys. Rev. Lett. **75**, 2232 (1995).

[180] Q.-H. Wei, C. Bechinger, D. Rudhardt, and P. Leiderer. Experimental study of laser-induced melting in two-dimensional colloids. Phys. Rev. Lett. **81**, 2606 (1998).

[181] E. Frey, D. R. Nelson, and L. Radzihovsky. Light-induced melting of colloidal crystals in two dimensions. Phys. Rev. Lett. **83**, 2977 (1999).

[182] C. Bechinger and E. Frey. Phase behaviour of colloids in confining geometry. J. Phys. **13**, R321 (2001).

[183] M. Brunner and C. Bechinger. Phase behavior of colloidal molecular crystals on triangular light lattices. Phys. Rev. Lett. **88**, 248302 (2002).

[184] C. Reichhardt and C. J. Olson. Novel colloidal crystalline states on two-dimensional periodic substrates. Phys. Rev. Lett. **88**, 248301 (2002).

[185] K. Mangold, P. Leiderer, and C. Bechinger. Phase transitions of colloidal monolayers in periodic pinning arrays. Phys. Rev. Lett. **90**, 158302 (2003).

[186] A. Patrykiejew and S. Sokołowski. Two-dimensional quasicrystals of decagonal order in one-component monolayer films. Phys. Rev. Lett. **99**, 156101 (2007).

[187] M. Schmiedeberg and H. Stark. Comment on “two-dimensional quasicrystals of decagonal order in one-component monolayer films”. Phys. Rev. Lett. **100**, 019601 (2008).

[188] M. Schmiedeberg and H. Stark. Colloidal ordering on a 2d quasicrystalline substrate. Phys. Rev. Lett. **101**, 218302 (2008).

[189] A. Patrykiejew and S. Sokołowski. Patrykiewjew and sokołowski reply:. Phys. Rev. Lett. **100**, 019602 (2008).

[190] W. Rżysko, A. Patrykiejew, and S. Sokołowski. Incommensurate monolayers of archimedean tiling formed on a square lattice. J. Phys. **20**, 494226 (2008).

[191] J. Mikhael, J. Roth, L. Helden, and C. Bechinger. Archimedean-like tiling on decagonal quasicrystalline surfaces. Nature **454**, 501 (2008).

[192] S. El Shawish, J. Dobnikar, and E. Trizac. Ground states of colloidal molecular crystals on periodic substrates. Soft Matter **4**, 1491 (2008).

[193] C. V. Achim, M. Karttunen, K. R. Elder, E. Granato, T. Ala-Nissila, and S. C. Ying. Phase diagram of pinned lattices in the phase field crystal model. J. Phys. **100**, 072001 (2008).

[194] M. Schmiedeberg, J. Mikhael, S. Rausch, J. Roth, L. Helden, C. Bechinger, and H. Stark. Archimedean-like colloidal tilings on substrates with decagonal and tetradecagonal symmetry. Eur. Phys. J. E **32**, 25 (2010).

[195] E. Granato, J. A. P. Ramos, C. V. Achim, J. Lehikoinen, S. C. Ying, T. Ala-Nissila, and K. R. Elder. Glassy phases and driven response of the phase-field-crystal model with random pinning. Phys. Rev. E **84**, 031102 (2011).

[196] C. Reichhardt, C. J. Olson, R. T. Scalettar, and G. T. Zimányi. Commensurate and incommensurate vortex lattice melting in periodic pinning arrays. Phys. Rev. B **64**, 144509 (2001).

[197] G. R. Berdiyorov, M. V. Milošević, and F. M. Peeters. Composite vortex ordering in superconducting films with arrays of blind holes. New J. Phys. **11**, 013025 (2009).

[198] S. N. Coppersmith, D. S. Fisher, B. I. Halperin, P. A. Lee, and W. F. Brinkman. Dislocations and the commensurate-incommensurate transition in two dimensions. Phys. Rev. Lett. **46**, 549 (1981).

[199] M. Grunze, P. H. Kleban, W. N. Unertl, and F. S. Rys. Evidence for a commensurate-incommensurate phase transition with an intermediate fluid phase: n_2 adsorbed on ni(110). Phys. Rev. Lett. **51**, 582 (1983).

[200] T. Arnold and S. M. Clarke. Diffraction from physisorbed layers. Curr. Opin. Colloid Interface Sci. **17**, 23 (2012).

[201] D. R. Nelson and B. I. Halperin. Dislocation-mediated melting in two dimensions. Phys. Rev. B **19**, 2457 (1979).

[202] A. C. Mitus, H. Weber, and D. Marx. Local structure analysis of the hard-disk fluid near melting. Phys. Rev. E **55**, 6855 (1997).

[203] M. M. Burns, J.-M. Fournier, and J. A. Golovchenko. Optical matter: Crystallization and binding in intense optical fields. Science **249**, 749 (1990).

[204] A. van Blaaderen, R. Ruel, and P. Wiltzius. Template-directed colloidal crystallization. Nature **385**, 321 (1997).

[205] J. A. Weiss, D. A. Oxtoby, D. G. Grier, and C. A. Murray. Martensitic transition in a confined colloidal suspension. J. Chem. Phys. **103**, 1180 (1995).

[206] S. van Teeffelen, H. Löwen, and C. N. Likos. Crystallization of magnetic dipolar monolayers: a density functional approach. J. Phys. **20**, 404217 (2008).

[207] Y. Rosenfeld. Free-energy model for the inhomogeneous hard-sphere fluid in d dimensions: Structure factors for the hard-disk (d=2) mixtures in simple explicit form. Phys. Rev. A **42**, 5978 (1990).

[208] S. Neser, C. Bechinger, P. Leiderer, and T. Palberg. Finite-size effects on the closest packing of hard spheres. Phys. Rev. Lett. **79**, 2348 (1997).

[209] A. Ricci, P. Nielaba, S. Sengupta, and K. Binder. Ordering of two-dimensional crystals confined in strips of finite width. Phys. Rev. E **75**, 011405 (2007).

[210] D. Wilms, N. B. Wilding, and K. Binder. Transitions between imperfectly ordered crystalline structures: A phase switch monte carlo study. Phys. Rev. E **85**, 056703 (2012).

[211] A. Vanossi, N. Manini, and E. Tosatti. Inaugural article: Static and dynamic friction in sliding colloidal monolayers. Proc. Natl. Acad. Sci. USA **109**, 16429 (2012).

[212] J. C. Meyer, A. K. Geim, M. I. Katsnelson, K. S. Novoselov, T. J. Booth, and S. Roth. The structure of suspended graphene sheets. Nature **446**, 60 (2007).

[213] K. S. Kim, Y. Zhao, H. Jang, S. Y. Lee, J. M. Kim, K. S. Kim, J.-H. Ahn, P. Kim, J.-Y. Choi, and B. H. Hong. Large-scale pattern growth of graphene films for stretchable transparent electrodes. Nature **457**, 706 (2009).

[214] J. Aizenberg, A. J. Black, and G. M. Whitesides. Control of crystal nucleation by patterned self-assembled monolayers. Nature **398**, 495 (1999).

[215] A. L. Briseno, S. C. B. Mannsfeld, M. M. Ling, S. Liu, R. J. Tseng, C. Reese, M. E. Roberts, Y. Yang, F. Wudl, and Z. Bao. Patterning organic single-crystal transistor arrays. Nature **444**, 913 (2006).

[216] X. Wang, C. J. Summers, and Z. L. Wang. Large-scale hexagonal-patterned growth of aligned zno nanorods for nano-optoelectronics and nanosensor arrays. Nano Lett. **4**, 423 (2004).

[217] T. P. Bigioni, X.-M. Lin, T. T. Nguyen, E. I. Corwin, T. A. Witten, and H. M. Jaeger. Kinetically driven self assembly of highly ordered nanoparticle monolayers. Nat Mater **5**, 265 (2006).

[218] J. A. van Meel, R. P. Sear, and D. Frenkel. Design principles for broad-spectrum protein-crystal nucleants with nanoscale pits. Phys. Rev. Lett. **105**, 205501 (2010).

[219] R. A. Segalman. Patterning with block copolymer thin films. Mat. Sci. Eng. R **48**, 191 (2005).

[220] J. Aizenberg, P. V. Braun, and P. Wiltzius. Patterned colloidal deposition controlled by electrostatic and capillary forces. Phys. Rev. Lett. **84**, 2997 (2000).

[221] V. A. Shchukin and D. Bimberg. Spontaneous ordering of nanostructures on crystal surfaces. Rev. Mod. Phys. **71**, 1125 (1999).

[222] G. I. Tóth, G. Tegze, T. Pusztai, and L. Gránásy. Heterogeneous crystal nucleation: The effect of lattice mismatch. Phys. Rev. Lett. **108**, 025502 (2012).

[223] S. Dorosz and T. Schilling. On the influence of a patterned substrate on crystallization in suspensions of hard spheres. J. Chem. Phys. **136**, 044702 (2012).

[224] S. Jungblut and C. Dellago. Crystallization on prestructured seeds. Phys. Rev. E **87**, 012305 (2013).

[225] M. Trau, D. A. Saville, and I. A. Aksay. Field-induced layering of colloidal crystals. Science **272**, 706 (1996).

[226] A. Ivlev, G. Morfill, and H. Löwen. *Complex Plasmas and Colloidal Dispersions: Particle-Resolved Studies of Classical Liquids and Solids* (World Scientific, 2012).

[227] C. Bechinger, M. Brunner, and P. Leiderer. Phase behavior of two-dimensional colloidal systems in the presence of periodic light fields. Phys. Rev. Lett. **86**, 930 (2001).

[228] J. S. Langer. Instabilities and pattern formation in crystal growth. Rev. Mod. Phys. **52**, 1 (1980).

[229] G. Tegze, G. I. Tóth, and L. Gránásy. Faceting and branching in 2d crystal growth. Phys. Rev. Lett. **106**, 195502 (2011).

[230] P. Espanol and H. Löwen. Derivation of dynamical density functional theory using the projection operator technique. J. Chem. Phys. **131**, 244101 (2009).

[231] J. Hermisson, C. Richard, and M. Baake. A guide to the symmetry structure of quasiperiodic tiling classes. J. Phys. I France **7**, 1003 (1997).